dCollection

Master's Thesis of Engineering

Fire Behavior of Post-Tensioned Concrete One-Way Members with Different Tendon Configuration

텐던공법에 따른 일방향 포스트텐션 콘크리트 부재의 내화거동

February 2022

Graduate School of Engineering

Seoul National University

Architecture and Architectural Engineering

Siyoung Park

Fire Behavior of Post-Tensioned Concrete One-Way Members with Different Tendon Configuration

Advisor: Thomas Kang

Submitting a Master's thesis of
Architecture and Architectural Engineering

February 2022

Graduate School of Engineering
Seoul National University
Architecture and Architectural Engineering

Siyoung Park

Confirming the Master's thesis written by
Siyoung Park

February 2022

Chair	Sung-Gul Hong	(Seal)
Vice Chair	Thomas Kang	(Seal)
Examiner	Hong-Gun Park	(Seal)

Abstract

Fire Behavior of Post-Tensioned Concrete One-Way Members with Different Tendon Configuration

Park, Siyoung
Department of Architecture and Architectural Engineering
College of Engineering
Seoul National University

Recently, the application of the post-tensioned (PT) method to concrete structures such as underground structures, long-span structures, and containment structures has increased. Structural safety under multiple hazards has been an issue for those structures, and therefore several building codes have been enacted and revised. In terms of fire resistance, there are domestic standards of Korean Standard (KS) F 2257 that specifies the fire resistance test method and National Legal that regulates fire safety design. There are also international standards such as IBC 2018 and ASTM E119 that specify fire safety design and fire test methods. However, existing standards include limited information and tend to be ambiguous in may clauses. Questions are continuously being raised as to whether or not the standards presented in the regulations are appropriate. In this study, fire tests of two one-way bonded PT concrete slabs and six one-way unbonded PT concrete slabs were conducted

under four-point static loading and monotonically increasing heating to evaluate the fire performance of the structures.

The variables considered in the test included tendon configuration, cover thickness, and fire resistance rating. Four specimens were manufactured to endure fire for two hours, others were designed to last three hours. All specimens installed thermocouples at the bottom, tendon, and top locations to measure temperature change. Self-made load cells were installed on unbonded cases to measure tendon stresses and their change at jacking and fire test stages. Deflection of slabs was measured at the center of specimens using an LVDT.

Test results demonstrated that bonded cases sufficiently endured two hours and three hours of fire with the minimum cover thickness specified in IBC 2018. However, unbonded cases ruptured prematurely compared to the expected fire resistance rating. Concrete spalling and delamination significantly affected test results, and other factors were also investigated to address reasons for early termination. Although the test ended earlier, the difference in fire behavior according to the tendon configuration in terms of temperature change, tendon stress change, and deflection change could be analyzed. For bonded cases, finite element analysis has been performed to assess the fire performance with varied cover thicknesses under the design fire resistance rating.

In conclusion, this study effectively analyzed the fire behavior of PT concrete one-way members with different tendon configuration. Numerical analysis was performed to check the fire performance with different cover thickness and verify the fire test results. Results from this study are expected to be used as basic research data to codify or revise fire design codes.

Keywords : bonded, cover thickness, fire resistance rating, one-way, post-tensioned concrete slab, tendon configuration, unbonded.

Student Number : 2020-29310

Contents

List of Tables

List of Figures

List of Notations

A_c	area of concrete, mm^2
A_p	area of prestressed longitudinal tension reinforcement, mm^2
A_s	area of non-prestressed reinforcement, mm^2
b	width of member, mm
b_w	width of member's web, mm
c	distance from extreme compression fiber to neutral axis, mm
c_c	concrete specific heat, J/(kgK)
c_s	specific heat of steel, J/(kgK)
c_t	concrete cover thickness at critical section, mm
d	distance from extreme compression fiber to extreme tensile fiber, mm
d_p	distance from extreme compression fiber to centroid of prestressing reinforcement, mm
E_c	elastic modulus of concrete in room temperature, MPa
$E_{cr,T}$	elastic modulus of concrete according to temperature, MPa
E_p	modulus of elasticity of prestressing reinforcement, MPa
$E_{s,0}$	elastic modulus of steel in room temperature, MPa
$E_{s,T}$	elastic modulus of steel according to temperature, MPa
e	distance from concrete centroid to prestressing reinforcement, mm
$F_{p,T}$	tendon tensile force, MPa

f_{cr}	tensile strength of concrete in room temperature, MPa
$f_{cr,T}$	tensile strength of concrete according to temperature, MPa
f_{ps}	stress in prestressed reinforcement at nominal flexural strength, MPa
f_{pu}	ultimate strength of prestressed reinforcement, MPa
f_{py}	yield strength of prestressing reinforcement, MPa
f_{se}	effective stress in prestressing reinforcement after allowance for all prestress losses, MPa
f_y	yield strength of non-prestressed reinforcement, MPa
$f_{ys,0}$	yield strength of steel in room temperature, MPa
$f_{ys,T}$	yield strength of steel according to temperature, MPa
f'_{cT}	compressive strength of concrete according to temperature, MPa
f'_c	compressive strength of concrete in room temperature, MPa
f'_m	masonry strength, MPa
h	overall thickness, height, or depth of member, mm
h_c	convective hat transfer coefficient, W/(m^{2}K)
l_c	inertia moment of concrete, mm^4
k_c	thermal conductivity of concrete, W/(mK)
$k_{ck,t}$	degradation rate of concrete tensile strength according to temperature
k_s	thermal conductivity of steel, W/(mK)
L_t	length of tendon, mm
L_c	clear span of beam, mm
l	length of member, mm
l_e	effective tendon length, mm

l_n	length of clear span measured face-face of supports, mm
N_s	number of support hinges crossed by tendon
n	outward normal direction of member surface
P_e	prestressing force at service load stage, N
P_v	additional axial force, N
Q	inherently generated heat, J/K
T	material temperature, K
T_f	average temperature of inside of furnace, K
T_s	absolute zero temperature, K
t	test time, min
w	water content by weight, %
$\alpha_{c,T}$	concrete coefficient of thermal expansion, m/(mK)
α_s	steel coefficient of thermal expansion, m/(mK)
ε_{cu}	ultimate concrete compression strain
ε_f	heat emissivity of fire
ε_m	heat emissivity of exposed surface
ε_{ps}	strain in prestressed reinforcement at nominal flexural strength
ε'_{cT}	concrete strain according to temperature
σ_{pe}	effective prestress at ambient conditions, MPa
ρ_c	concrete density, kg/m^3
ρ_s	density of steel, kg/m^3
η	load level, defined as ratio of applied loading to capacity of slab at ambient temperature

Chapter 1. Introduction

1.1 Introduction

1.1.1 Bonded and unbonded post-tensioning systems

The first patent for prestressed concrete (PC) was issued to P. H. Jackson of San Francisco in 1886. This PC system is actively used in commercial buildings, residential apartments, parking structures, long-span bridges, and nuclear containment buildings based on technological development and market strategies (PTI, 2006; Hou et al., 2013). PC is a method that applies a tensioning force to the prestressing steel with an engaging pre-compressive force to concrete. This pre-force compensates for the tensile weakness of concrete, and the compensation induces advantages such as crack control, deflection control, reduced slab width to depth ratio, and increased load capacity in PC system (Burns et al., 1978).

Post-tensioning (PT) method, one of the PC systems, is a method that applies tensioning force to prestressing steel after concrete curing, which is pre-installed in PT ducts. PT system can be classified into two categories according to the number of strands in duct or sheath; single-strand tendon and multi-strand tendon (**Figure 1-1**). The single-strand method is widely used for the construction of relatively small-sized buildings or infrastructure. Whereas, the multi-strand method is frequently used for large-scale buildings and infrastructure, especially in long-span bridges and nuclear containment buildings (Yoon et al., 2019).
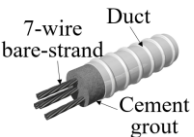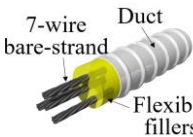
Single-strand tendon and multi-strand tendon systems have a composition of strands, filling material, duct, anchorage, and wedge (**Figure 1-1**). Types of strands include bare-strand and greased sheathed-strand, and types of filling material include cement grout, and flexible fillers such as grease or wax. Depending on the type of strands and filling material, tendon systems are

classified into bonded bare-strand tendon, unbonded bare-strand tendon, and unbonded high-density polyethylene (HDPE) sheathed-strand tendon. The characteristics of each post-tensioning tendon are summarized in **Table 1-1**.

(a) Single-strand tendon   (b) Multi-strand tendon

Figure 1-1 Single-strand tendon and multi-strand tendon (VSL, 2015)

Table 1-1 Characteristics of each PT tendon (Shin et al., 2020)

Type	Bonded bare-strand tendon	Unbonded bare-strand tendon	Unbonded HDPE sheathed-strand tendon
Composition			
Corrosion protection layers	Cement grout	Flexible fillers	Cement grout + HDPE sheath + PT coating
Adverse effects	Cracks, void, and bleeding	Leakage of flexible fillers	HDPE sheath damage
Strand installation	Easy	Easy	Difficult
Duct size	Small	Small	Large
Detensioning	Impossible	Possible but difficult	Possible and easy
Restressing			
Replacment of strands			
Stress measurement of tendon in service	Impossible	Possible	Possible
Stress measurement of individual strand in service	Impossible	Impossible	Possible

1.1.2 Fire safety engineering in structures

Fire is one of the severe disasters that may induce thousands of human casualties and property loss each year. People expect that their lives and homes will be safe from the ravages of an unwanted fire, but fire can initiate in any place without notice. Regarding the fire damage, there are prevention methods such as provision of automatic fire sprinklers, detection and notification of fires, safe travel paths, barriers, and structures that do not prematurely collapse (Buchanan and Abu, 2017). Fire safety engineering concept came up with an idea considering these prevention methods with being defined as follows (Purkiss and Li, 2014):

"The application of scientific and engineering principles to the effects of fire in order to reduce the loss of life and damage to property by quantifying the risks and hazards involved and provide an optimal solution to the application of preventive or protective measures."

Figure 1-2 shows a typical time-temperature curve for complete process of fire development inside a room. After fire ignites, temperature increases to about 600°C where burning rate increases rapidly, leading to a flashover that is transition to burning period. The burning period seriously impacts structural elements and compartment boundaries. After fuel burns out, temperature drops out in a decay period, leading to eventual end of burning.
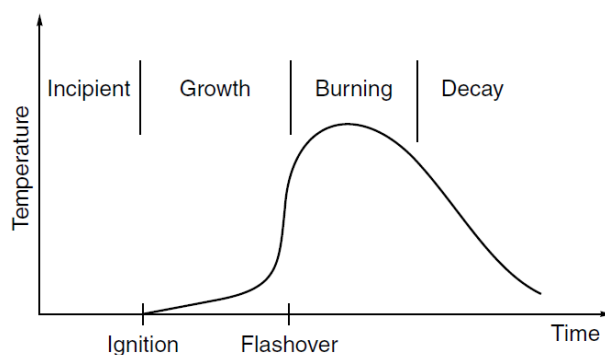
Figure 1-2 Time-temperature curve for full process of fire development
(Buchanan and Abu, 2017)

To avoid damage in the fire development procedure, engineers have devised a fire protection strategy in a passive approach and an active approach. An active approach includes alarms/detection systems and sprinklers that can be a direct and fast method for fire protection (**Figure 1-3**). A passive approach designs buildings to achieve fire resistance and structural stability. For simple and convenient design, prescriptive fire design codes are specified. **Table 1-2** is an example of prescriptive fire resistance rating specified by the International Building Code (IBC) of the United States (ICC, 2017).

| (a) Fire extinguisher | (b) Ceiling sprinkler | (c) Fire alarm system |

Figure 1-3 Active approach on fire protection strategy

Table 1-2 Example of prescriptive fire resistance rating (ICC, 2017)

(a) Minimum slab thickness (mm)					
Concrete aggregate type	Fire-resistance rating (hours)				
	1	1-1/2	2	3	4
Siliceous	88.9	109.2	127	157.5	177.8
Carbonate	81.3	101.6	116.8	144.8	167.6
Sand lightweight	68.6	83.8	96.5	116.8	137.2
Lightweight	63.5	78.7	91.4	111.8	129.5

(b) Cover thickness for PC floor or roof slabs (mm)										
Concrete aggregate type	Fire-resistance rating (hours)									
	Restrained					Unrestrained				
	1	3/2	2	3	4	1	3/2	2	3	4
Siliceous	19.1	19.1	19.1	19.1	19.1	28.6	38.1	44.5	60.3	69.9
Carbonate	19.1	19.1	19.1	19.1	19.1	25.4	34.9	41.3	54.0	57.2
Sand-lightweight or lightweight	19.1	19.1	19.1	19.1	19.1	25.4	34.9	38.1	50.8	57.2

This prescriptive fire design has long been a standard for the construction of fire-resistance buildings. However, recently, researchers are questioning the validity of prescriptive fire design code since it does not contain specific design conditions and it often demands the excessive dimension of structural elements that brings high construction costs.

PC, especially PT concrete, has diverse tendon systems, which include bonded bare-strand tendon, unbonded bare-strand tendon, and unbonded HDPE sheathed-strand tendon. Though there have been fire tests that examined the performance of PT concrete slabs, tests were limited to adjusting slab thickness, restrained type, or fire scenario (Ellobody and Bailey, 2008; Bailey and Ellobody, 2009; Kodur and Dwaikat, 2010; Hou et al., 2013). Tendon, which is responsible for the flexural strength of PT slabs, is vulnerable to high temperature (ASCE, 1992; EN1993-1-2, 2005; Kodur et al., 2010; Du et al., 2018). Although bonded and unbonded tendon have similar behavioral characteristics at a working stage, their behaviors become different in the plastic phases. In the view of prescriptive fire design that specifies the fire-resistance rating, structures would undergo both elastic and plastic phases. Therefore, it is necessary to evaluate fire-resistance performance of PT slabs depending on tendon configuration within designed fire-resistance rating.

To assess fire performance of PT slabs with different tendon configuration, eight one-way PT slabs were tested and analyzed in terms of flexural behavior. Deflection and deflection rate were measured depending on the elapse of time and temperature change. Also, variation of the tendon tensile force in unbonded cases was measured during the initial post-tensioning stage and fire test stage.

1.2 Scope and objectives

The main purpose of this study is to investigate the behavior and performance of both bonded and unbonded PT one-way slabs subjected to fire and loading. Eight slabs were designed following the provisions of IBC 2018 to withstand two or three hours of heating, according to the time-temperature curve specified in ISO 834 (ISO, 1999). All specimens had 1,860 MPa strength strands. Four of the specimens were with bare-strand tendon and others were with HDPE sheathed-strand tendon. The specimens were designed following ACI 318-19

(ACI, 2019). From the fire tests, the following behavior and performance of PT slabs were investigated: temperature change in the bottom of slab, tendon and the top of slab, deflection, deflection rate, and tensile stress change according to the time and temperature variation. Finite element modeling and analysis were conducted in the case of the bonded bare-strand tendon for verification of test and additional study on fire performance of slab according to cover thickness of the slab.

1.3 Organization

The thesis is composed of seven main chapters, as summarized in **Figure 1-4**. Introduction, purpose, and scope of the research are briefly shown in **Chapter 1**. Current codes and specifications related to fire safety design and test method of PT slabs, and previous studies of PT slabs are discussed in **Chapter 2**. Design process including details of eight specimens and an instrumentation plan are shown in **Chapter 3**. **Chapter 4** contains the description of specimen construction, post-tensioning procedure, material properties, and test setup. Fire test results and assessment of eight specimens are described and compared in **Chapter 5**. Numerical analysis of the bonded PT slabs for further research on appropriate cover thickness by fire-resistance rating is shown in **Chapter 6**. Conclusions are given in **Chapter 7**.

Chapter 1. Introduction	- Research background - Research scope and objectives
Chapter 2. Review of Codes, Specifications, and Previous Studies	- Current codes and specifications - Previous studies of PT slabs under fire
Chapter 3. Specimen Design	- Specimen outline - Specimen design - Tendon design
Chapter 4. Specimen Construction and Test Setup	- Specimen construction - Post-tensioning - Material properties - Test setup
Chapter 5. Fire Test Results	- Thermal variation of specimens under fire specified in ISO 834 - Effects of high temperature on structures by different tendon configuration - Fire performance of post-tensioned slabs
Chapter 6. Numerical Analysis	- Finite element modeling of bonded PT concrete slabs - Finite element analysis of bonded PT concrete slabs
Chapter 7. Conclusion	- Summary of results - Conclusion

Figure 1-4 Contents of thesis

Chapter 2. Review of Codes, Specifications, and Previous Studies

2.1 Tendon stress at nominal flexural strength (f_{ps})

Estimation of tendon stress (f_{ps}) at ultimate is crucial in designing PT slabs since f_{ps} significantly affects the flexural strength of PT slabs. The f_{ps} of the bonded tendon can be determined by using the strain compatibility method of section (**Eq. (2-1)** to **Eq. (2-5)**).

$$f_{ps} = E_p \varepsilon_{ps} \tag{2-1}$$

$$\varepsilon_{ps} = \varepsilon_{se} + \varepsilon_2 + \varepsilon_3 \tag{2-2}$$

$$\varepsilon_{se} = \frac{P_e}{A_p E_p} \tag{2-3}$$

$$\varepsilon_2 = -\frac{1}{E_c}\left(\frac{P_e}{A_c} + \frac{P_e e}{I_c}e\right) \tag{2-4}$$

$$\varepsilon_3 = \varepsilon_{cu}\left(\frac{d_p - c}{c}\right) \tag{2-5}$$

Where, A_c is area of concrete; A_p is area of prestressed longitudinal tension reinforcement; c is distance from extreme compression fiber to neutral axis; d_p is distance from extreme compression fiber to centroid of prestressing reinforcement; e is distance from concrete centroid to prestressing reinforcement; E_c is modulus elasticity of concrete; E_p is modulus of elasticity of prestressing reinforcement; f_{ps} is stress in prestressed reinforcement at nominal flexural strength; I_c is inertia moment of concrete; P_e is prestressing force at service load stage; ε_{cu} is ultimate concrete compressive strain; and ε_{ps} is strain in prestressed reinforcement at nominal flexural strength.

Stress of unbonded tendon at nominal flexural strength cannot be calculated in the same method because behavior of unbonded tendon is affected by the compatibility of tendon elongation and the overall deformation of member. Several tests and analytical approaches have been performed to evaluate the stress of unbonded tendon in prestressed flexural members. **Table 2-1** presents equations of unbonded tendon stress at nominal flexural strength specified in codes, specifications, and previous studies (Yang and Kang, 2011; AASHTO, 2017; Garcia et al., 2017; ACI, 2019).

Table 2-1 Equations of nominal flexural stress (f_{ps}) in unbonded tendon

Reference	Equations
Yang and Kang (2011)	$$f_{ps} = \frac{-B_1 + \sqrt{B_1^2 - 4A_1C_1}}{2A_1} \leq f_{py}$$ $$A_1 = A_{ps}$$ $$B_1 = A_s f_y - A'_s f'_y - C_f - A_{ps} f_{ps} + \alpha_f E_p \varepsilon_{cu} A_{ps}$$ $$C_1 = \alpha_f E_p \varepsilon_{cu}(A_s f_y - A'_s f'_y - C_f - 0.85 f'_c b_w \beta_1 d_p) - f_{se}(A_s f_y - A'_s f'_y - C_f)$$ where, A_{ps}: area of prestressed reinforcement; A_s: area of non-prestressed reinforcement; b_w: width of member's web; C_f: simply taken as 0 for a rectangular beam; d_p: distance from extreme compression fiber to centroid of prestressing reinforcement; E_p: elastic modulus of prestressing reinforcement; f'_c: compressive strength of concrete; f_y: yield strength of non-prestressed reinforcement; β_1: ratio of depth of equivalent uniformly stressed compression zone assumed in strength limit state to depth of actual compression zone; and ε_{cu}: ultimate concrete compression strain
AASHTO (2017)	$$f_{ps} = f_{se} + 900\left(\frac{d_p - c}{l_e}\right) \leq f_{py} \quad \text{(ksi)}$$ $$l_e = \left(\frac{2L_T}{2 + N_s}\right)$$ $$c = \frac{A_{ps} f_{ps} + A_s f_s - A'_s f'_s - 0.85 f'_c (b - b_w) h_f}{0.85 f'_c \beta_1 b_w}$$ where, for rectangular section, b: width of member; c: distance from extreme compression fiber to neutral axis; f_{se}: effective stress in prestressing reinforcement after allowance for all prestress losses; h_f: compression flange depth; l_e: effective tendon length; L_T: length of tendon; and N_s: number of support hinges crossed by tendon

Garcia et al. (2017)	$f_{ps} = f_{se} + \dfrac{E_p}{L}(d_p - c)\theta$ $c = \dfrac{f_{ps,u}A_{ps} + P_v}{\beta_1 \beta_2 f'_m b}$ where, P_v: additional axial force; β_2: compression stress block depth factor; and f'_m: masonry strength
ACI 318-19 (2019)	for $l_n/h \le 35$, f_{ps} the least of: $f_{se} + 10{,}000 + \dfrac{f'_c}{100\rho_p}$ $f_{se} + 60{,}000$ f_{py} for $l_n/h > 35$, f_{ps} the least of: $f_{se} + 10{,}000 + \dfrac{f'_c}{300\rho_p}$ $f_{se} + 30{,}000$ f_{py} where, f_{py}: yield strength of prestressing reinforcement; h: overall thickness, height, or depth of member; l_n: length of clear span measured face-face of supports; and ρ_p: ratio of A_{ps} to bd_p

2.2 Structural fire safety design

2.2.1 Variation of material properties according to temperature

Materials that PT concrete consists of are generally concrete, tendon, and reinforcing bar. These materials experience mechanical and thermal property changes at high temperature, and the affected properties include strength, elastic modulus, conductivity, specific heat, and thermal expansion coefficient. Structural performance and safety have a relationship with material properties. It is crucial to recognize the effects of high temperature preemptively. In Eurocode and ASCE, material properties from ambient temperature (20°C) to high temperature (1,000-1,200°C) are introduced, and several researchers also studied effect of temperature. Relationships between material properties and temperature are shown in **Table 2-2** and **Table 2-3** (Lie and Lin, 1985; ASCE, 1992; EN1992-1-2, 2004; Kodur et al., 2004; Chang et al., 2006; Aslani and Bastami, 2011).

Table 2-2 Concrete property change at high temperature

Reference	Equation
	(a) Compressive strength (MPa)
ASCE Manual (1992)	$$f'_{cT} = \begin{cases} f'_c & 20°C \leq T \leq 450°C \\ f'_c\left[2.011 - 2.353\left(\dfrac{T-20}{1,000}\right)\right] & 450°C \leq T \leq 874°C \\ 0 & T > 874°C \end{cases}$$
	where, f'_c: compressive strength of concrete in room temperature; f'_{cT}: compressive strength of concrete according to temperature; and T: material temperature
BS EN 1992-1-2 (2004)	$$f'_{cT} = \begin{cases} f'_c & T \leq 100°C \\ f'_c(1.067 - 0.00067T) & 100°C \leq T \leq 400°C \\ f'_c(1.44 - 0.0016T) & T \geq 400°C \end{cases}$$
Kodur et al. (2004)	$$f'_{cT} = \begin{cases} f'_c[1.0 - 0.003125(T-20)] & T < 100°C \\ 0.75f'_c & 100°C \leq T \leq 400°C \\ f'_c(1.33 - 0.00145T) & T > 400°C \end{cases}$$
Aslani and Bastami (2011)	$$f'_{cT} = f'_c\begin{cases} 1.012 - 0.0005T \leq 1.0 & 20°C \leq T \leq 100°C \\ 0.985 + 0.0002T - 2.235\times10^{-6}T^2 + 8\times10^{-10}T^3 & 100°C < T \leq 800°C \\ 0.44 - 0.0004T & 900°C \leq T \leq 1,000°C \\ 0 & T > 1,000°C \end{cases}$$

<table>
<tr><td colspan="2" align="center">(b) Tensile strength (MPa)</td></tr>
<tr>
<td>BS EN
1992-1-2
(2004)</td>
<td>

$$k_{ck,t} = \begin{pmatrix} 1 & 20°C \le T \le 100°C \\ 1-(T-100/500) & 100°C < T \le 600°C \end{pmatrix}$$

$$f_{crT} = k_{ck,t} f_{cr}$$

where, f_{cr}: tensile strength of concrete in room temperature; $f_{cr,T}$: tensile strength of concrete according to temperature; and $k_{ck,t}$: degradation rate of concrete tensile strength according to temperature
</td>
</tr>
<tr>
<td>Chang et al.
(2006)</td>
<td>

$$f_{cr,T} = f_{cr} \begin{pmatrix} 1.05 - 0.0025T & 20°C \le T \le 100°C \\ 0.80 & 100°C < T \le 200°C \\ 1.02 - 0.0011T \ge 0.0 & 200°C < T \le 800°C \end{pmatrix}$$
</td>
</tr>
<tr>
<td>Aslani and
Bastami
(2011)</td>
<td>

$$f_{crT} = f_{cr} \begin{pmatrix} 1.02 - 0.00098T \le 1.0 & 20°C < T \le 300°C \\ 0.965 - 10^{-3}T - 9 \times 10^{-7}T^2 - 3 \times 10^{-9}T^3 + 3.2 \times 10^{-12}T^4 & 300°C < T \le 900°C \\ 0 & T \ge 1,000°C \end{pmatrix}$$
</td>
</tr>
<tr><td colspan="2" align="center">(c) Elastic modulus (MPa)</td></tr>
<tr>
<td>Anderberg
and
Thelandersson
(1976)</td>
<td>

$$E_{cr,T} = 2 f'_{cT} / \varepsilon'_{cT}$$

where, $E_{cr,T}$: elastic modulus of concrete according to temperature; and ε'_{cT}: concrete strain according to temperature
</td>
</tr>
<tr>
<td>Aslani and
Bastami
(2006)</td>
<td>

$$E_{cr,T} = E_c \begin{pmatrix} 1.0 & 20°C \le T < 100°C \\ 1.015 - 0.00154T + 2 \times 10^{-7}T^2 + 3 \times 10^{-10}T^3 & 100°C < T \le 1,000°C \\ 0 & T > 1,000°C \end{pmatrix}$$

where, E_c: elastic modulus of concrete in room temperature
</td>
</tr>
<tr>
<td>Chang et al.
(2011)</td>
<td>

$$E_{cr,T} = E_c \begin{pmatrix} -0.00165T + 1.033 & 20°C < T \le 125°C \\ \dfrac{1}{1.2 + 18(0.0015T)^{4.5}} & 125°C < T \le 800°C \end{pmatrix}$$
</td>
</tr>
</table>

	(d) Thermal conductivity (W/mK)			

	(d) Thermal conductivity (W/mK)
Lie and Lin (1985) ASCE Manual (1992)	$$k_c = \begin{pmatrix} -0.000625T + 1.5 & 0°C \le T \le 800°C \\ 1 & T > 800°C \end{pmatrix}$$ where, k_c: thermal conductivity of concrete
BS EN 1992-1-2 (2004)	Upper limit $$k_c = 2 - 0.2451(\theta/100) + 0.0107(\theta/100)^2 \quad 20°C \le \theta \le 1,200°C$$ Lower limit $$k_c = 1.36 - 0.136(\theta/100) + 0.0057(\theta/100)^2 \quad 20°C \le \theta \le 1,200°C$$
Kodur et al. (2004)	$$k_c = (2 - 0.0011T) \times 0.85 \quad 0°C \le T \le 1,000°C$$
	(e) Coefficient of thermal expansion (m/mK)
Lie and Lin (1985) ASCE Manual (1992) Kodur et al. (2004)	$$\alpha_{c,T} = (0.008T + 6) \times 10^{-6}$$ where, $\alpha_{c,T}$: concrete coefficient of thermal expansion
	(f) Thermal capacity (J/m^{3}K)
Lie and Lin (1985) ASCE Manual (1992) Kodur et al. (2004)	$$\rho_c c_c = \begin{cases} (0.005T + 1.7) \times 10^6 & 0°C \le T \le 200°C \\ 2.7 \times 10^6 & 200°C < T \le 400°C \\ (0.013T - 2.5) \times 10^6 & 400°C < T \le 500°C \\ (-0.013T + 10.5) \times 10^6 & 500°C < T \le 600°C \\ 2.7 \times 10^6 & T > 600°C \end{cases}$$ where, c_c: concrete specific heat; and ρ_c: concrete density

Table 2-3 Steel property change at high temperature

Reference	Equation
	(a) Yield strength (MPa)
ASCE Manual (1992)	$$f_{ys,T} = \begin{cases} f_{ys,0}\left[1.0 + \dfrac{T}{900\ln(\dfrac{T}{1750})}\right] & 0°C < T \leq 600°C \\[4mm] f_{ys,0}\dfrac{340 - 0.34T}{T - 240} & 600°C < T < 1,000°C \end{cases}$$
	where, $f_{ys,0}$: yield strength of steel in room temperature; $f_{ys,T}$: yield strength of steel according to temperature; T: material temperature
BS EN 1992-1-2 (2004)	$$f_{ys,T} = \begin{cases} 1 & T < 100°C \\ -1.933\times10^{-3}T + 1.193 & 100°C \leq T < 400°C \\ -0.6\times10^{-3}T + 0.66 & 400°C \leq T < 500°C \\ -1.8\times10^{-3}T + 1.26 & 500°C \leq T < 600°C \\ -1.05\times10^{-3}T + 0.81 & 600°C \leq T < 700°C \\ -2.5\times10^{-4}T + 0.25 & 700°C \leq T < 800°C \\ -1.25\times10^{-4}T + 0.15 & 800°C \leq T < 1,200°C \\ 0 & T \geq 1,200°C \end{cases}$$

	(b) Elastic modulus (MPa)	
ASCE Manual (1992)	$$E_{s,T} = \begin{pmatrix} E_{s,0}\left[1.0 + \dfrac{T}{2000\ln\left(\dfrac{T}{1,100}\right)}\right] & 0°C < T \le 600°C \\[4mm] E_{s,0}\dfrac{690 - 0.69T}{T - 53.5} & 600°C < T < 1,000°C \end{pmatrix}$$	
	where, $E_{s,0}$: elastic modulus of steel in room temperature; $E_{s,T}$: elastic modulus of steel according to temperature	
BS EN 1992-1-2 (2004)	$$E_{s,T} = E_s \begin{pmatrix} 1 & T < 100°C \\ -1\times10^{-3}T + 1.1 & 100°C \le T < 500°C \\ -2.9\times10^{-3}T + 2.05 & 500°C \le T < 600°C \\ -1.8\times10^{-3} + 1.39 & 600°C \le T < 700°C \\ -4\times10^{-4} + 0.41 & 700°C \le T < 800°C \\ -2.25\times10^{-4} + 0.27 & 800°C \le T < 1,200°C \\ 0 & T \ge 1,200°C \end{pmatrix}$$	
	(c) Thermal conductivity (W/mK)	
ASCE Manual (1992)	$$k_s = \begin{pmatrix} -0.022T + 48 & T \le 900°C \\ 28.2 & T > 900°C \end{pmatrix}$$	
	where, k_s: thermal conductivity of steel	
BS EN 1992-1-2 (2004)	$$k_s = \begin{pmatrix} 54 - 3.33\times10^{-3}T & T < 800°C \\ 27.3 & T \ge 800°C \end{pmatrix}$$	

	(d) Coefficient of thermal expansion (m/mK)
ASCE Manual (1992)	$$\alpha_s = \begin{pmatrix} (0.004T+12)\times10^{-6} & T<1{,}000°C \\ 16\times10^{-6} & T\geq1{,}000°C \end{pmatrix}$$ where, α_s: steel coefficient of thermal expansion
BS EN 1992-1-2 (2004)	$$\alpha_s = \begin{pmatrix} 1.2\times10^{-5}T+0.4\times10^{-8}T^2-2.416\times10^{-4} & T<750°C \\ 1.1\times10^{-2} & 750°C\leq T\leq860°C \\ 2\times10^{-5}T-6.2\times10^{-3} & 860°C<T\leq1{,}200°C \end{pmatrix}$$

	(e) Specific heat (J/kgK)
ASCE Manual (1992)	$$c_s = \begin{pmatrix} \dfrac{(0.004\times T+3.3)\times10^6}{\rho_s} & T\leq650°C \\ \dfrac{(0.068\times T+38.3)\times10^6}{\rho_s} & 650°C<T\leq725°C \\ \dfrac{(-0.086\times T+73.35)\times10^6}{\rho_s} & 725°C<T\leq800°C \\ \dfrac{4.55\times10^6}{\rho_s} & T>800°C \end{pmatrix}$$ where, c_s: specific heat of steel; and ρ_s: density of steel
BS EN 1992-1-2 (2004)	$$c_s = \begin{pmatrix} 425+7.73\times10^{-1}T-1.69\times10^{-3}T^2+2.22\times10^{-6}T^3 & T<600°C \\ 666+\dfrac{13002}{738-T} & 600°C\leq T<735°C \\ 545+\dfrac{17820}{T-731} & 735°C\leq T<900°C \\ 650 & 900\leq T\leq1{,}200°C \end{pmatrix}$$

2.2.2 Standards for fire tests

Performance of structural members under fire-exposure conditions is critical in protecting residents. Tests are conducted by authorities and academic organizations to verify the extent of structural safety and behavior under fire. In the process of testing, it is necessary to specify standards of testing in terms of materials, situations, and conditions of exposure. ASTM E119 specified the standard for fire test conditions regarding the extent and severity of fire-exposed surfaces. The content of the standard includes test specimen dimensions, humidity, furnace temperature, temperature measurement, loading condition, and conditions of acceptance. **Figure 2-1** shows the standard time-temperature curve (ISO 834) of the furnace. **Table 2-4** is a design guide for loading conditions and one-way slab specimen details. Furthermore, ASTM E119 guides conditions of acceptance involving deflection and deflection rate standards as indicated in **Table 2-5** and specifies the assessment of fire performance with fire-resistance time.
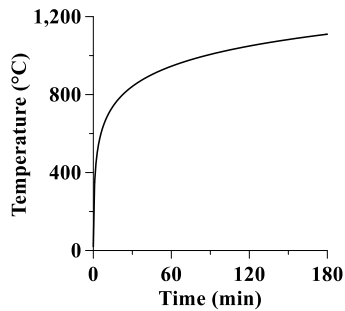
Figure 2-1 ISO 834 standard fire (ISO, 1999)

Table 2-4 Standards for loading conditions and design details (ASTM, 2020)

(a) Loading of floors and roofs
Throughout the fire-resistance test, apply a superimposed load to the test specimen to simulate a maximum-load condition. This load shall be the maximum-load condition allowed under nationally recognized structural design criteria unless limited design criteria are specified and a corresponding reduced load is applied.
(b) Size and characteristics of test specimen
The clear span (L_c) of beam exposed to the fire shall be not less than 12 ft (=3.7 m) and the member shall be tested in a horizontal position. For specimens tested with a representative section of a floor or roof assembly, such sections shall be not more than 7 ft (=2.1 m) wide and symmetrically located with reference to the beam.

Table 2-5 Conditions of acceptance in fire tests (ASTM, 2020)

(a) Maximum total deflection
$$\frac{L_c^{\,2}}{400d}$$ where, L_c: clear span of beam; and d: distance from extreme compression fiber to extreme tensile fiber
(b) Maximum deflection rate per minute
$$\frac{L_c^{\,2}}{9,000d}$$
(c) Tension steel temperature limit
427°C
(d) Reinforcing steel temperature limit
593°C

2.3 Previous studies

2.3.1 Bailey and Ellobody (2009)

Fire tests on eight bonded PT concrete one-way slabs were conducted by Bailey and Ellobody (2009). In this research, the fire performance of structures was compared by setting duct type, aggregate type, and restrained conditions differently, although the geometry and prestressing of the test were designed to be identical. Also, two ambient temperature tests were conducted for comparison. The geometry of test specimens and instrumentations are depicted in **Figure 2-2**.
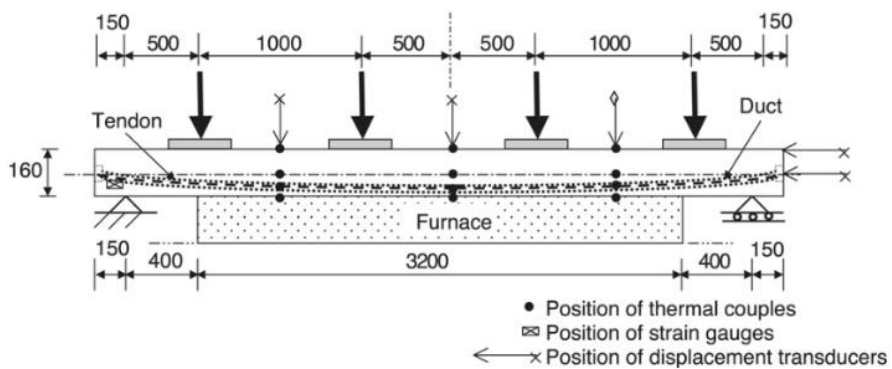
(a) Elevation view of specimen (unit: mm)
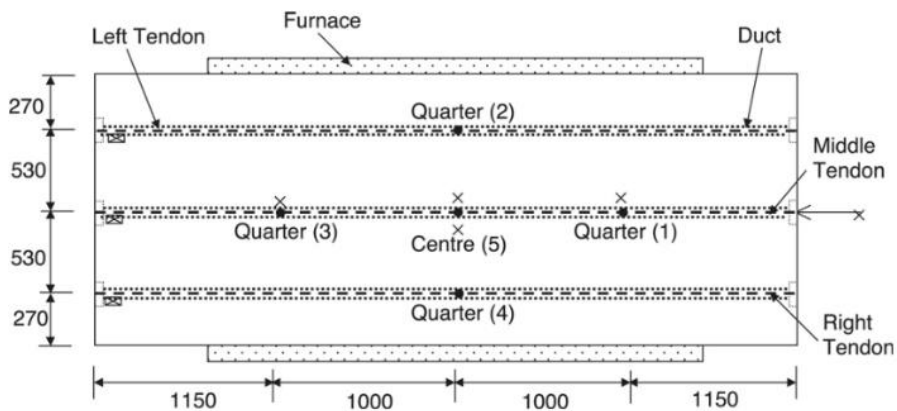
(b) Plan view of specimen (unit: mm)

Figure 2-2 Geometry and instrumentations of specimens
(Bailey and Ellobody, 2009)

Specimens were designed with a length of 4.3 m, a width of 1.6 m, and a depth of 160 mm, with a span length of 4.0 m. Ducts were installed in a second-degree parabolic shape with a 42 mm cover thickness in the middle lowest part. The tendon that was installed was a seven-plain mono-strand tendon with a diameter of 15.7 mm and an ultimate strength of 1,846 MPa. Three longitudinal ducts were placed, each with two tendons inside the duct. Temperature distribution, deflections in vertical and longitudinal directions, and tendon strains were all measured to analyze the fire performance of PT slabs. Static load was applied in four locations with spreader plates (1,600 × 350 × 40 mm) at a force of 78.3 kN (**Figure 2-2 (a)**). Specimens had two post-tensioning stages: (i) 50% of the design stressing load (97.5 kN) at four days after casting, and (ii) 70% of the breaking load (195 kN) that led to 169 kN after initial prestress loss at 14 days after casting. Variables that fire and ambient temperature tests are planned are shown in **Table 2-6**. Concrete cube strength and moisture content of specimens are presented in **Table 2-7**.

Table 2-6 Variables of tests (Bailey and Ellobody, 2009)

Test specimen	Fire	Longitudinal expansion		Duct		Coarse aggregate	
		Free	Restrained	Plastic	Metallic	Limestone	Thomas gravel
TB1		X		X		X	
TB2		X			X	X	
TB3	X	X		X		X	
TB4	X		X	X		X	
TB5	X	X		X			X
TB6	X		X	X			X
TB7	X	X			X	X	
TB8	X		X		X	X	
TB9	X	X			X		X
TB10	X		X		X		X

Table 2-7 Concrete cube strength and moisture content (Bailey and Ellobody, 2009)

Test Specimen	Aggregate type	Measured concrete strength at different days after casting (MPa)				Moisture content (%)
		4 days	14 days	28 days	At testing	
TB1	Limestone	32.3	39.2	40.0	41.2	-
TB2	Limestone	22.1	30.3	31.7	30.3	-
TB3	Limestone	25.2	36.4	39.4	36.6	1.19
TB4	Limestone	32.9	41.5	43.9	40.9	1.93
TB5	Thames gravel	24.0	35.0	35.3	35.5	1.07
TB6	Thames gravel	30.8	37.2	39.3	38.6	2.50
TB7	Limestone	29.2	36.0	39.1	40.4	2.43
TB8	Limestone	29.0	37.4	40.0	42.3	1.84
TB9	Thames gravel	26.5	35.3	38.9	36.9	2.27
TB10	Thames gravel	32.0	35.1	38.6	39.3	2.18

TB1 and TB2 are tests for comparison on fire test specimens that were conducted without temperature control. Both of them were unrestrained and had limestone aggregate. The duct type and concrete strength only differed. Tests for TB1 and TB2 were progressed with an increasing load from 36.7 kN to a failure load where end loads were 216 kN and 188 kN with a deflection in the vertical direction of 120 mm and 108 mm, respectively. In fire tests, not duct type but concrete strength influenced structural fire performance. **Figure 2-3** shows the load-central deflection curve for ambient slabs TB1 and TB2.
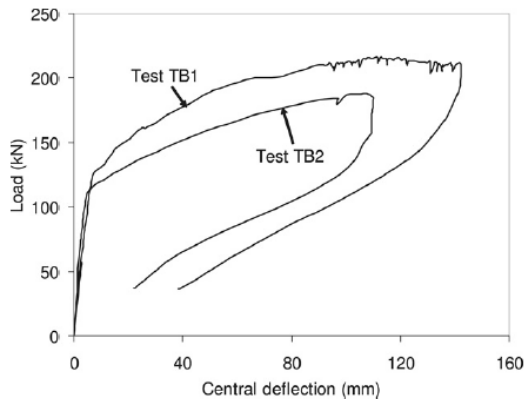

Figure 2-3 Load-central deflection curve for ambient slab TB1 and TB2
(Bailey and Ellobody, 2009)

Fire behaviors of PT concrete slabs were estimated by analyzing the following test results: (i) time and temperature data when the crack propagated, (ii) vertical deflection and horizontal expansion variation, (iii) test termination, and (iv) concrete spalling. Summaries of fire test results are shown in **Table 2-8**, **Figure 2-4**, and **Figure 2-5**.

Longitudinal cracks that appeared directly above and parallel to the location of tendons showed similar trends in propagation time and tendon temperature. In all specimens, cracks propagated around 15 to 20 minutes after the test started, and tendon temperatures were near 100°C. According to the variables aforementioned in **Table 2-6**, vertical deflection and horizontal expansion (**Figure 2-4** and **Figure 2-5**) variation behaved differently. By contrasting in pairs: (TB3 and TB7), (TB4 and TB8), (TB5 and TB9), and (TB6 and TB10), it could be assessed that metallic ducts are more vulnerable to fire. Also, specimens manufactured with Thames gravel aggregate experienced more deflection and expansion than limestone types. The most influential variable was the restrained condition. Regardless of duct type or aggregate type, all restrained specimens suffered less deflection and expansion change in contrast to unrestrained specimens. This result is due to the repulsive force generated by the support that induces the arch action of the structure. The test aimed to endure fire for 90 minutes before the tendon temperature exceeded 400°C. As shown in **Table 2-8**, fire tests have shown that designed specimens are capable of 90-minute fire resistance.

Table 2-8 Summary of test results (Bailey and Ellobody, 2009)

Test specimen	Longitudinal crack			Test termination		Spalling
	Propagation time (min)	Temp. (°C)		Time (min)	Tendon Temp. (°C)	
		Furnace	Tendon			
TB3	15	726	112	95	400	X
TB4	19	758	109	97	400	X
TB5	16	716	102	80	400	Minor
TB6	15	701	105	86	400	Minor
TB7	17	728	104	99	393	X
TB8	15	718	108	98	366	Minor
TB9	15	722	100	94	372	Minor
TB10	14	697	96	90	382	Minor
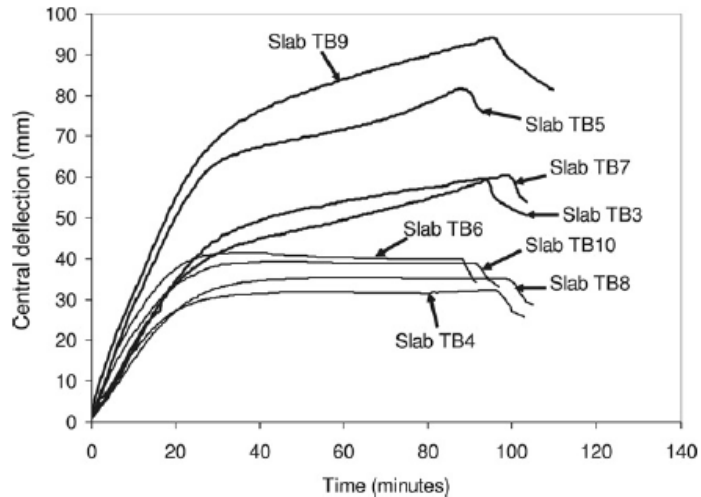
Figure 2-4 Time-central deflection curves for all fire tests
(Bailey and Ellobody, 2009)
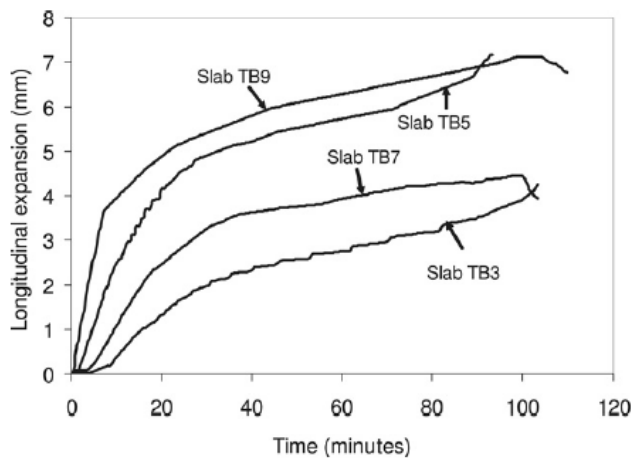
Figure 2-5 Time-longitudinal expansion for Slab TB3, TB5, TB7, and TB9
(Bailey and Ellobody, 2009)

From test results, the fire performance of bonded PT concrete slabs could be assessed. It can be determined that the sensitivity of variables for bonded PT concrete slabs is in order of restrained condition, aggregate type, and duct type. However, further investigations are required for specific explanations of differences resulting from duct type.

2.3.2 Hou et al. (2013)

Hou et al. (2013) tested nine unbonded prestressed concrete continuous slabs. The variables were concrete cover thickness, load level, effective prestress, and degree of prestressing. It was able to measure the degree of prestressing during the fire test since the test was conducted for unbonded PT series. Temperature, deflection, crack and spalling, failure time, and failure mode were all measured to assess the performance of continuous slabs after heating. Key characteristics and test parameters for slabs are shown in **Table 2-9**. Also, **Figure 2-6** presents the layout of steel bars and prestressing steel wires in UPCS-5.

Table 2-9 Key characteristics and test parameters in slabs (Hou et al., 2013)

Specimens	c_t (mm)	PPR	σ_{pe} (MPa)	η	f'_c (MPa)	w (%)	Width × depth (mm)
UPCS-1	15	0.35	657	0.37	56.9	3.98	600×70
UPCS-2	15	0.51	823	0.52	56.9	3.98	600×70
UPCS-3	15	0.68	1,019	0.62	48.2	3.50	600×70
UPCS-4	25	0.43	918	0.54	40.1	2.77	600×80
UPCS-5	25	0.53	972	0.36	52.1	2.36	600×80
UPCS-6	25	0.70	760	0.43	48.2	3.50	600×80
UPCS-7	30	0.40	1,000	0.43	52.1	2.36	600×85
UPCS-8	30	0.56	753	0.54	52.0	3.29	600×85
UPCS-9	30	0.69	830	0.37	52.0	3.29	600×85

Where, c_t: concrete cover thickness at critical section; PPR: degree of prestressing; σ_{pe}: effective prestress at ambient conditions; η: load level, defined as ratio of applied loading to capacity of slab at ambient conditions; f'_c: compressive strength of concrete in room temperature; and w: water content by weight
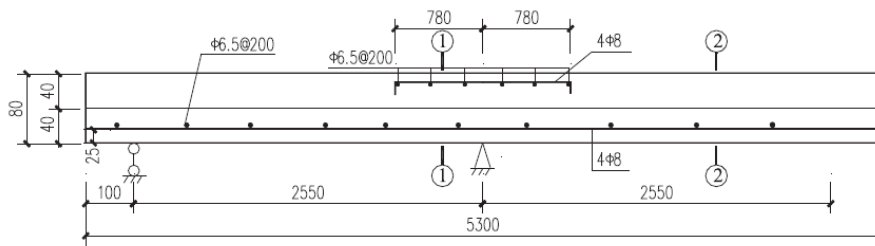
(a) Layout of steel bars (unit: mm)
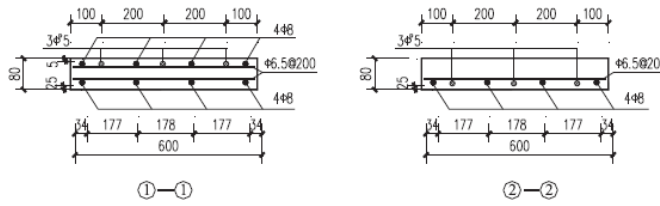
(b) Section view of steel bars (unit: mm)
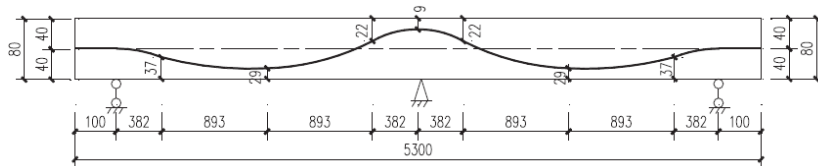
(c) Profile of prestressing steel wires (unit: mm)

Figure 2-6 Layout of steel bars and prestressing steel wires in UPCS-5
(Hou et al., 2013)

Figure 2-7 shows midspan deflections for nine slabs during and after fire tests. In the initial phase, deflection occurred due to thermal gradients developing in slabs. The intermediate phase also presented an increase in deflection that is because of a material property change. Lastly, at the cooling phase, deflection recovered with property recovery.

(a) USPC-1, USPC-2, and UPCS-3   (b) USPC-4, USPC-5, and UPCS-6

(c) USPC-7, USPC-8, and UPCS-9
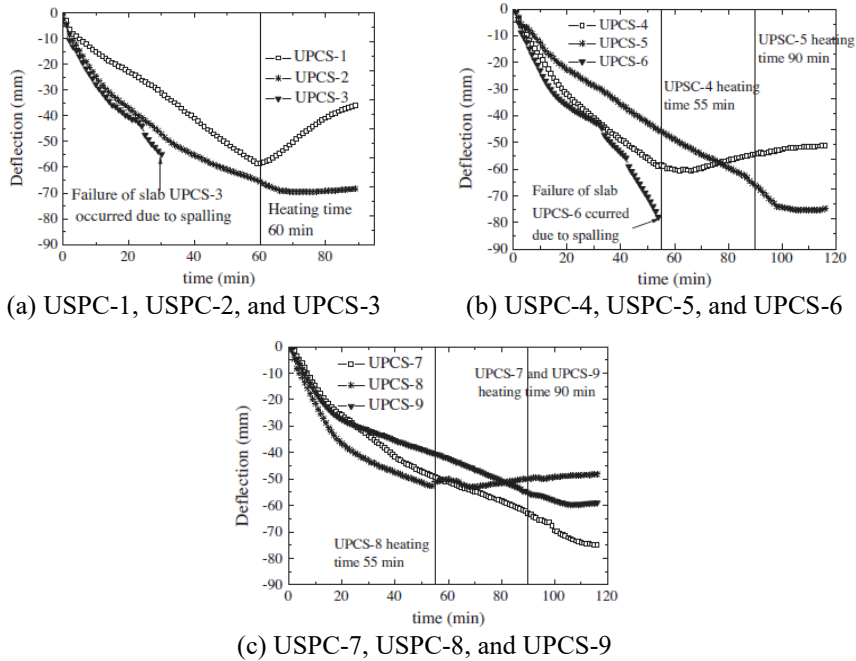
Figure 2-7 Midspan deflection-time response in different slabs
(Hou et al., 2013)

Hou et al. (2013) also measured time to stress graph divided into three stages as shown in **Figure 2-8**. The first stage is the time from 0 to 20 minutes after fire exposure. In all specimens, stress in prestressing steel wires increased during the first stage (in the range of 27 to 100 MPa). This is due to thermal gradients formulated by an increasing temperature that also cause deflections of slabs. The second stage is the time from 20 minutes to the end of the test. During this period, stress decreased conversely (11 to 330 MPa). Although thermal gradients develop, the strength and stiffness of the specimen would degrade as a result of the higher temperature. Eventually, this leads to a lower stress value. The third stage is the cooling phase, where stress decreases to a steady value due to recovery of modulus and creep strains.

(a) USPC-1, USPC-2, and UPCS-3   (b) USPC-4, USPC-6, and UPCS-8

(c) USPC-5, USPC-7, and UPCS-9
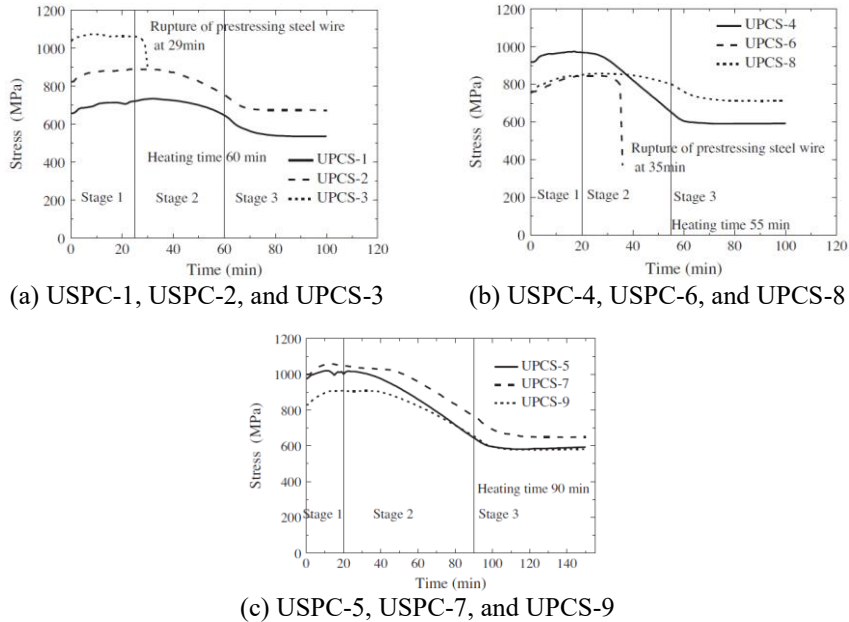
Figure 2-8 Development of stresses in prestressing steel wires of test slabs
(Hou et al., 2013)

In the fire tests conducted by Hou et al. (2013), concrete cover thickness and degree of prestressing were critical factors for fire resistance capacity. Tendon temperature change was affected by an increased concrete cover thickness, which is directly related to the structural performance. Also, if a high degree of prestressing was applied, the time for yielding and fracture of tendon and reinforcing bars was shortened. Furthermore, load level and reinforcement layout influenced the fire performance. High load level induced higher midspan deflection that also increased stress. All in all, factors that might affect the fire behavior of continuous slabs were discussed with fire tests.

2.4 Discussion

In this chapter, previous studies on the prestress of bonded and unbonded PT tendons were reviewed. Also, standards for fire tests and material properties according to temperature were discussed. Fire tests for bonded and unbonded cases were also investigated by examining test results. Summaries of contents are as follows:

1) Estimation of prestress at nominal flexural strength is significant since it affects the flexural strength of PT concrete slabs. For bonded tendons, stresses are calculated using the strain compatibility method. Whereas, unbonded tendons cannot directly assume with the method so that several researchers have devised equations based on experiment results. Yang and Kang (2011), AASHTO (2017), Garcia et al. (2017), and ACI 318-19 (2019) have come up with methods for unbonded tendon.

2) Concrete and steel properties deform substantially at high temperature. For fire safety design, a variation of properties should be considered. Therefore, prior researchers have studied high-temperature characteristics and presented relationships between material properties and temperature (Lie and Lin, 1985; ASCE, 1992; EN1992-1-2, 2004; Kodur et al., 2004; EN1993-1-2, 2005; Chang et al., 2006; Aslani and Bastami, 2011). The given equations can be used to predict the fire behavior of one-way slabs in fire tests or for numerical analysis.

3) Bailey and Ellobody (2009) conducted fire tests on eight bonded PT concrete one-way slabs. The variables used in tests were duct type, aggregate type, and restrained conditions. The Test aimed to evaluate the importance of variables on fire behavior, and in particular, restrained conditions were determined as the most significant factor. Thus, boundary conditions to be restrained or unrestrained would be crucial in designing fire tests.

4) Hou et al. (2013) tested nine unbonded prestressed concrete continuous slabs. The variables were cover thickness, load level, effective prestress, and the degree of prestressing. Cover thickness is related to thermal

conduction that makes the tendon have a low temperature at the same time and accordingly less deflection. Furthermore, since the slab was in an unbonded tendon system, the test could measure stress changes with time flow. Three stages of stress development were measured, and further research is required to assess stress change and material property variation together.

5) Prior tests aimed to assess the fire behavior of PT slabs either installed with bonded or unbonded tendons. It was revealed that several variables would affect the performance of PT slabs under fire. However, comparisons between the two methods were not performed. Furthermore, the fact that the unbonded tendon method is diverse should be considered. Unbonded tendon methods are classified into unbonded bare-strand tendon and unbonded HDPE sheathed-strand tendon with or without duct. Therefore, in the following study, the influence of tendon configuration on fire behavior will be progressed.

Chapter 3. Specimen Design

In this chapter, the design process of eight specimens is presented. The specimen dimensions were designed based on ACI 318-19, IBC 2018, and ACI 423.10R-16 (ACI, 2016). Dimension of specimens was set to fit the specified test conditions. Also, load balancing, stress checking, and moment checking were conducted for design details. Specimens were designed with two variables considered: fire resistance rating and tendon configuration.

3.1 Specimen outline

3.1.1 Specimen dimension

ASTM E119-20 specifies one-way slabs with a length of at least 12 ft (= 3.7 m) (**Table 2-4**). However, PT concrete suffers from anchorage slip, significantly at the initial stage. A minimum length of specimen should be ensured so that tensile force remains near anchor even after anchorage slip occurs. Therefore, eight specimens were designed in a one-way slab by adjusting the length to the maximum within the available length in the test center. Fire safety research center, located in Hwaseong, South Korea, conducts slab fire tests with a heating length of 2, 4, and 6 m. A maximum heating length of 6 m was selected, and additionally hanging length was added according to KS F 2257-5 (KS, 2014) at a length of 0.25 m at both ends. In total, specimens had a length of 6.7 m, a span length of 6.2 m, and a heating length of 6 m.

In IBC 2018, slab cover thickness code is specified according to aggregate type and fire resistance rating. In this research, slabs were designed to endure two- and three-hour, respectively. Referring to IBC 2018, the cover thickness of slabs was designed to be 45 and 60 mm, respectively. Also, since specimens were designed to have the same stress effect throughout the whole area of specimens according to slab height, the distance from concrete centroid to prestressing

reinforcement (*e*) at the middle was designed to be the same length of 70 mm. Therefore, the height of specimens was designed to be 250 mm (two-hour) and 280 mm (three-hour) respectively.

3.1.2 Material plan

Material properties were determined using general data. In PT systems, high-strength concrete is used to endure stress induced by prestressing without crack propagation. Thus, the designed target concrete compressive strength was 40 MPa. In respect of tendon, Grade 270 15.2 mm diameter prestressing strands (A_p = 140 mm^2, f_{pu} = 1,860 MPa) were used as bare-strand tendon. The HDPE sheathed-strand tendon also had equal prestressing strands but with PT and HDPE coating, resulting in a total diameter of 18.98 mm. Assuming that equivalent forces are applied to strands regardless of tendon configuration, 0.80f_{pu} (1,488 MPa) was designed to be jacked. Reinforcing bars used in the specimens were SD400 (f_y = 400 MPa) with D10 and D12 diameters.

3.2 Tendon design

3.2.1 Tendon configuration

Tendon configuration was determined according to strand type, material composition, and duct presence. **Figure 3-2** shows the tendon configuration that is installed in specimens. Ducts used in the specimens were metal ducts with a width of 71 mm and a height of 23 mm (**Figure 3-1**). Filled in materials was cement grout or grease. In particular, for unbonded bare-strand tendon cases, by peeling off the coating, grease coating was achieved. By using this method, although duct was not filled with grease, it was expected to have similar condition to unbonded tendon with grease filled.

(a) Width   (b) Height
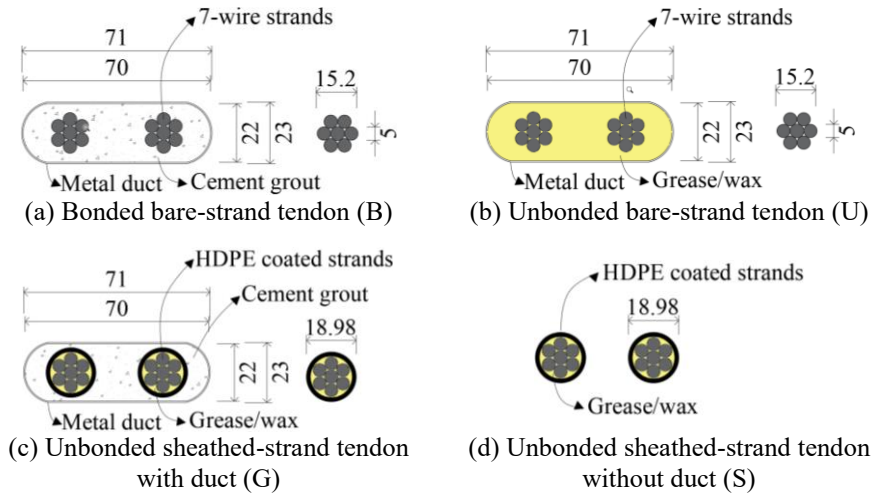
Figure 3-1 Metal duct

Figure 3-2 Tendon configuration installed in specimens (unit: mm)

3.2.2 Tendon layout

Tendon profile was designed with several parabolas through slabs, and only one configuration of tendon profile was used in specimens. **Figure 3-3** presents the profile of tendon. There were two types of specimens that had different heights. In total, the location where tendon is installed is different, but profile is the same. **Figure 3-3** shows half of the tendon layout that is symmetric about the centerline. Anchorage's location was at the center of gravity of concrete (c.g.c.), in the height of 125 and 140 mm, respectively. There were three inflection points (I.P.) designed in half of the specimen. The first point is 350 mm from anchorage. This point is where roller support is placed, and until the first I.P., heating load is not affected. Tendon profiled straight along the c.g.c. line from anchorage to the first I.P. Since then, considering negative moments near support, tendon profile was designed to have hogging curvature for the length of 600 mm, which is a tenth of the length of the heating length. Tendon profile was set for the rest of the section to reach its lowest point in an upward direction from the specimen's midpoint. This is the position corresponding to 55 and 70 mm from the bottom of the concrete section.
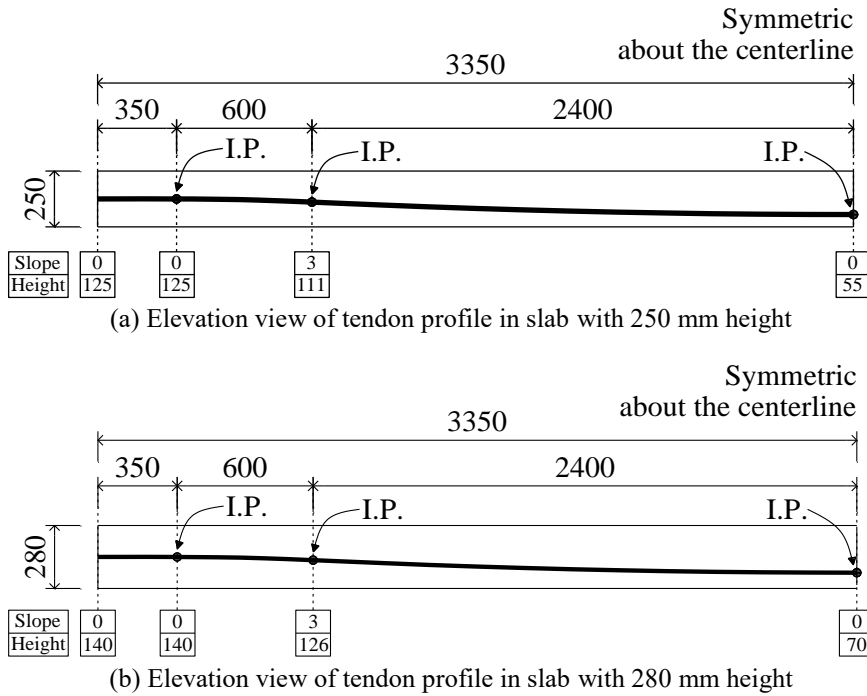
(a) Elevation view of tendon profile in slab with 250 mm height

(b) Elevation view of tendon profile in slab with 280 mm height

Figure 3-3 Tendon profile (I.P.: inflection point; unit: mm)

3.3 Specimen design

The number of tendons was determined using the load balancing method (Lin, 1963). For one-meter width, four tendons were required with a tendon profile as shown in **Figure 3-3**. Since specimens were designed to have a 1.5 m width, six tendons were determined to be installed. After determining the number of tendons, decision-making for service load followed. In fire tests, equal vertical loading was designed to be applied to all specimens. A loading plan was determined based on the bonded case designed for two hours fire resistance. Without consideration of reinforcing bars, the standard specimen had a moment capacity of 257.7 kN·m. In return, 40% of the moment capacity was set to be service load, which is 18 kN/m, for a total of 120 kN for the whole area. The next step was to check for stress according to ACI 318-19. By referring to Sections 24.5.2.1, 24.5.3.1, 24.5.3.2, and 24.5.4.1, the serviceability of specimens was checked. All specimens were classified as Class U, which is assumed to behave without cracking after tendon stressing. Meanwhile, since bonded and unbonded cases have different moment capacities (**Eq. (2-1)** and

Table 2-1), the reinforcing bar placement plan was set by designing all specimens within the same height to have equal moment capacity. In the process where the tendon installation plan was implemented, it was calculated that the moment capacity of bonded cases was larger by a value of 60 kN·m compared to unbonded cases. Accordingly, including the minimum reinforcing bar arrangement for ease of manufacturing specimens, two lower D13 longitudinal bars and two upper D10 longitudinal bars were planned for bonded cases, and eight lower D13 longitudinal bars and two upper D10 longitudinal bars were planned for unbonded cases. Further information on specimen design details is provided in **Table 3-1**, and a representative drawing (PF-B2) of specimens is shown in **Figure 3-5**. Drawings for all specimens are in Appendix A. Depending on the fire resistance rating and configuration of tendon, the IDs of specimens were determined as in **Figure 3-4**.
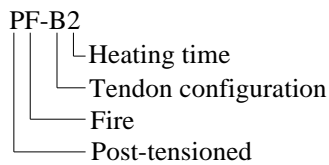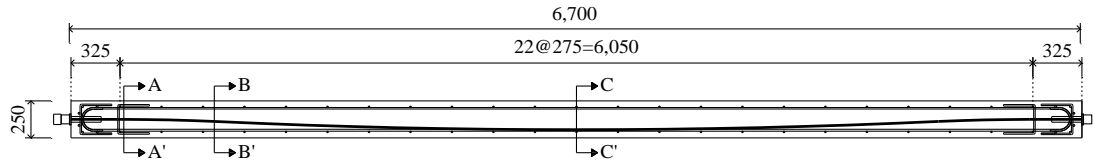
PF-B2
          └Heating time
   └Tendon configuration
      ├Fire
     └Post-tensioned

Figure 3-4 Nomenclature of specimens

Table 3-1 Test specimen details

| Specimen	PF-B2	PF-B3	PF-U2	PF-U3	PF-G2	PF-G3	PF-S2	PF-S3
Heating time (hr)	2	3	2	3	2	3	2	3
l (mm)	6,700	6,700	6,700	6,700	6,700	6,700	6,700	6,700
l_n (mm)	6,200	6,200	6,200	6,200	6,200	6,200	6,200	6,200
l_h (mm)	6,000	6,000	6,000	6,000	6,000	6,000	6,000	6,000
b (mm)	1,500	1,500	1,500	1,500	1,500	1,500	1,500	1,500
h (mm)	250	280	250	280	250	280	250	280
c_t (mm)	45	60	45	60	45	60	45	60
A_p (mm^2)	824.7	824.7	824.7	824.7	824.7	824.7	824.7	824.7
A_s (mm^2)	396.1	396.1	1,156	1,156	1,156	1,156	1,156	1,156
f'_c (MPa)	40	40	40	40	40	40	40	40
f_y (MPa)	400	400	400	400	400	400	400	400
f_{pu} (MPa)	1,860	1,860	1,860	1,860	1,860	1,860	1,860	1,860
f_{se} (MPa)	1,116	1,116	1,116	1,116	1,116	1,116	1,116	1,116
e (mm)	70	70	70	70	70	70	70	70

Where, A_p: area of prestressed longitudinal tension reinforcement; A_s: area of non-prestressed reinforcement; b: width of member; c_t: concrete cover thickness at critical section; e: distance from concrete centroid to prestressing reinforcement; f'_c: compressive strength of concrete in room temperature; f_{pu}: ultimate strength of prestressed reinforcement; f_{se}: effective stress in prestressing reinforcement after allowance for all prestress losses; f_y: yield strength of non-prestressed reinforcement; h: overall thickness, height, or depth of member; l: length of member; l_h: length of heating region; and l_n: length of clear span measured face-face of supports
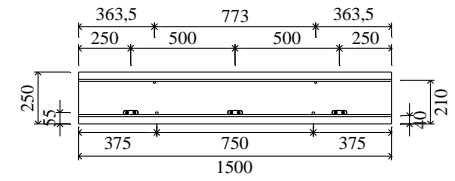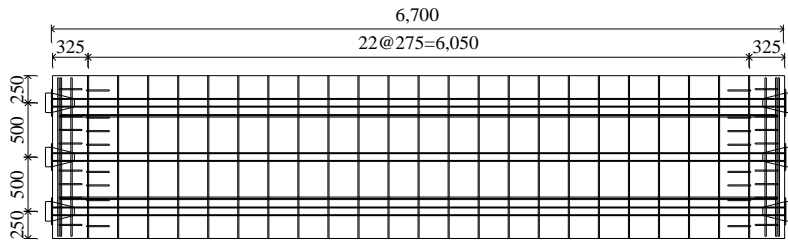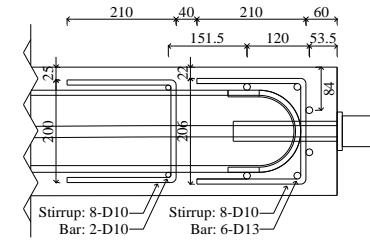
(a) Front view
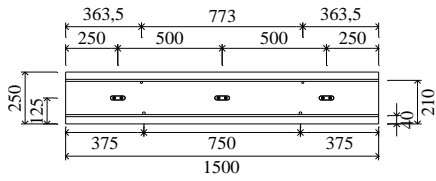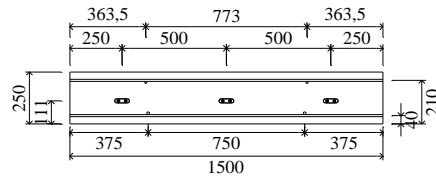
(b) Section A-A'   (c) Section B-B'   (d) Section C-C'

(e) Top view   (f) Anchorage detail

Figure 3-5 Representative specimen drawing (PF-B2; unit: mm)

36

3.4 Discussion

In this chapter, the detailed process of specimen design was introduced. Summaries of contents are as follows:

1) Referring to ASTM E119-20 and IBC 2018, the specimen dimension was designed within the experimental scale. Fire-resistance rating and cover thickness mainly influenced design decisions. Also, material properties were determined by referring to previous studies.

2) Tendon configurations are bonded bare-strand tendon (B), unbonded bare-strand tendon (U), unbonded sheathed-strand tendon with duct (G), and unbonded sheathed-strand tendon without duct (S). All specimens had equivalent tendon profiles with anchorage at the c.g.c. line. The distance from c.g.c. to prestressing reinforcement was the same for all specimens. Cover thickness was designed differently depending on the fire resistance rating, which made two types of specimen height.

3) All specimens were designed symmetrically about the center of the slab, and the number of tendons was designed to be the same. Determination of service load and stress check was conducted referring to ACI 318-19. The purpose of specimens was to compare fire resistance performance; therefore, the moment capacity of specimens was controlled to be equivalent by modifying the number and layout of reinforcing bars.

Chapter 4. Specimen Construction and Test Setup

In this chapter, the process of specimen construction is introduced. Also, test setup conditions are presented. All specimens were constructed in a precast factory in Yeoju, Korea. Since the length and width of specimens were all identical, but the height differed between two types, there were two types of formwork. Specimen test setup was designed based on ASTM E119-20 and KS F 2257-5.

4.1 Specimen construction

Specimens were constructed in the order of PF-B, PF-U, PF-G, and PF-S within two weeks. The steps of manufacturing process are shown in **Figure 4-1**. Reinforcing bar placement was identical for all specimens. Two wooden forms were placed at different heights to equalize the concrete curing conditions depending on strand type. Assembled reinforcing bars were fabricated on top of wooden forms, and then tendons were placed. Tendon parabola profile was fixed by using stair-shaped steel wires. After placement of reinforcing bar and tendon, the installation of thermocouples followed. **Figure 4-2** depicts installation location details for K-type thermocouples.

Concrete casting followed after thermocouple installation. Specimens were steam cured for a day, and then a twenty-five-day of curing period followed before tendon jacking. Strands were jacked by a hydraulic single-strand jack individually. The jacking force was set to be 0.80 f_{pu} (= 1,488 MPa). Only one side of the tendon was jacked, and the other was fixed. While jacking, tendon stressing force was measured using the self-made load cell (**Figure 4-3**). Note that jacking force can only be measured in unbonded cases. After jacking, specimens were delivered to a fire test center in Hwaseong, Korea.
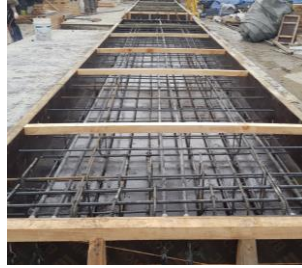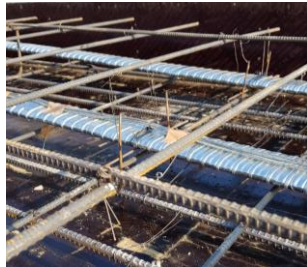
(a) Reinforcing bar assembly

(b) Wooden formwork

(c) Reinforcement bar and tendon placement (B,U, and G)

(d) Reinforcement bar and tendon placement (S)

(e) Thermocouple installation

(f) Concrete pouring

(g) Steam curing

(h) Removing formwork

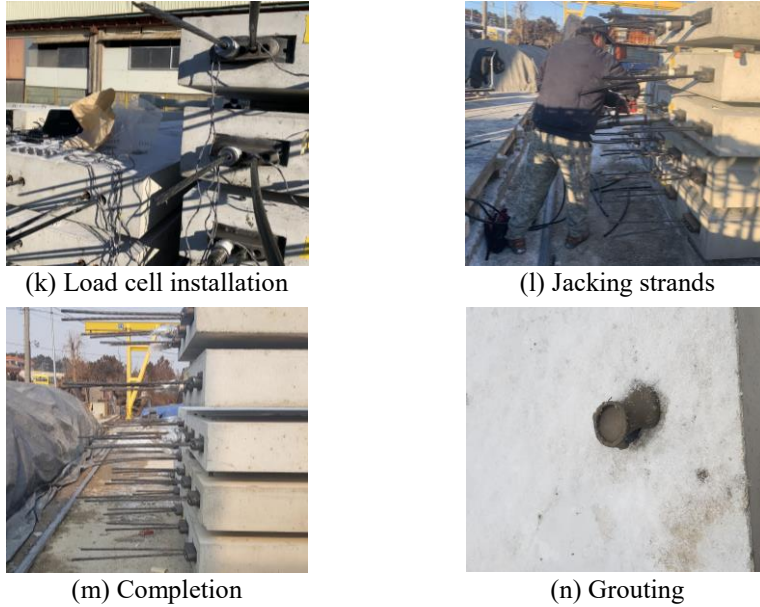(i) Tendon setting

(j) Jacking preparation

(k) Load cell installation

(l) Jacking strands

(m) Completion

(n) Grouting

Figure 4-1 Steps of manufacturing process
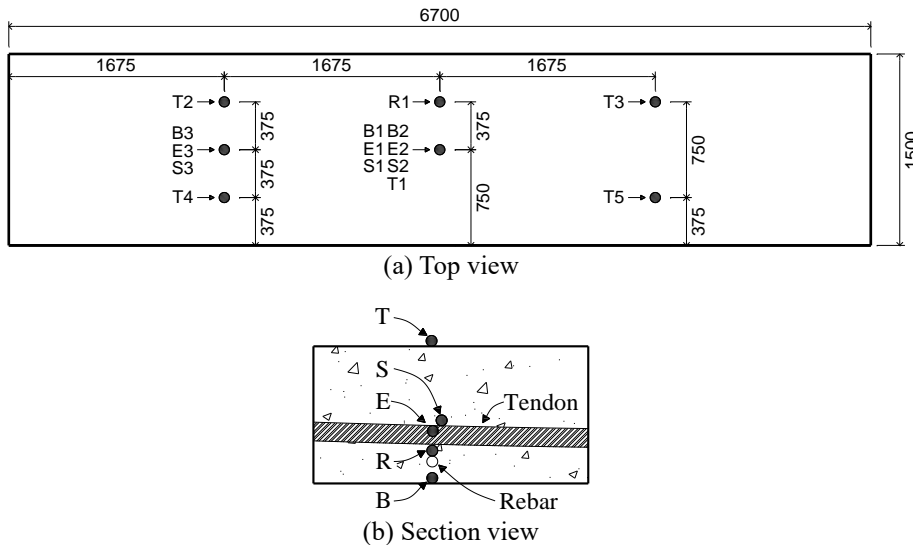

(a) Top view

(b) Section view

Figure 4-2 Location details of thermocouples (unit: mm)

Load cells were manufactured using S45C steel (outside diameter of 50 mm, inside diameter of 20 mm). Four strain gauges were attached along the outside diameter as shown in **Figure 4-3**. After the process of load cell manufacturing, calibration was performed to find the coefficient factor of load cells by applying force using Universal Testing Machine (UTM; **Figure 4-3**).

(a) Load cells manufactured
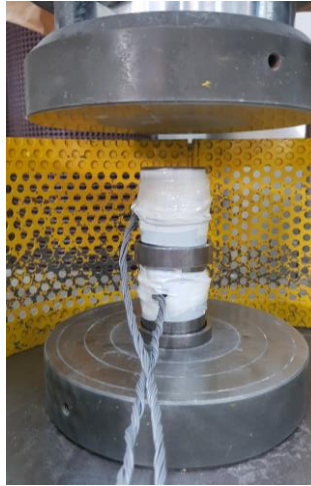
(b) Calibration

Figure 4-3 Self-made load cells

4.2 Tendon jacking

Tendon jacking was conducted two weeks after casting PF-S series. The compressive strengths of concrete at jacking date are shown in **Table 4-1**. In ACI 318-19, Section 24.5.3.1, concrete compressive stress limits are defined. Without service load, the maximum stress applied to the middle and end of the concrete by jacking force would be 3.98 and 2.45 MPa, respectively. With given concrete compressive stress data, all specimens satisfied the limit condition (minimum required concrete strength of 6.7 MPa). Also, as shown in **Figure 4-1**, no cracks occurred after jacking.

Table 4-1 Concrete compressive strength at jacking date

Specimens	PF-B	PF-U	PF-G	PF-S
Cure date	2020.12.14	2020.12.17	2020.12.21	2020.12.23
Jacking date	2021.01.06	2021.01.06	2021.01.06	2021.01.06
Duration (days)	23	20	16	14
Compressive strength (MPa)	26.2	40.2	46.0	30.0

Tendon jacking was conducted using a hydraulic single-strand jack with a target force of 200 kN. For unbonded cases, tendon stress at anchorages was measured using load cells. **Figure 4-4** shows the measured jacking stress data of specimens according to time. Jacking was done at the free end, and data measurement was conducted on both sides. As shown in **Figure 4-4**, all specimens were jacked to approximately 200 kN at their free end. At the fixed end on the other side, it was measured that the tensile force reached a level of 170 kN. This difference is thought to be the effect of friction loss occurring along the longitudinal direction. Anchorage slip was also measured. An anchorage slip occurred to have a loss of 30 to 40 kN, which is a 12 to 16% tensile force loss. Furthermore, the eigenvalue of tensile force was also measured using the direct method of logger sensor to estimate effective force at the test date that had a period of 29 to 49 days between jacking and testing.
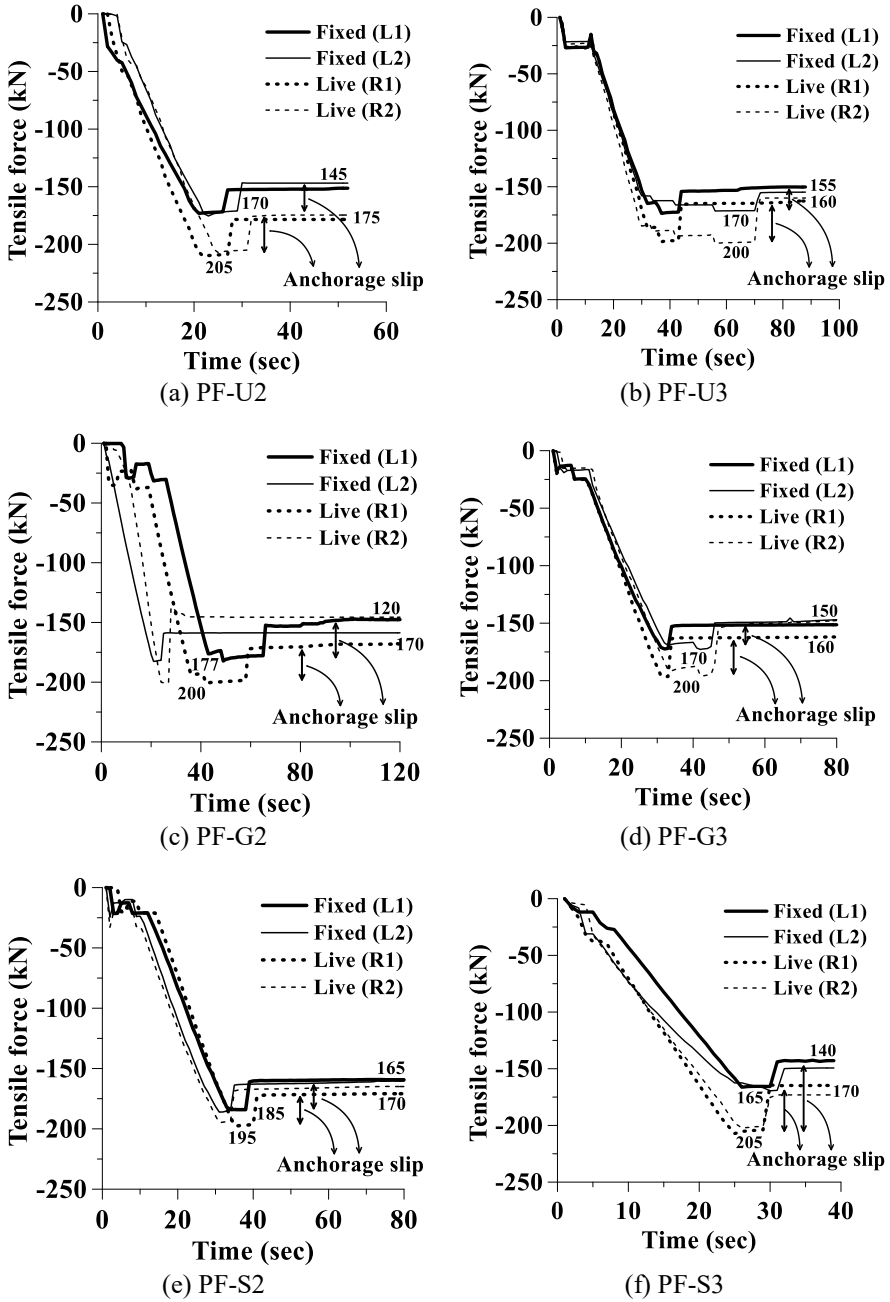
(a) PF-U2

(b) PF-U3

(c) PF-G2

(d) PF-G3

(e) PF-S2

(f) PF-S3

Figure 4-4 Jacking stress data of specimens

4.3 Material property

4.3.1 Strand

In specimens, one type of strand was used: SWPC 7B. Each tendon had seven strands, consisting of six strands with a diameter of 5 mm and one strand with a diameter of 5.2 mm. The six strands were twisted along a 5.2-diameter strand, and the tendon was designed to have an ultimate strength (f_{pu}) of 1,860 MPa. A tensile strength test was carried out for measuring material properties, and the measured stress-strain data is shown in **Figure 4-5**. The tensile strength test was successfully ended, and it was revealed that the tendon had a yield strength of 1,670 MPa, an ultimate strength of 1,896 MPa, and an elastic modulus of 200,000 MPa. The tendon tensile test setup is shown in **Figure 4-6**.
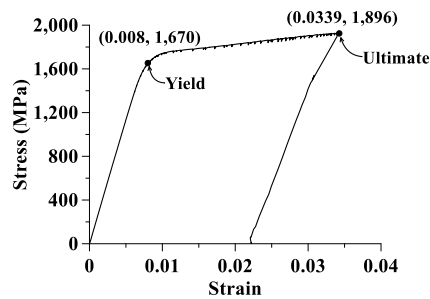

Figure 4-5 Strand stress-strain curve

Figure 4-6 Tensile strength testing

4.3.2 Reinforcing steel

One type of reinforcing steel was used in specimens with two types of diameter. SD400 steel with a yield strength of 400 MPa was used. Stirrups, hair pins, upper longitudinal bars, and temperature bars had a diameter of 10 mm, and lower longitudinal bars had a diameter of 13 mm.

4.3.3 Concrete

Cast-in-place high strength concrete with a nominal compressive strength of 40 MPa was used for specimens. Also, concrete pouring was conducted on four different days. The compressive strength of concrete was measured at the jacking date and the testing date using cylinder compression testing. Furthermore, concrete splitting tensile tests were also conducted to estimate the tensile strength of concrete. Three tests were conducted for each concrete type, and average values are shown in **Table 4-2**. Pictures of concrete cylinder testing are shown in **Figure 4-7**. Other concrete properties provided by the concrete mixing plant are shown in **Table 4-3**. Concrete elastic modulus was also calculated by measuring stress-strain data from cylinder compression testing. The measured concrete elastic modulus ranged from 14,797 to 23,733 MPa. According to ACI 318-19 Section 19.2.2.1, the elastic modulus of normal-weight concrete (E_c) can be calculated as 29,934.5 MPa when concrete's compressive strength is 40 MPa. However, the concrete compressive strength in the test was small due to severe curing conditions (steam curing and low temperature).
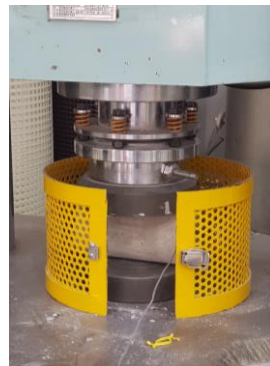
| (a) Compression test | (b) Splitting tensile test |

Figure 4-7 Concrete cylinder test

Table 4-2 Concrete cylinder test results

Specimen	Type	Age (days)	Compressive strength (MPa)	Elastic modulus (MPa)	Splitting tensile strength (MPa)
PF-B2	Jacking	23	26.2	14,797	2.7
PF-B2	Testing	44	42.0	14,797	2.7
PF-B3	Jacking	23	26.2	16,834	2.7
PF-B3	Testing	49	46.3	16,834	2.7
PF-U2	Jacking	20	40.2	23,733	2.8
PF-U2	Testing	35	46.7	23,733	2.8
PF-U3	Jacking	20	40.2	15,547	2.8
PF-U3	Testing	48	49.5	15,547	2.8
PF-G2	Jacking	16	46.0	20,415	3.1
PF-G2	Testing	29	49.1	20,415	3.1
PF-G3	Jacking	16	46.0	14,943	3.1
PF-G3	Testing	45	47.6	14,943	3.1
PF-S2	Jacking	14	30.0	16,297	2.6
PF-S2	Testing	33	36.5	16,297	2.6
PF-S3	Jacking	14	30.0	18,255	2.6
PF-S3	Testing	47	38.2	18,255	2.6

Table 4-3 Concrete mixture proportions and properties

Type	Unit	PF-B2	PF-B3	PF-U2	PF-U3	PF-G2	PF-G3	PF-S2	PF-S3
Cement density	kg/m^3	468	468	468	468	468	468	468	468
Fine aggregate density	kg/m^3	783	783	783	783	783	783	783	783
Coarse aggregate density	kg/m^3	953	953	953	953	953	953	953	953
High range water reduction agent density	kg/m^3	4.78	4.78	4.78	4.78	4.78	4.78	4.78	4.78
Water density	kg/m^3	165	165	165	165	165	165	165	165
Water-cement ratio	%	35.3	35.3	35.3	35.3	35.3	35.3	35.3	35.3
Slump	mm	150	150	150	150	150	150	150	150

4.4 Test setup and instrumentation plan

4.4.1 Test setup

Setting of the fire test is presented in **Figure 4-8**. Specimens were simply supported on two round-cylindrical supports. Dimensions of the furnace were $6 \times 2.4 \times 1.5$ m (length × width × height). In the furnace, a column was set to protect the furnace after a slab ruptured. A four-point actuator was used to apply load on a slab with a 1,050 mm interval. A force of 120 kN was applied using an actuator, which is 40% of the moment capacity of 250 mm thick slabs. For the same condition of all specimens, an equal load was also applied on 280 mm thick slabs. Insulated covers were laid next to the slab on both sides to block pressure and temperature loss. Photographs of the settings are shown in **Figure 4-9**. Heating condition of the furnace was set to follow the standard time-temperature curve specified in ISO 834 (**Figure 2-1**).
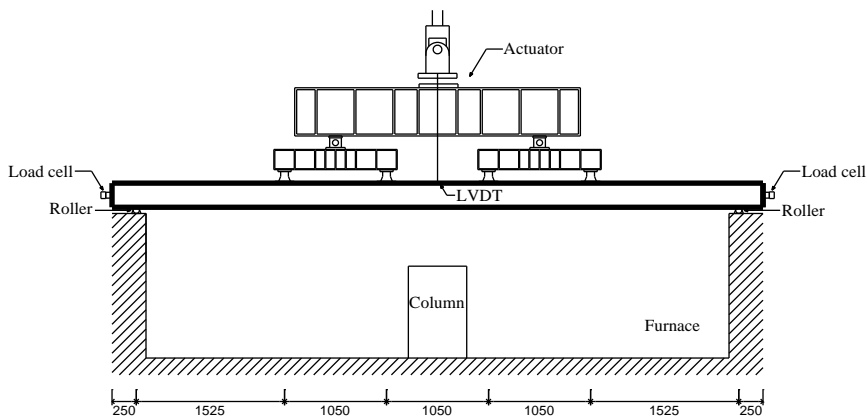

Figure 4-8 One-way PT slab test (unit: mm)

(a) Insulated cover

(b) Actuator

(c) Furnace

(d) Roller support

Figure 4-9 Test setup

4.4.2 Instrumentation plan

Load cells, LVDTs, and thermocouples were used to collect test data during fire tests. Load cells were installed at both ends of the slab in unbonded cases. Four load cells were installed in one slab, one in the center of the width and one in the quarter of each end, which corresponds to the location of anchorages. For each specimen, a single wire-LVDT was installed at the centroid of the upper face of the slab. This instrument was used to determine the vertical displacement of slabs. Each specimen was equipped with fifteen k-type thermocouples. **Figure 4-2** illustrates the installation location in detail. **Figure 4-10** shows photographs of the instrumentation.

(a) Load cell at support with anchor (PF-U, PF-G)

(b) Load cell at support without anchor (PF-S)

(c) Thermocouple

(d) Wire LVDT

Figure 4-10 Instrumentation

4.5 Discussion

In this chapter, specimen construction, tendon jacking, material properties, and test setup were illustrated. Summaries of contents are as follows:

1) Eight specimens were constructed in Yeoju, Seoul, at a precast factory. Reinforcing bar assembly, formwork, reinforcing bar and tendon placement, thermocouple installation, concrete pouring, concrete casting, and jacking were the sequence of construction. Load cells were made by hand using S45C steel and four strain gauges to measure tendon tensile force at jacking and fire tests.

2) Tendon jacking was conducted two weeks after the final specimen was cast in concrete. The target jacking force was 200 kN. Applied forces were measured using the load cells that were installed. Tensile force was measured for a while after jacking to 200 kN to measure the value of anchorage slip. It was revealed that 12 to 16% of the tensile force loss occurred after jacking. No cracking occurred after jacking.

3) SWPC 7B strands with an ultimate strength of 1,860 MPa were used for the specimens, along with the SD400 reinforcing steel bars with a yield strength of 400 MPa. The compressive strength of concrete was designed to be 40 MPa.

4) Specimens were placed in the furnace in a simply supported condition. To ensure complete filling of the furnace, the specimen's side was blocked with an insulating cover. The heating curve followed ISO 834 standard time-temperature curve, and a constant static load of 120 kN was applied to the slab throughout the test.

5) From fire tests, temperature, tendon tensile force, deflection, concrete spalling and delamination damage and extent, and crack pattern are obtained.

Chapter 5. Fire Test Results

In this chapter, the results of fire tests are reported. Fire test results were evaluated in terms of temperature (bottom and tendon), deflection, deflection rate, tendon tensile force, concrete crack propagation, concrete spalling, and concrete delamination by tendon.

In this thesis, the phrase "concrete spalling" refers to the phenomenon of concrete breakdown on the member surface caused by elevated temperature. Concrete spalling occurs mostly up to a thickness of 20 to 40 mm. In the current fire test, concrete spalling occurred mainly in the thickness of 20 mm due to the arrangement of bottom reinforcing bars, and had no significant effect on the fire resistance performance. The phrase "concrete delamination" refers to a significant degree of concrete breakdown caused by an increase in deflection (as a result of increased tendon tensile force and temperature) and degradation of material properties near the slab's anchors at both ends. Concrete delamination occurred up to a thickness of 260 mm, mostly due to tensile stresses induced by curved tendons near anchor zone (thickness of 125 mm in two-hour specimens and thickness of 140 mm in three-hour specimens). In comparison to concrete spalling, concrete delamination led to the early termination of fire tests.

5.1 Input fire scenario

Domestic and international standards (ISO, 1999; KS, 2014; ASTM, 2020) specify the time-temperature curve of the furnace during fire resistance test as shown in **Eq. (5-1)**.

$$T_f = 345 \log_{10}(8t + 1) + 20 \tag{5-1}$$

Where, T_f is average temperature of inside of furnace, and t is test time.

The input fire scenarios of eight fire tests were all designed to follow the ISO 834 standard fire curve. The time-temperature curves of inside of furnace during each fire test are shown in **Figure 5-1**. Each furnace temperature matched well with the ISO 834 standard fire curve.
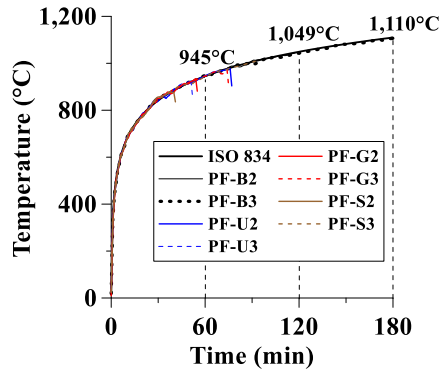

Figure 5-1 Input fire scenario of eight fire tests

5.2 Temperature variation

For each fire test, 15 k-type thermocouples were installed in the specimens at the bottom of slab, reinforcing bar, tendon, duct, and top of the slab. There were three thermocouples at the bottom, duct, and tendon in the middle (2) and quarter (1) locations. Five thermocouples were installed at the top of the slab at the center and four quarter points.

5.2.1 Time-temperature curves at the bottom of slab

Figure 5-2 illustrates the time-temperature curves for the PF-B2 and PF-U2 at the bottom of the slab as examples. Appendix B contains information of the time-temperature curves of all fire tests. Thermocouple nomenclature and position are shown in **Figure 4-2**. Although specimens were supposed to be uniformly exposed to fire during testing, the results indicate that heating propagated disproportionately on the bottom surface of slabs. The point is that the variation of curves is much different between the bonded (PF-B2) and unbonded (PF-U2) cases. This event occurs between 14 and 24 minutes after the start of the fire test. Concrete spalling is assumed to occur in three stages:

early spalling, intermediate spalling, and late spalling (Dwaikat and Kodur, 2009). Unbonded cases had concrete spalling across the entirety of the bottom surface, and the fluctuation period is presumed to be in the early stages of spalling. **Figure 5-3** shows the time range when early spalling occurred for unbonded cases.
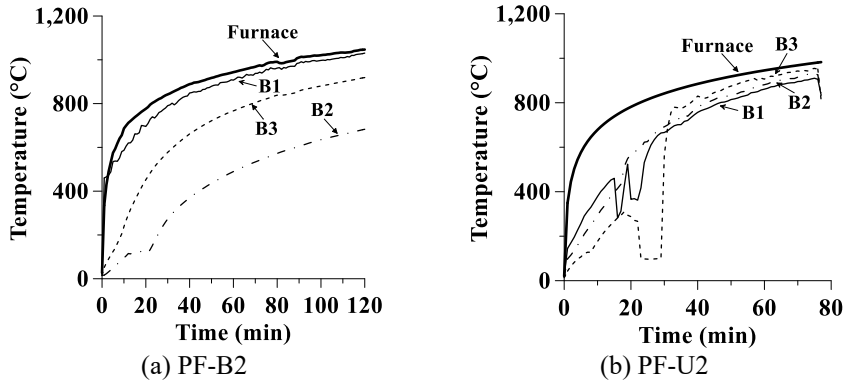

(a) PF-B2   (b) PF-U2

Figure 5-2 Time-temperature curves at bottom of the slab
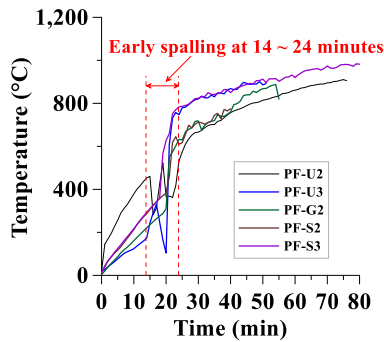
Figure 5-3 Time-temperature curves of unbonded cases

5.2.2 Time-temperature curves at tendon

The time-temperature curves of tendon are shown in **Figure 5-4**. For tendon configurations B, U, and G, temperature increase begins approximately 20 minutes after the fire test starts. Whereas the S type tendon experiences an increase in temperature from the start of the fire test. This distinction is brought about by the presence or lack of a duct. However, after a period of time during

53

which heat is delivered to the tendon, the temperature increase tendency of the tendon is identical. When tendon temperature reached 100-150°C, the rate of temperature growth slowed to a halt, referred to as the plateau stage. This is due to the evaporation of moisture from the tendon's surrounding area. For U, G, and S type, dropping point of grease near 70°C (ACI, 2014), resulted in a variance of the temperature increase tendency before reaching plateau stage. Increased cover thickness has an effect on the delay of temperature increase, as illustrated in **Figure 5-4 (c)**. Slower temperature conduction to the tendon indicates that the material properties of the tendon deteriorates more slowly and the tendon's fire resistance performance improves. The temperature of the PF-U3 and PF-S3 tendon increased after the plateau stage, and when the temperature reached 250°C, the fire test was stopped due to excessive deflection. Additionally, the temperature of the PF-G2 and PF-G3 tendons reached about 600°C at the end of the fire test with severe deflection. Except for the U type, higher cover thickness resulted in a longer fire-resistance period in unbonded cases, which is attributed to a slower temperature increase of the tendon.
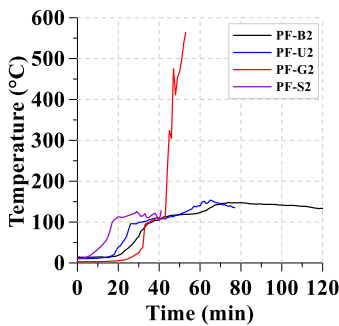
(a) Two-hour fire tests
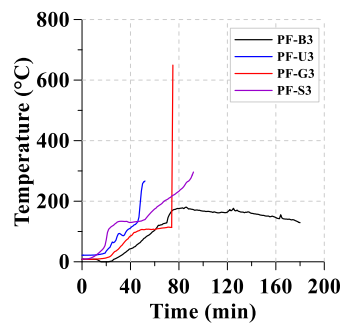
(b) Three-hour fire tests
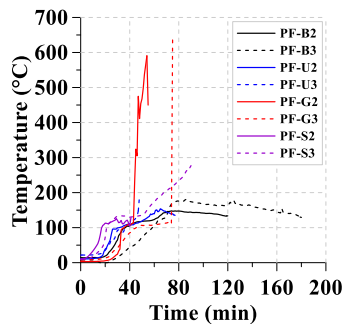
(c) Measured time-temperature curves at tendon

Figure 5-4 Time-temperature curves at tendon

5.2.3 Time-temperature curves for reinforcing bars

The time-temperature curves for reinforcing bars are shown in **Figure 5-5**. Due to the difference in degree of concrete spalling, even though thermocouples were installed at the same location, the temperature differed by tendon configurations.
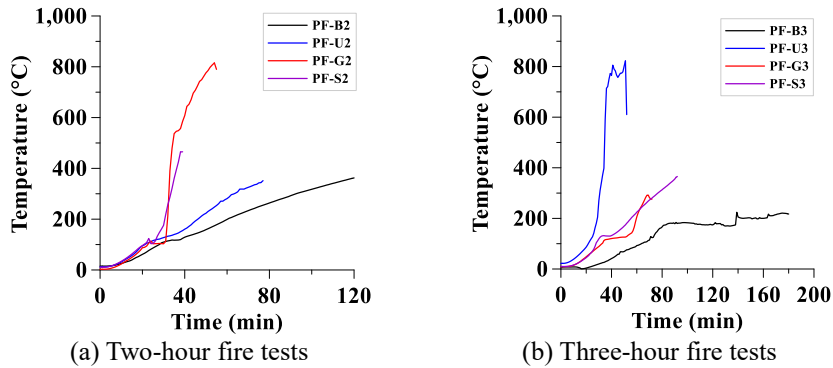

(a) Two-hour fire tests   (b) Three-hour fire tests

Figure 5-5 Time-temperature curves for reinforcing bars

5.3 Deflection and deflection rate variation

Time-deflection curves for two- and three-hour fire tests are shown in **Figure 5-6**, and time-deflection rate curves for two- and three-hour fire tests are shown in **Figure 5-7**. The fire testing was terminated when the deflection or deflection rate surpassed the ASTM E119 acceptance standards (**Table 2-5**). PF-U3 and PF-G2 exceeded at 52 and 55 min, respectively, in terms of deflection acceptance. Additionally, PF-U2, PF-U3, PF-G2, PF-G3, PF-S2, and PF-S3 exceeded at 76, 52, 55, 75, 42, and 91 min, respectively, in terms of deflection rate acceptance. The PF-B2 and PF-B3 fire tests were terminated after completing the target test time of 120 and 180 min, respectively.

For all tendon configurations, the time-deflection curve showed a consistent increase in deflection. All specimens were constructed to have the same capacities and same slab height (and same cover thickness), resulting in the same structural performance that may lead to similar tendency in deflection curve. Unbonded cases ruptured earlier than expected at various times. For two-hour fire testing, the order of failure time was PF-S2 (42 min), PF-G2 (55 min),

and PF-U2 (76 min). In three-hour fire testing, the order of failure time was PF-U3 (52 min), PF-G3 (75 min), and PF-S3 (91 min). It is notable that the fire endurance duration of the PF-U3 decreased to 67% of PF-U2 as the cover thickness increased, whereas PF-G3 and PF-S3 increased to 36 and 116% of PF-G2 and PF-S2, respectively. This appears to indicate that, despite thicker cover thickness, U type specimens were unable to withstand the fire due to increased self-weight and degradation of material properties. The values of deflection at the termination of fire tests for each specimen were 168 mm (PF-B2), 207 mm (PF-B3), 311 mm (PF-U2), 609 mm (PF-U3), 670 mm (PF-G2), 223 mm (PF-G3), 281 mm (PF-S2), and 173 mm (PF-S3).

Time-deflection rate curves showed a different tendency depending on tendon configuration, with the presence of a HDPE sheathing appearing to be influential. During two-hour fire tests, G and S types showed a deflection rate of 2.5 to 5 mm/min, whereas B and U types had a deflection rate of 5 to 10 mm/min. This difference became more pronounced as cover thickness increased. Prior to the sudden rupture, G type had a deflection rate of 0 to 2.5 mm/min, while S type showed a deflection rate of 0 to 2.5 mm/min with infrequent peak points (5 to 10 mm/min). In three-hour of fire tests, B type showed a stabilized deflection rate within the range of 0 to 5 mm/min, but U type showed a deflection rate of 5 to 12 mm/min with the earliest rupture time. Because strands of G and S types were sheathed with HDPE covering unlike those of B and U types which were bare mono-stand, it is believed that sheathing has an effect on the deflection rate of structures, which is related to fire performance.
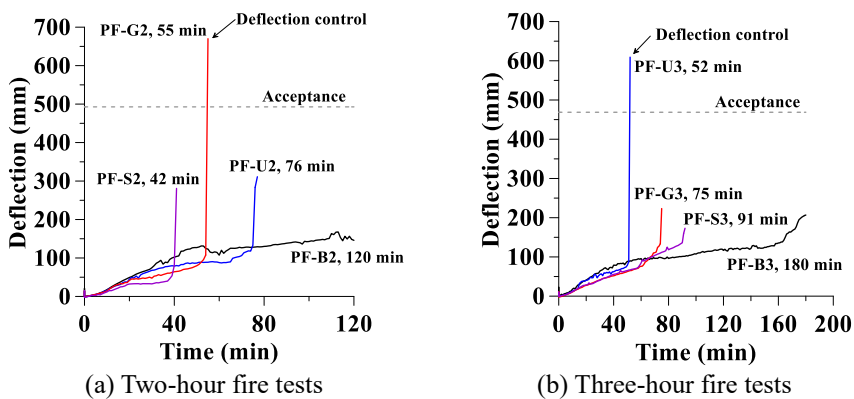

(a) Two-hour fire tests   (b) Three-hour fire tests

Figure 5-6 Time-deflection curves of fire tests

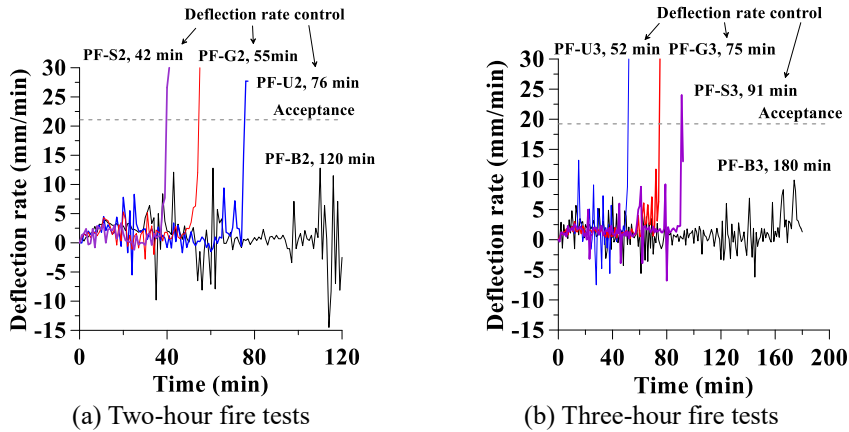(a) Two-hour fire tests   (b) Three-hour fire tests

Figure 5-7 Time-deflection-rate curves of fire tests

Two factors that contribute to the premature termination of fire tests are excessive tendon temperature and material property degradation. Tendon temperature-deflection curves are shown in **Figure 5-8** to determine failure criteria. **Figure 5-9** illustrates fractured tendons in unbonded cases following fire tests. For PF-G2 and PF-G3, the tendon temperature reached about 600°C, which is above the critical temperature for tendon specified in ASTM E119. Following the fire tests, the fractured tendon of PF-G2 and PF-G3 was examined as shown in **Figures 5-9 (c)** and **(d)**. High temperature of the tendon would induce significant material property loss, followed by fracture of the tendon, resulting in structure rupture. The tendon temperature reached 250°C and 300°C for PF-U3 and PF-S3, respectively. This is not the critical temperature at which the tendon will fracture as indicated in ASTM E119, but because the material properties of concrete decreased with increased temperature, loading generated excessive deflection of the structure. The fractured tendon of PF-U3 and PF-S3 is shown in **Figures 5-9 (b)** and **(f)**. The temperature of PF-U2 and PF-S2 tendons remained below 150°C; however, the structure ruptured. In these instances, it is estimated that the material property degradation of the concrete had a substantial effect on the structure's rupture. Although the tendon fractured as well, as shown in **Figures 5-9 (a)** and **(e)**, this would be owing to severe structural deflection.
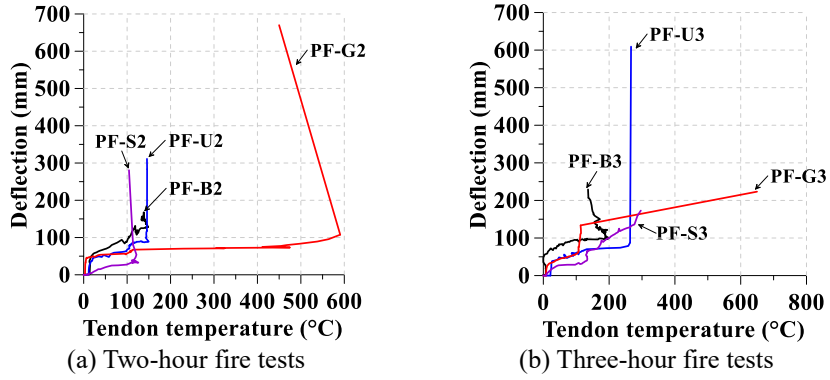
(a) Two-hour fire tests (b) Three-hour fire tests

Figure 5-8 Tendon temperature-deflection curves of fire tests

(a) PF-U2

(b) PF-U3

(c) PF-G2
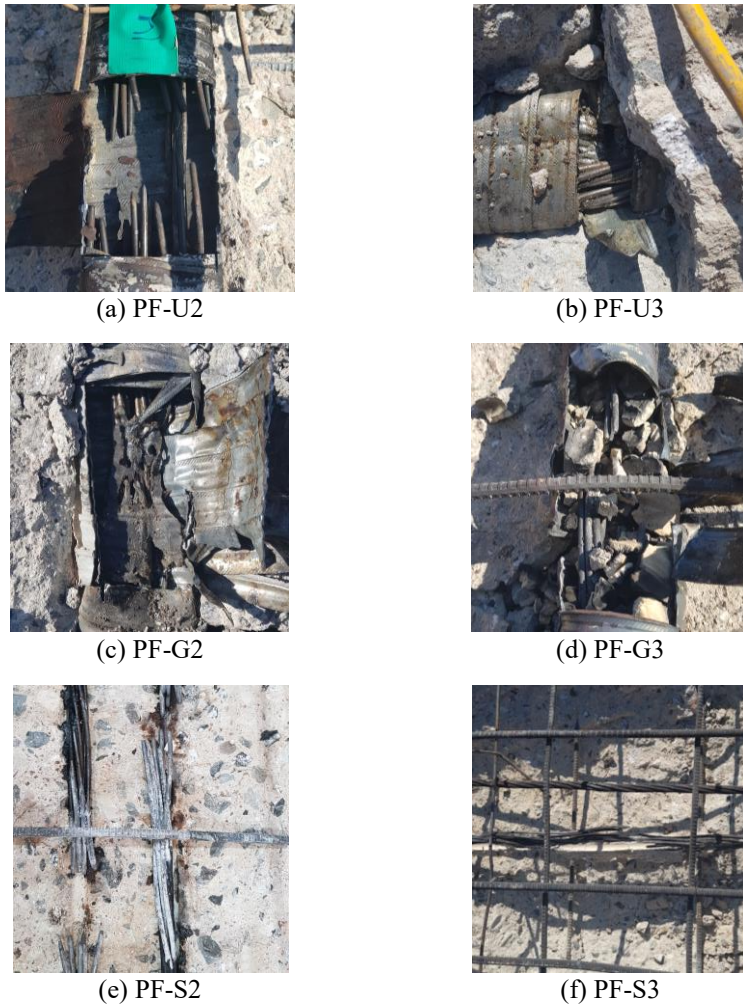
(d) PF-G3

(e) PF-S2

(f) PF-S3

Figure 5-9 Photographs of fractured tendons in unbonded cases

5.4 Tendon tensile force variation

Tensile force variation of tendon was measured for unbonded cases. Load cells made of S45C steel and four strain gauges were affixed to the fixed and free anchors at the slab's center and side locations. Following is the terminology for the position of the load cells: L denotes a fixed anchor, R denotes a free anchor, 1 denotes a center anchor, and 2 denotes a side anchor. The time-tendon tensile force curves for each tendon configuration are shown in **Figure 5-10**.

There was a consistent pattern of tensile force variation found across all fire test results. There were three stages: tensile force increase stage, tensile force decrease stage, and rupture stage. During the initial stage, the tensile force of the tendon gradually rose with time. Tensile force increased by 10 to 20 kN for 20 to 40 minutes following fire exposure. This is due to the slab's deflection that increased as the temperature increased. The second stage showed a gradual decrease in the tensile force of the tendon. Prior to the third stage, the tensile force restored to its initial value. A decrease in tensile force can be attributed to the degradation of mechanical properties (**Table 2-3**; strength and stiffness). Also, tendon deterioration caused by elevated temperature resulted in a decrease in tensile force. In the third stage, the tensile force of the tendon rapidly changed, resulting in the rupture of slabs. This is the period during which the deflection of the slab rapidly increased, either as a result of the tendon being directly exposed to fire or as a result of the structural failing to sustain load owing to mechanical property degradation. Tendon tensile force variation was in the range of 10 to 20 kN, which was similar for all tendon configurations.
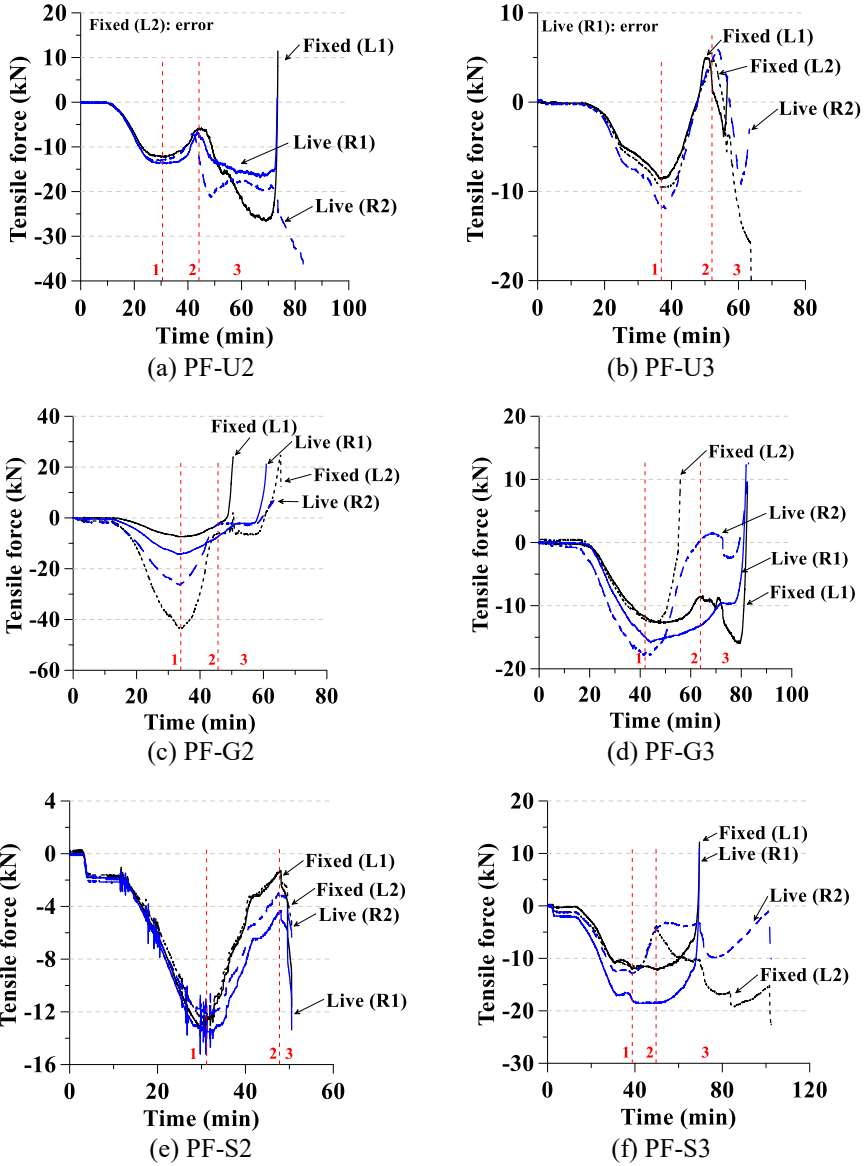
Figure 5-10 Time-tendon tensile force curves

5.5 Concrete crack propagation, spalling and delamination

5.5.1 Concrete crack propagation

After conducting fire tests, the propagation of concrete cracks was investigated. **Figure 5-12** shows the location and pattern of crack propagation on the specimen's side faces and top face, and **Figure 5-13** shows photographs of concrete cracks. The following types of concrete patterns were found in specimens: plastic shrinkage crack, flexural crack, and delamination crack. Plastic shrinkage cracks are evaluated to propagate as a result of free water evaporating from the concrete due to the elevated temperature. Water vapors were found at the top of the slab during fire testing when the tendon temperature exceeded 100°C. These voids serve as a channel for crack growth. In **Figure 5-12 (a)**, plastic shrinkage cracks are illustrated in the upper regions on both front and rear sides. Flexural cracks propagated from the center to both ends of the slab when specimen deflection increased due to vertical and fire loads. Flexural cracks and plastic shrinkage cracks were connected to create a larger crack, which conventionally resulted in cracks throughout the section, becoming a passageway for heat to penetrate to the tendon and duct and reducing the member's fire resistance performance. Delamination cracks propagated near support regions, as shown in **Figure 5-13 (b)**. **Figure 5-11** explains the procedure of delamination crack propagation. As shown in **Figure 5-5** and **Figure 5-10**, tendon tensile force increased with elevated tendon temperature. This increased tendon force augmented tensile force along the tendon direction. Tendon parabola is designed to have a negative slope near the support, resulting in a downward force (bursting force) acting on the concrete with a repulsive force upward. Due to the degraded concrete tensile strength by elevated temperature and augmented forces by increased tendon tensile force, a delamination crack propagated.
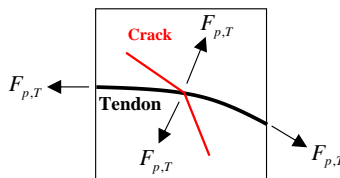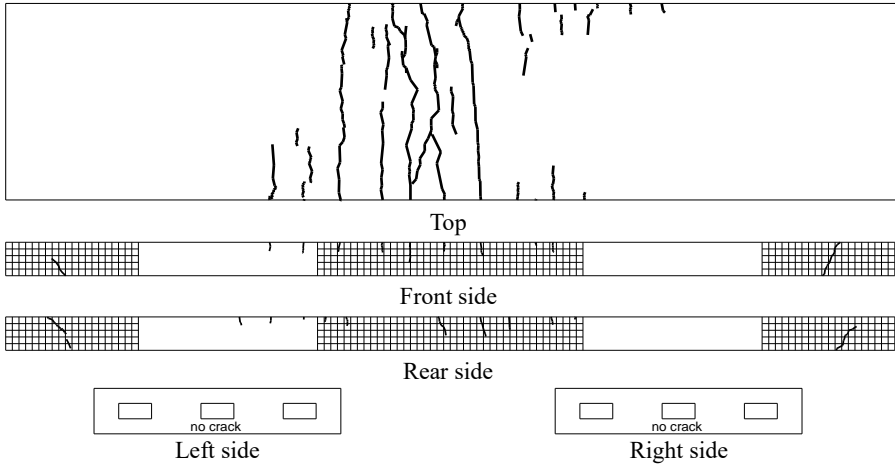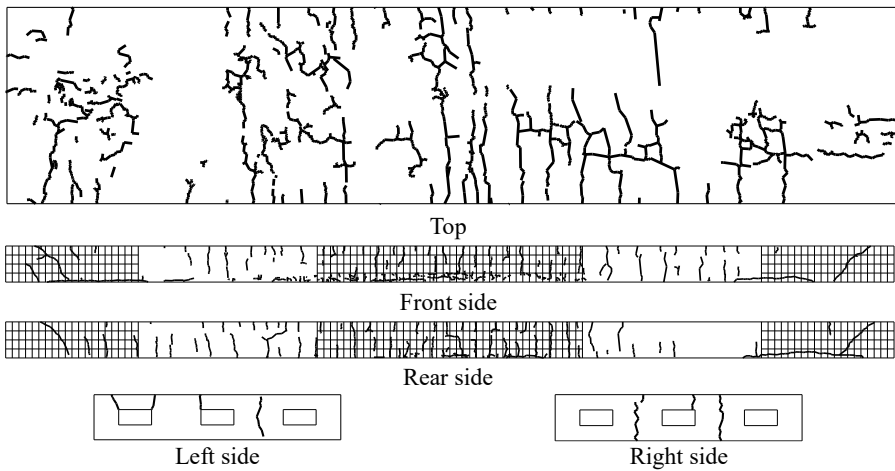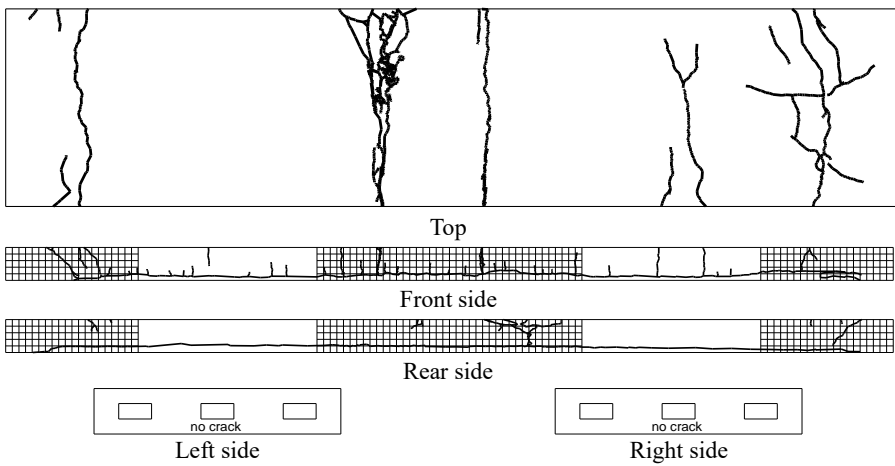
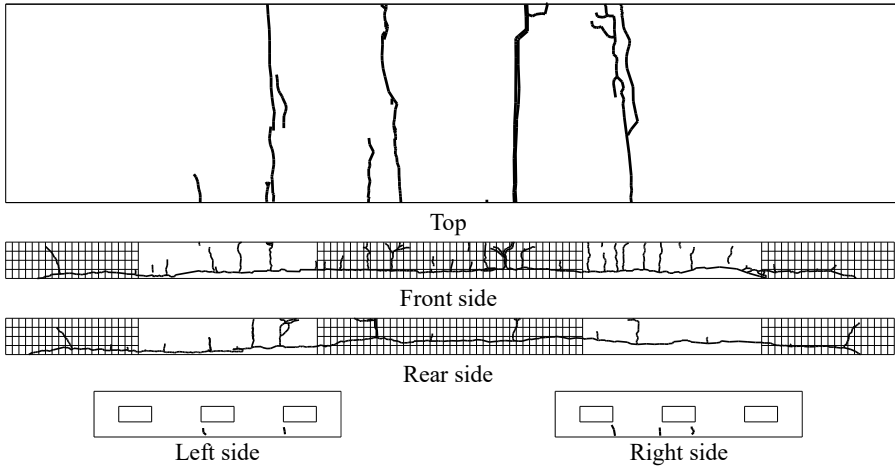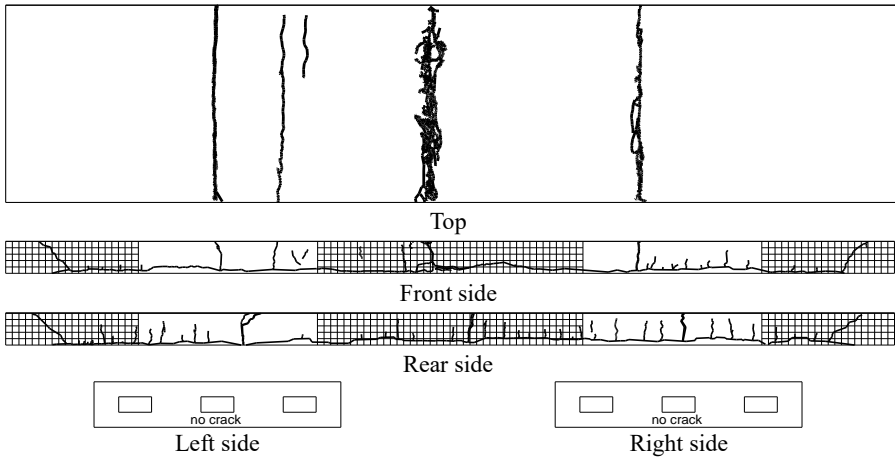**Figure 5-11** Delamination crack ($F_{p,T}$ is tendon tensile force)

Top

Front side

Rear side

no crack

Left side

no crack

Right side

(a) PF-B2

Top

Front side

Rear side

Left side

Right side

(b) PF-B3

Top

Front side

Rear side

no crack

Left side

no crack

Right side

(c) PF-U2

62

Top

Front side

Rear side

Left side   Right side

(d) PF-U3

Top

Front side

Rear side

Left side   Right side
no crack   no crack

(e) PF-G2

Top

Front side

Rear side

Left side   Right side
no crack

(f) PF-G3

Top

Front side

Rear side

Left side   Right side

(g) PF-S2

Top

Front side

Rear side

Left side   Right side

(h) PF-S3

Figure 5-12 Drawings of concrete cracks after fire tests
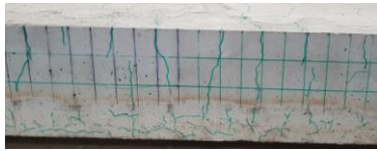
(a) Center region
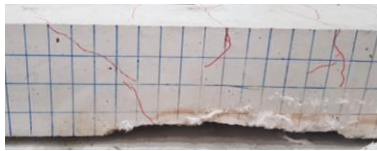
(b) Support region   (c) Anchor region

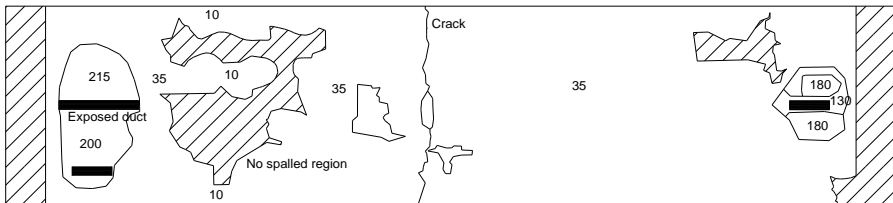**Figure 5-13** Photographs of concrete cracks

5.5.2 Concrete spalling and delamination

After fire tests, concrete spalling and delamination were observed on the bottom surface of each specimen. The damage and degree of concrete spalling and delamination are illustrated in **Figure 5-14**. Photographs of concrete spalling and delamination are shown in **Figure 5-15**. Minor spalling occurred regionally with depths of 20 to 65 mm in bonded cases. No concrete delamination occurred in PF-B2, while PF-B3 experienced concrete delamination at the anchor zone as a result of increased tendon tensile force and material stiffness degradation caused by elevated temperature. Concrete delamination depths in bonded cases ranged from 75 to 185 mm. Unbonded cases resulted in increased damage and degree of concrete spalling and delamination. Concrete spalling occurred in the majority of the bottom surface between 15 and 65 mm in depth, while concrete delamination occurred between 100 and 260 mm in depth near anchor regions. Specifically, the depth of concrete delamination in PF-U2, PF-G3, and PF-S3 was between 200 and 260 mm (approximately 80 to 90% of the original depth). This resulted in the duct and tendon being exposed to fire, as seen in **Figures 5-15 (c)** to **(d)**. According to the fire test results, unbonded cases show a greater variation in tensile force in the anchor zone than bonded cases (this could be due to the fact that bonded cases distribute stress from strand to grout to concrete in all regions simultaneously, whereas unbonded cases distribute stress starting from the anchor region to concrete), resulting in more severe concrete delamination at the anchor.
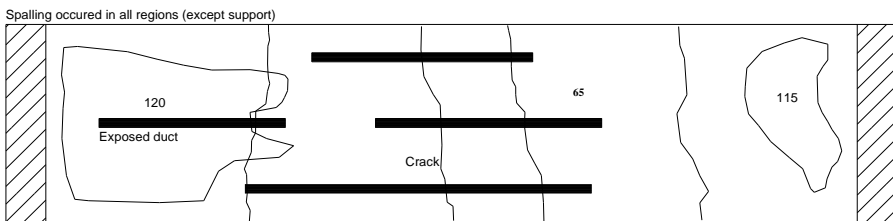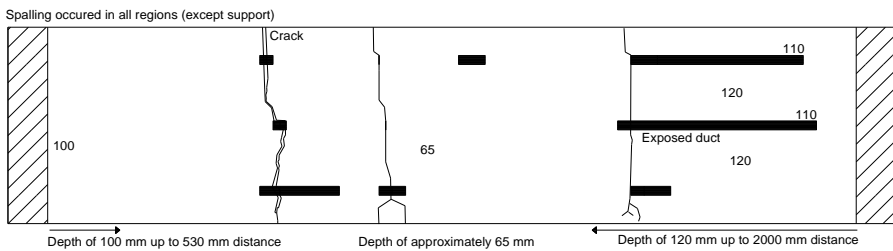
No spalled region

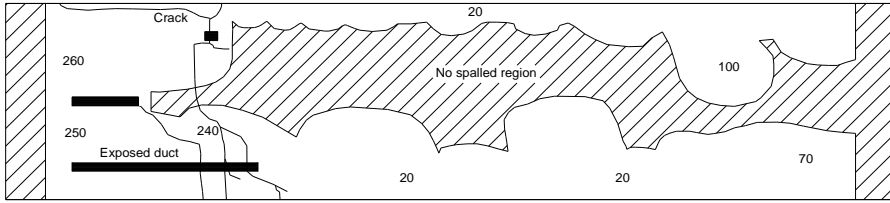Regional spalling

20 44

(a) PF-B2

20

75 80

135

85 20-40

185 85

94 85

No spalled region

(b) PF-B3

10

Crack

215 35

35 35

10

Exposed duct 180

200 130

180

No spalled region

10

(c) PF-U2

Spalling occured in all regions (except support)

120 65 115

Exposed duct

Crack

(d) PF-U3

Spalling occured in all regions (except support)

Crack 110

120

110

100 65 Exposed duct

120

Depth of 100 mm up to 530 mm distance   Depth of approximately 65 mm   Depth of 120 mm up to 2000 mm distance

(e) PF-G2

(f) PF-G3

(g) PF-S2
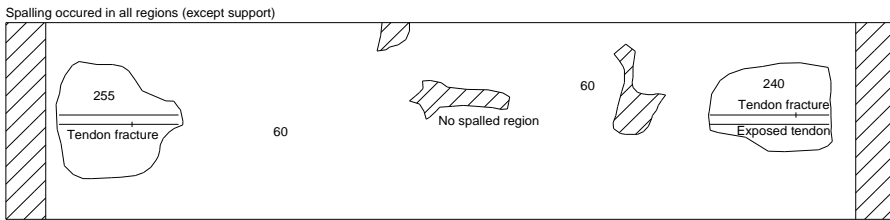
(h) PF-S3

Figure 5-14 Damage and degree of concrete spalling and delamination
(number indicates the depth of spalling and delamination; unit: mm)

(a) Delamination at anchor (bonded)

(b) Regional spalling

(c) Delamination at anchor (unbonded)

(d) Spalling at center

Figure 5-15 Photographs of concrete spalling and delamination

5.6 Discussion

In this chapter, the results of fire tests were illustrated. Summaries and discussions are as follows:

1) **Table 5-1** summarizes the results of the fire tests. Temperature, deflection, and tensile force of the tendon increased similarly for all tendon configurations, although deflection rate differed. Presence of the HDPE sheathing influenced on the degree of deflection rate. Deflection rate is one of the parameters considered when determining a structure's fire resistance performance. Thus, the use of G or S type tendon configuration is recommended in terms of fire resistance.

2) All specimens experienced three steps of tendon tensile force variation (increase, reduction, and rupture). This was attributed to the structure's increased deflection and material property degradation by the elevated temperature.

3) In bonded cases, regional spalling occurred at a depth of 20 to 65 mm. In unbonded cases, spalling occurred in most of the bottom surface area with a depth of 15 to 65 mm. Also, the majority of spalling was at a depth of 20 to 25 mm, which corresponds to the location of the lower reinforcing bar.

4) Delamination of concrete occurred at the anchor zone at depths ranging from 75 to 260 mm by bursting force (caused by tendons) and degraded concrete's stiffness (due to elevated temperature). However, when fire occurs in only a few regions in an actual structure, deflection occurs regionally with less tendon elongation in a continuous structure. Also, redundancy of one- or two-way slab structure and redistribution of stresses would prevent concrete delamination.

5) Stirrups are also believed to prevent concrete delamination (Choi et al., 2020) and PP (polypropylene) or NY (nylon) fibers may contribute to prevention of concrete spalling (Lee et al., 2012).

Table 5-1 Fire test results

Specimen		PF-B2	PF-B3	PF-U2	PF-U3	PF-G2	PF-G3	PF-S2	PF-S3
Test time (min)		120	180	77	52	55	75	41	92
End temp. (°C)	Bottom	1030	1098	954	900	887	747	844	982
	Tendon	145	136	147	267	591	650	128	296
Max. temp. (°C)	Tendon	145	199	150	272	591	650	128	296
Deflection (mm)		168	207	133	88	108	134	81	136
Deflection rate (mm/min)		5-10	0-5	5-10	5-12	2.5-5	0-2.5	2.5-5	0-2.5
Tensile force (kN)		Tensile force variation of 10-20 kN Stage 1 (increase) → Stage 2 (decrease) → Stage 3 (rupture)							
Crack propagation		Plastic shrinkage crack (upper side) Flexural crack (lower side) Delamination crack (near anchor region)							
Spalling		Regional		Majority (except support)					
		20-65 mm depth		15-65 mm depth					
Delamination		Only crack	Concentrated near anchor zone 75-260 mm depth						

Chapter 6. Numerical Analysis

In this chapter, numerical analyses for bonded PT slabs are performed. Heat transfer and thermo-mechanical stress analyses were performed using the ABAQUS (ABAQUS, 2014) finite element analysis (FEA) program. Throughout the chapter, the concepts of modeling, material property, and analysis are introduced.

6.1 Numerical modeling

Heat transfer and thermo-mechanical stress analyses were performed on three-dimensional models of post-tensioned concrete slabs, as seen in **Figure 6-1**. As shown in **Table 2-2** to **Table 2-3**, mechanical and thermal properties of concrete and steel were defined based on previous studies and standards.

(a) Slab

(b) Tendon　　　　　　　　　　(c) Reinforcing bar
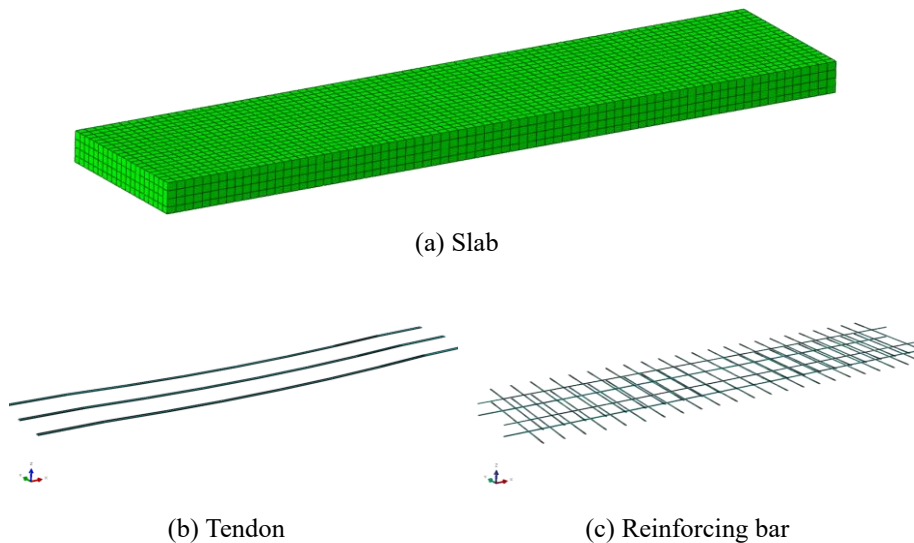
Figure 6-1 Three-dimensional numerical model

6.1.1 Concrete modeling

The mechanical behavior of concrete was defined using the damaged plasticity constitutive model (ABAQUS, 2014). The dilation angle, eccentricity (default value is 0.1), ratio of initial equibiaxial compressive yield stress to initial uniaxial compressive yield stress (σ_{b0}/σ_{c0}, default value is 1.16), ratio of the second stress invariant on the tensile meridian (K_c, default value is 2/3), and viscosity were defined using previous studies (Kang and Huang, 2012; Gao et al., 2013) in which the parameters were calibrated for post-tensioned structures and fire analysis (**Table 6-1**). Elastic modulus was defined to follow the research result of Bastami and Aslani (2011), and compressive and tensile stress-strain data were defined based on BS EN 1992-1-2 (2004). **Figure 6-2** shows the mechanical properties defined in numerical analysis for PF-B2.

Table 6-1 Concrete damaged plasticity constitutive model parameters

Dilation angle	Eccentricity	σ_{b0}/σ_{c0}	K_c	Viscosity
50	0.1	1.16	2/3	0.005
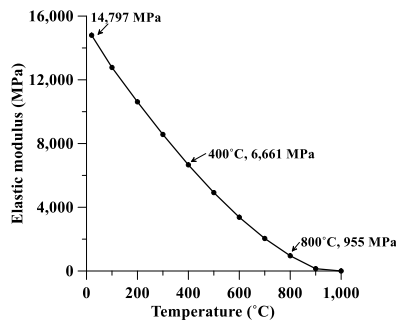
(a) Elastic modulus
(Bastami and Aslani, 2011)
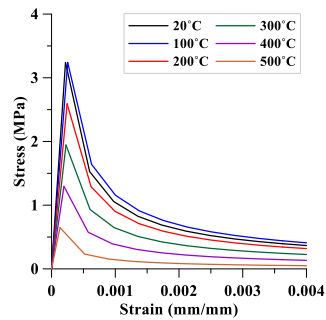
(b) Tensile stress-strain curves
(BS EN 1992-1-2, 2004)
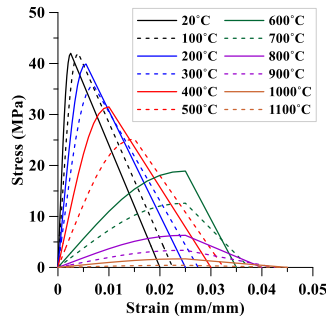
(c) Compressive stress-strain curves (BS EN 1992-1-2, 2004)

Figure 6-2 Mechanical properties of concrete at elevated temperature (PF-B2)

The thermal properties of concrete, which include density, conductivity, specific heat, and thermal expansion, were defined according to BS EN 1992-1-2 (2004) and ASCE Manual (1992). Each of the thermal properties at elevated temperature is shown in **Figure 6-3** at elevated temperature. The moisture content of concrete, which impacts its heat capacity, is implicitly considered by introducing a latent heat that occurs between 100 and 115°C when the specific heat reaches its maximum value. Due to the high moisture content of the specimen manufactured in this study, a material property definition of 3% moisture content was used in numerical analysis.

(a) Density
(BS EN 1992-1-2, 2004)

(b) Conductivity
(BS EN 1992-1-2, 2004)

(c) Specific heat
(BS EN 1992-1-2, 2004)

(d) Thermal expansion
(ASCE Manual, 1992)
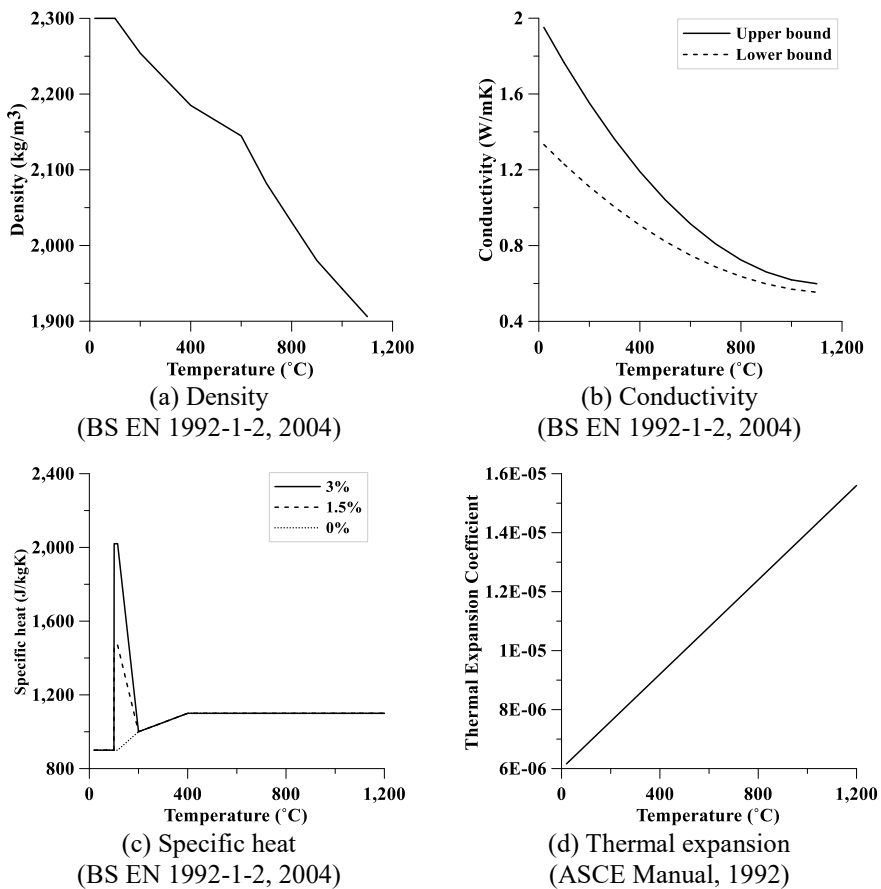
Figure 6-3 Thermal properties of concrete at elevated temperature

6.1.2 Steel modeling

The mechanical and thermal properties of reinforcing bar and tendon were defined according to BS EN 1992-1-2 (2004), BS EN 1993-1-2 (2005), and ASCE Manual (1992). Plasticity model was used to define the mechanical property of steel at elevated temperature. Elastic modulus, density, conduction, specific heat, and thermal expansion were also defined for heat transfer and thermo-mechanical analyses. **Figure 6-4** shows the mechanical and thermal properties of steel at elevated temperature.
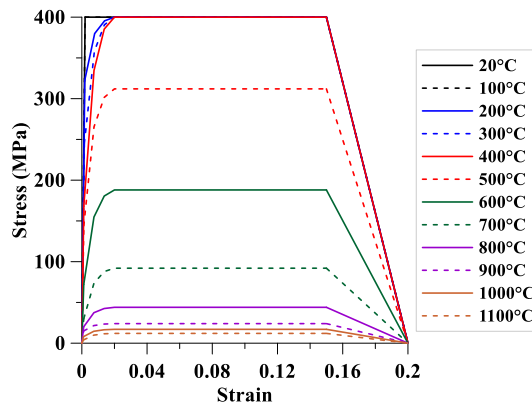
(a) Stress-strain curves of reinforcing bar (BS EN 1992-1-2, 2004)
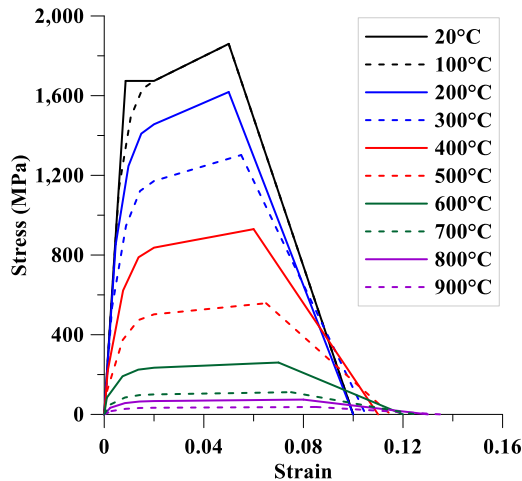
(b) Stress-strain curves of tendon (BS EN 1992-1-2, 2004)
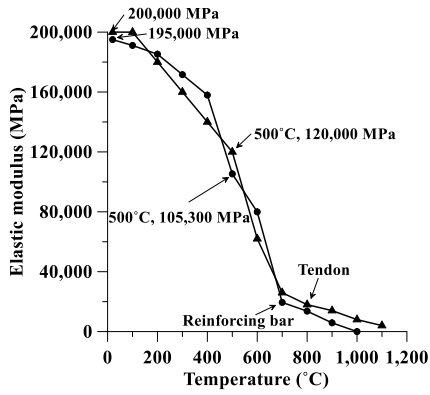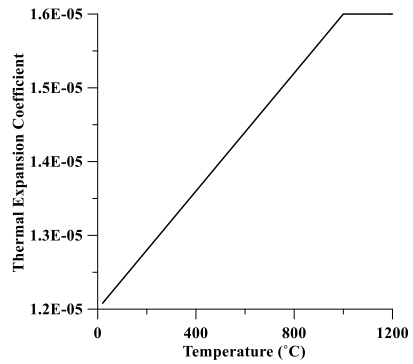
(c) Elastic modulus
(BS EN 1992-1-2, 2004)
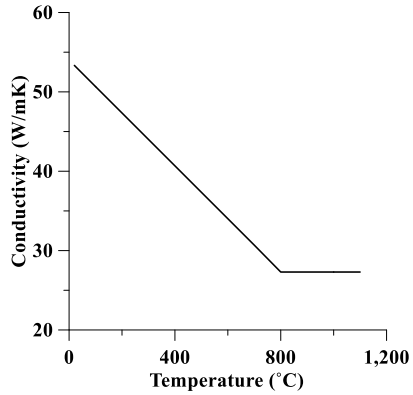
(d) Conductivity
(BS EN 1993-1-2, 2005)
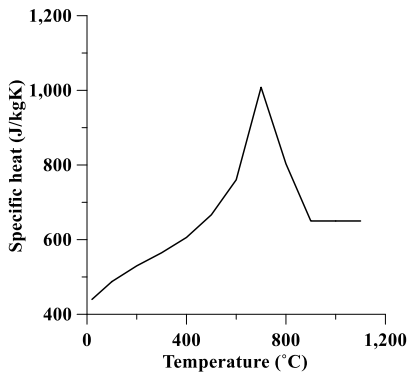
(e) Specific heat
(BS EN 1993-1-2, 2005)

(f) Thermal expansion
(ASCE Manual, 1992)

Figure 6-4 Mechanical and thermal properties of steel at elevated temperature

6.2 Heat transfer analysis

6.2.1 Heat transfer model

In heat transfer analysis, reinforcing bar and tendon were modeled with 2-node heat transfer link (DCID2), and concrete slab was modeled with 8-node linear heat transfer brick (DC3D8). To analyze the temperature field of PT concrete slab, three modes of heat transfer, namely convection, radiation, and conduction, were considered. Theoretical concepts are described in the Eurocode and previous studies (EN1991-1-2, 2002; Gao et al., 2013; Martinez and Jeffers, 2021), and the following contents are the summaries for each mode.

Conduction is a concept of heat transfer that occurs within the structure's body. By Fourier's differential equation (Purkiss and Li, 2014), the temperature gradient can be described in a time-dependent equation as shown in **Eq. (6-1)**.

$$\frac{\partial}{\partial x}(k_c \frac{\partial T}{\partial x}) + \frac{\partial}{\partial y}(k_c \frac{\partial T}{\partial y}) + \frac{\partial}{\partial z}(k_c \frac{\partial T}{\partial z}) + Q = \rho_c c_c \frac{\partial T}{\partial t} \qquad (6\text{-}1)$$

Where, c_c is specific heat capacity; k_c is conductivity; Q is inherently generated heat; t is time variable; and ρ_c is density. For heat transfer analysis, inherently generated heat (Q) can be neglected ($Q = 0$).

Convection and radiation are a concept of heat transfer that occurs with the surface of structure and surrounding conditions. It can be depicted by means of the Robin boundary condition (Purkiss and Li, 2014) as shown in **Eq. (6-2)**.

$$-k_c \frac{\partial T}{\partial n} = h_c(T - T_f) + \sigma \varepsilon_m \varepsilon_f [(T - T_z)^4 - (T_f - T_z)^4] \qquad (6\text{-}2)$$

Where, n is outward normal direction of member surface; h_c is convective heat transfer coefficient; T_f is fire temperature measured in furnace; T_z is absolute zero temperature; σ is Stefan-Boltzmann constant; ε_m is heat emissivity of exposed surface; and ε_f is heat emissivity of fire. According to EN 1991-1-2 (2004), the value of h_c is 25 W/(m²K) at fire-exposed surface and 9 W/(m²K) at ambient exposed surface; σ is 5.67×10^{-8} W/(m²K⁴); ε_f is 1.0; and ε_m is 0.8 for concrete.

6.2.2 Heat transfer analysis

Heat transfer analysis was performed on the PF-B2 and PF-B3 cases. At the bottom of each numerical model, the furnace temperature (**Figure 5-1**) was applied as a heating load. **Figure 6-5** shows the time-temperature curves of furnace, fire test result, and FEA results. To check mesh convergence, the models were meshed differently. As shown in **Figure 6-5**, the mesh interval along the height direction had an effect on convergence but width mesh did not affect convergence for heat transfer analysis. In both PF-B2 and PF-B3, when the mesh interval narrowed, the FEA accuracy increased but the analysis time increased. It was determined that meshing at a height of 50 mm for PF-B2 and 70 mm for PF-B3 is suitable. The time-temperature curves for concrete at the tendon location are shown in **Figure 6-6**. In PF-B2, the FEA and fire test results matched well across all mesh types, but in PF-B3, the fire test result showed irregular fluctuation that made comparison difficult. However, because the bottom time-temperature curves and PF-B2 case matched well, it is possible to estimate that the FEA result may be utilized to analyze the temperature of the concrete at the tendon location. **Figure 6-7** and **Figure 6-8** show the results of the heat transfer analysis in the section view at the middle of the model. Although the FEA was performed in three-dimensional, heat transfer occurred mostly in height direction due to the heating load being delivered uniformly over the width direction. Additionally, heat was transferred up to the height of 75 mm in the PF-B2 case and 110 mm in the PF-B3 case.
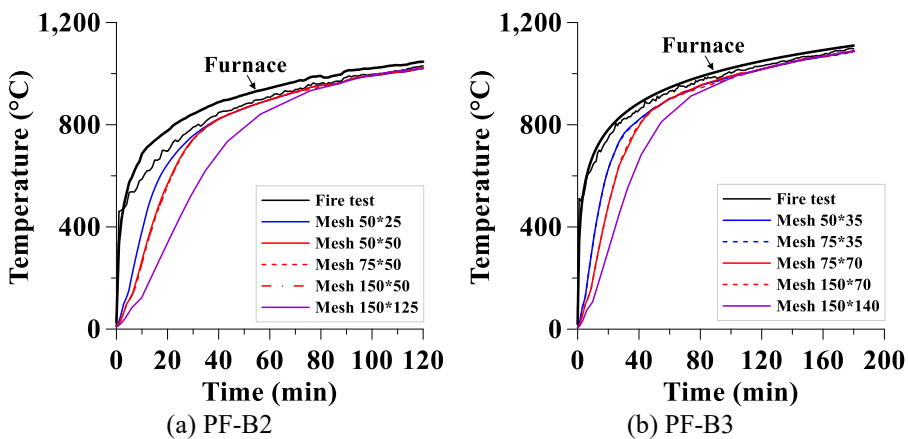

(a) PF-B2   (b) PF-B3

Figure 6-5 FEA time-temperature curves for bottom of the slab
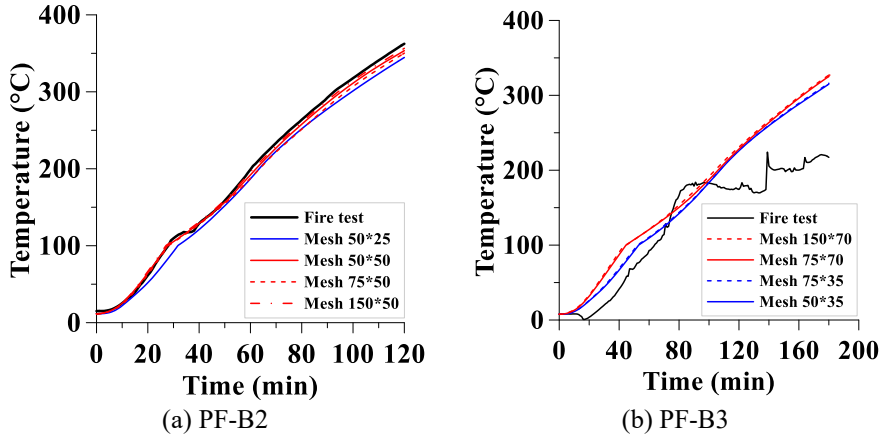
(a) PF-B2   (b) PF-B3

Figure 6-6 FEA time-temperature curves for concrete at tendon location

(a) Mesh size (50 × 25)

(b) Mesh size (50 × 50)

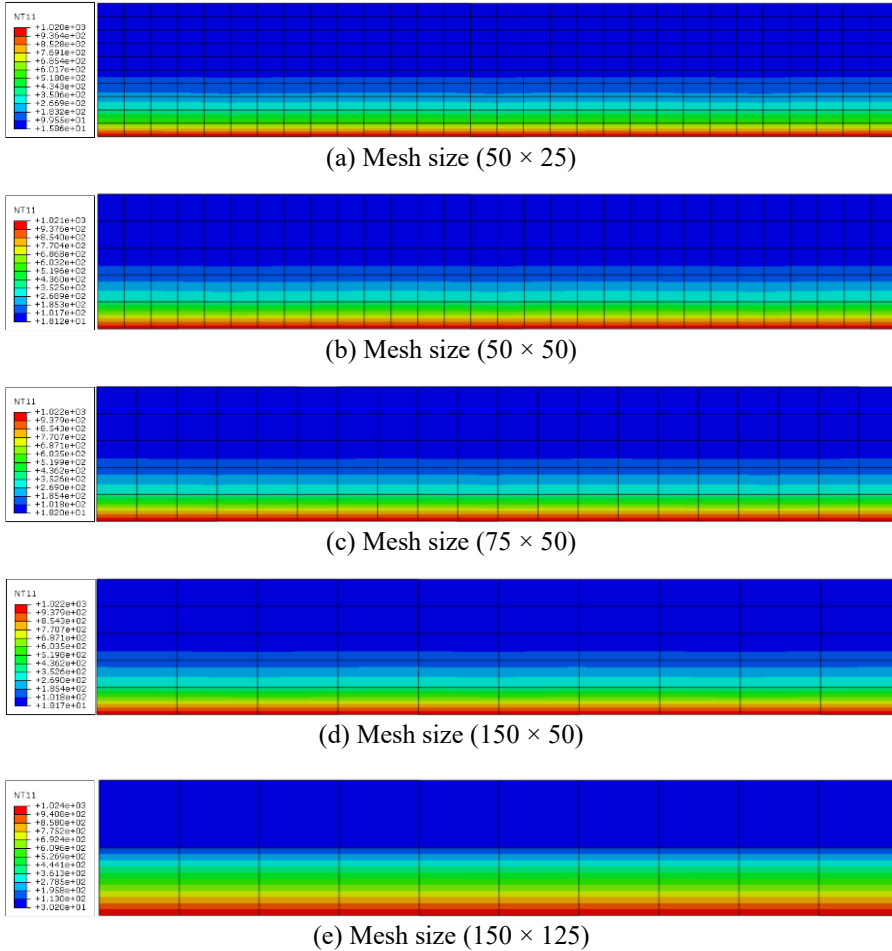(c) Mesh size (75 × 50)
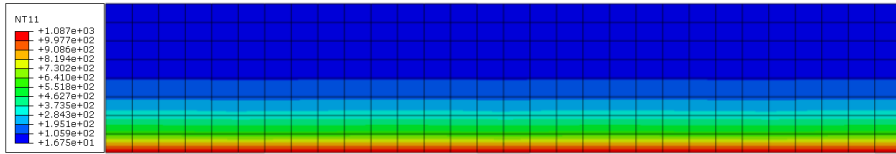

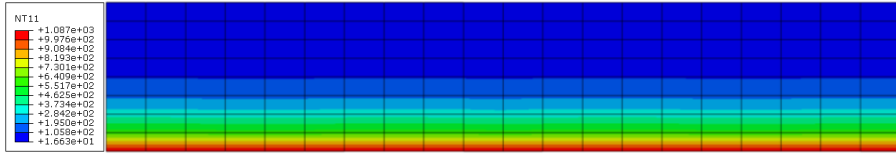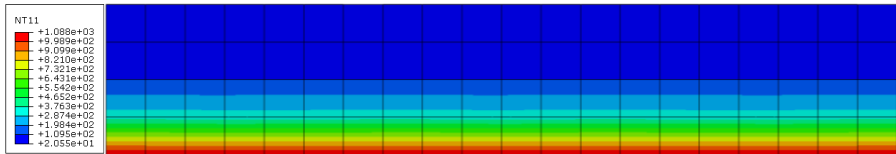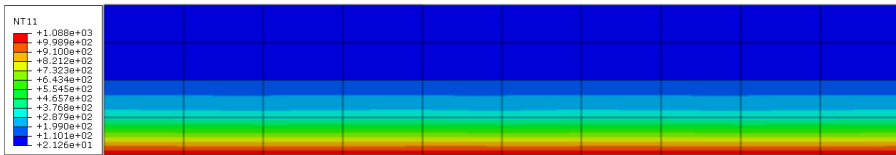(d) Mesh size (150 × 50)

(e) Mesh size (150 × 125)

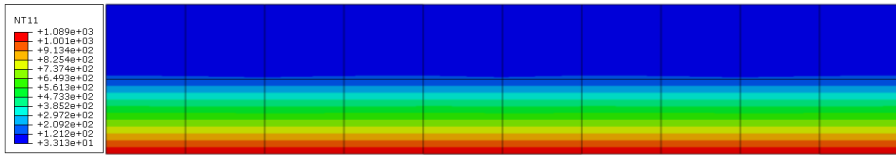**Figure 6-7** Results of heat transfer analysis (PF-B2)

(a) Mesh size (50 × 35)

(b) Mesh size (75 × 35)

(c) Mesh size (75 × 70)

(d) Mesh size (150 × 70)

(e) Mesh size (150 × 140)

Figure 6-8 Results of heat transfer analysis (PF-B3)

6.3 Thermo-mechanical analysis

6.3.1 Thermo-mechanical model

Thermo-mechanical analysis was performed by using coupled temperature-displacement mechanism which analyzes temperature and stress or displacement field together. The same heat transfer mechanism used in Section 6.2 was applied to thermo-mechanical analysis but with different element types. Stress elements were replaced for coupled temperature-displacement model, which are 2-node 3-D thermally coupled truss (T3D2T) for tendon and reinforcing bar and 8-node thermally coupled brick (C3D8T) for concrete.

The mesh plan for thermo-mechanical analysis was determined by taking mesh convergence and analysis time into account. Models were meshed in a cube or cuboid shape, which is believed to be the ideal shape for stress analysis. Mesh sizes were designed to be $150 \times 150 \times 50$ and $75 \times 75 \times 50$ for PF-B2, and $150 \times 150 \times 70$ and $75 \times 75 \times 70$ for PF-B3. **Figure 6-9** shows that meshed model of PF-B3 ($75 \times 75 \times 70$) in top, front, and side views.
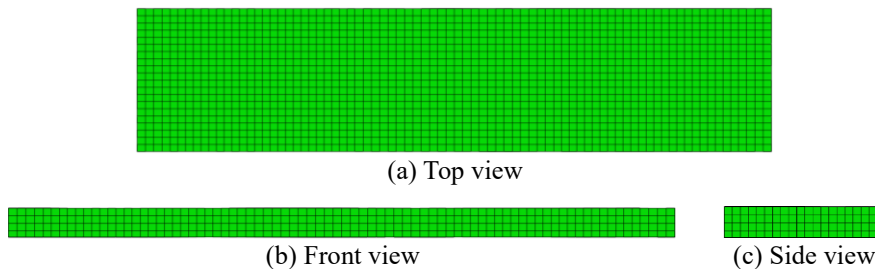
(a) Top view

(b) Front view   (c) Side view

Figure 6-9 Meshed model for thermo-mechanical analysis

The following steps were performed to successfully conduct the thermo-mechanical analysis: (1) prestressing, (2) loading, and (3) heating. The mechanical properties of concrete were modeled using a damaged plasticity constitutive model, as shown in Section 6.1.1. The properties of steel were modeled using a plasticity model, as shown in Section 6.1.2. Both material properties were defined in dependence on the temperature field, which is specified in EN 1992-1-2 (2004) and Bastami and Aslani (2011).

6.3.2 Thermo-mechanical analysis: prestressing

Prestressing was applied to tendon in the analysis by using the pre-defined field where the effective prestress load is $0.65 f_{pu}$ ($= 1116$ MPa). Boundary conditions were defined to be pinned at both end surfaces only accepting x-direction displacement. **Figure 6-10** shows the details of model at prestressing step.

As shown in **Figure 6-10 (a)**, prestress was applied on tendon in the value of 1116 MPa. The effect of prestressing on concrete at anchor zone can be seen in **Figure 6-10 (b)**. After prestressing analysis was performed, the boundary conditions set at the prestressing step were released, and simply-supported condition was newly adapted for the next steps with prestressing load remained until the end of the FEA.
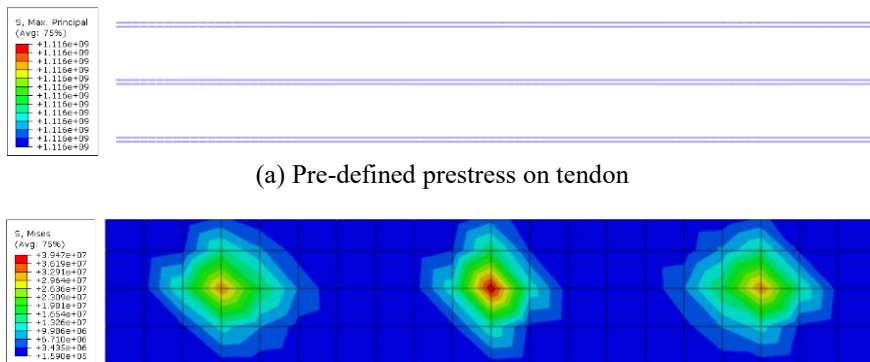

(a) Pre-defined prestress on tendon

(b) Effect of prestressing on concrete at anchor zone

Figure 6-10 Details of model at prestressing step

6.3.3 Thermo-mechanical analysis: loading

Following the prestressing step, the loading step was performed. A four-point actuator was used to apply a vertical force of 30 kN to each leg during the fire tests. In FEA, the loading location and force were replicated by partitioning the model and applying nodal force to the designated location. **Figure 6-11** shows the details of model at loading step.

Figure 6-12 shows the result of FEA from the prestressing to loading step. Camber occurred in PF-B2 and PF-B3 at the prestressing step with values of 7.8 and 5.5 mm, respectively. After applying four-point loads, deflection occurred at 15.5 and 10.9 mm in PF-B2 and PF-B3, respectively, which are consistent with the fire test results of 16.2 and 12.1 mm. After applying loads, the tendon stress increased from 1,116 MPa, and the stress distribution of concrete is shown in **Figure 6-12 (d)**.
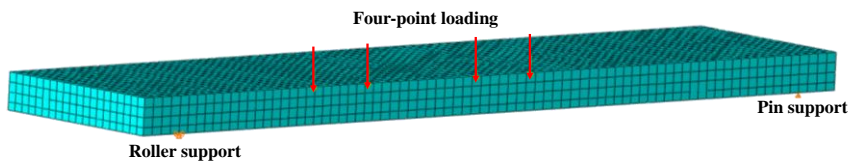
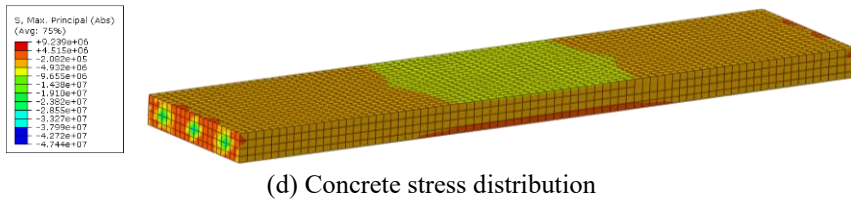**Figure 6-11** Details of model at loading step

(a) Step-deflection curve (PF-B2)   (b) Step-deflection curve (PF-B3)

(c) Tendon stress distribution
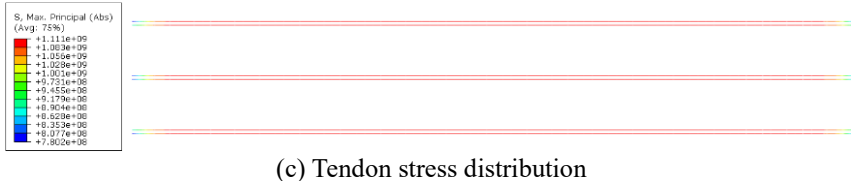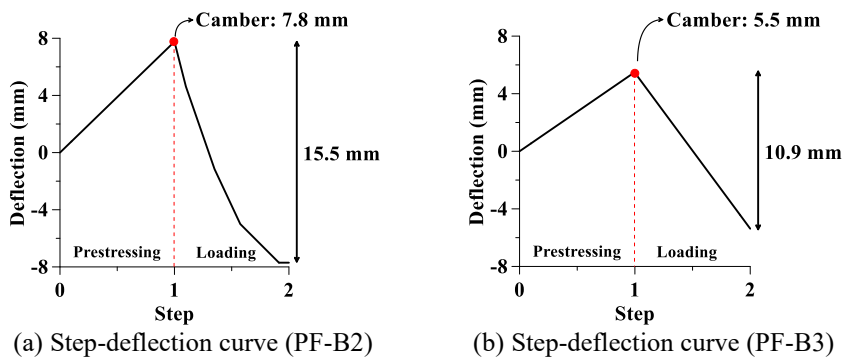
(d) Concrete stress distribution

Figure 6-12 Results of FEA from prestressing to loading step

6.3.4 Thermo-mechanical analysis: heating

Heating step was performed after conducting prestressing and loading steps. Section 6.2 examined the mechanisms of heat transfer and the temperature of the bottom surface which is equally applied in this section. Additionally, thermo-mechanical mechanism is examined in this section in terms of deflection and stress variations.

Mesh sizes of $150 \times 150 \times 50$ and $75 \times 75 \times 50$ for PF-B2 and $150 \times 150 \times 70$ and $75 \times 75 \times 70$ for PF-B3 both functioned well during the prestressing and loading process; however, $75 \times 75 \times 50$ for PF-B2 did not work during the heating step. Thus, the results of FEA are studied with mesh size of $150 \times 150 \times 50$ for PF-B2 and $75 \times 75 \times 70$ for PF-B3.

Figure 6-13 shows the time-deflection and time-deflection rate curves of PF-B2 and PF-B3 during fire tests and FEA. Except for the brief period during which an unexpected disturbance occurred, the results of fire tests and FEA matched well. Based on the fact that both the results of the heat transfer analysis (Section 6.2) and thermo-mechanical analysis (Section 6.3) both matched well with the results of the fire tests, it can produce additional data that the fire test could not obtain can be assumed via FEA, and further parametric study using the same material properties and modeling methods can be conducted.
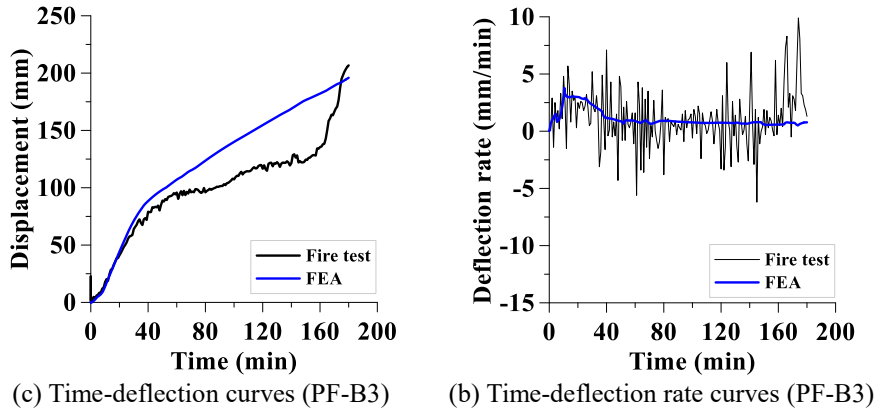

(a) Time-deflection curves (PF-B2)　　(b) Time-deflection rate curves (PF-B2)

(c) Time-deflection curves (PF-B3)   (b) Time-deflection rate curves (PF-B3)
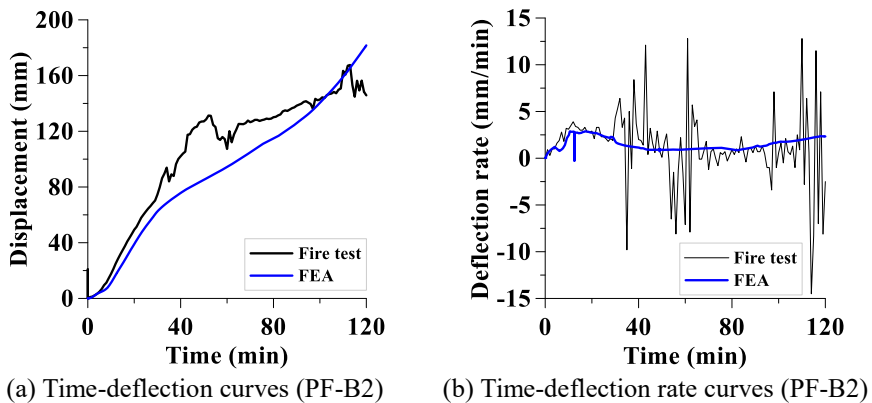
Figure 6-13 FEA and fire test results

Figure 6-14 shows the results of stress variation by FEA of PF-B2 at the center and support regions. The stress values at the top and bottom of the slab were compared to the compressive and tensile strengths of concrete specified by EN 1992-1-2 (2004) and Aslani and Bastami (2011) at elevated temperature.

Early concrete spalling was predicted to occur at the center and support regions for about 25 and 20 minutes after the heating started, respectively, when the concrete tensile strength becomes less than the applied bottom stress.

For about 30 minutes after the heating started, crack propagation was predicted to occur exclusively at the center region, when the concrete compressive strength becomes less than the applied top stress. The crack propagation tendency is consistent with the fire test result given in **Figure 5-12 (a)**, which shows that no cracks propagated at the support but only in the center region. **Figure 6-15** and **Figure 6-16** show the stress variation over time in the section view at the center and support regions, respectively, for PF-B2.
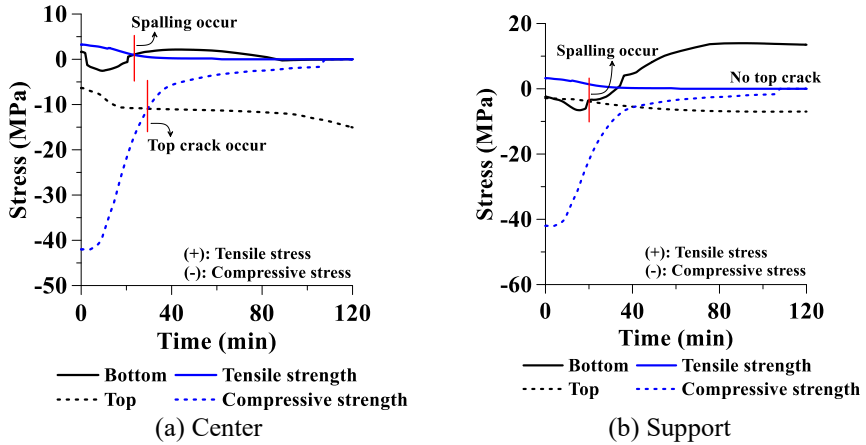
(a) Center   (b) Support

Figure 6-14 Results of stress variation by FEA (PF-B2)

(a) Initial

(b) After 30 minutes

(c) After 60 minutes
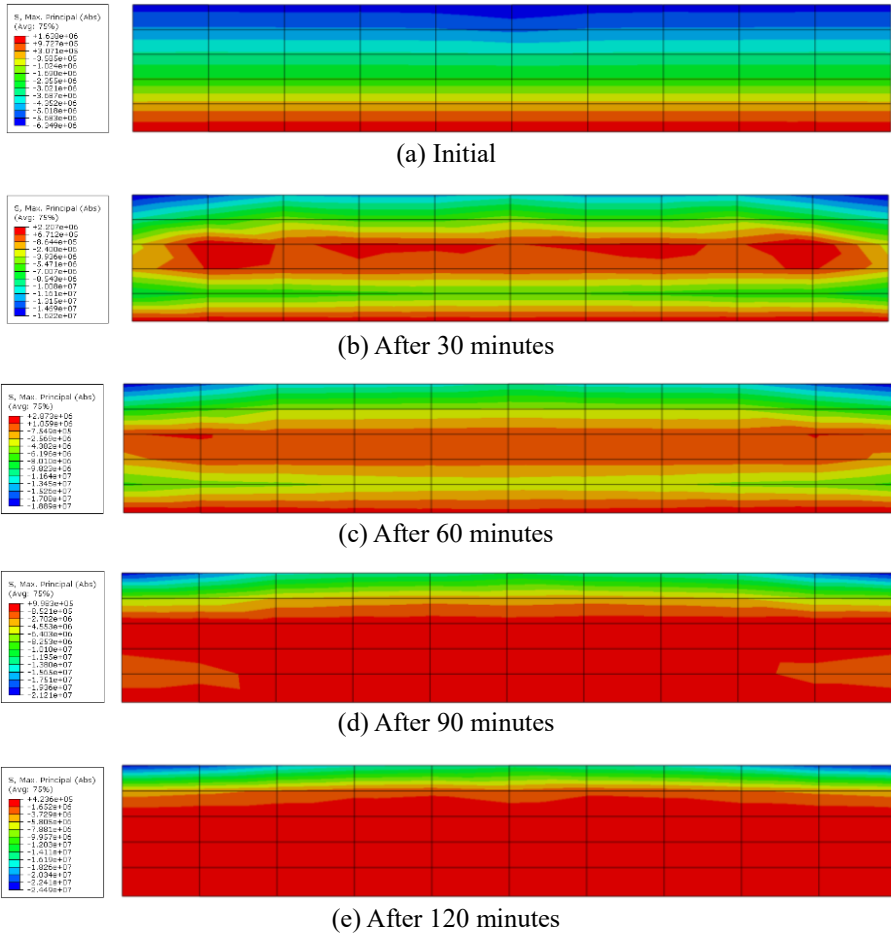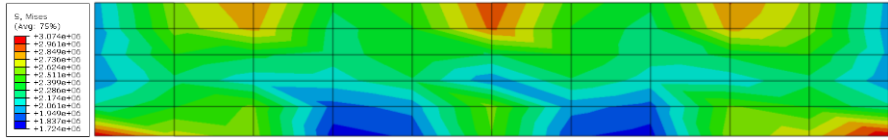

(d) After 90 minutes

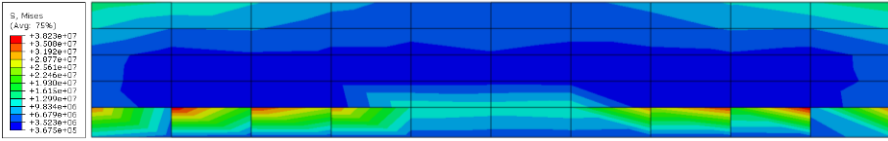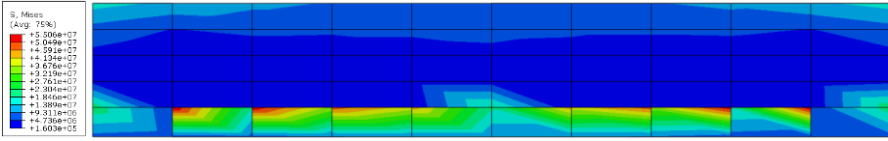
(e) After 120 minutes

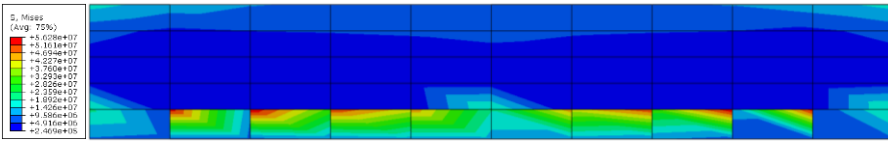**Figure 6-15** Stress variation by time at the center (PF-B2)

(a) Initial
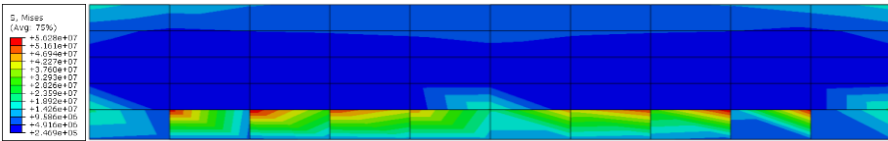

(b) After 30 minutes

(c) After 60 minutes

(d) After 90 minutes

(e) After 120 minutes

Figure 6-16 Stress variation by time at the support (PF-B2)

Figure 6-17 shows the results of stress variation by FEA of PF-B3 at center and support locations. As with the PF-B2 example, early concrete spalling was predicted to occur at the center and support for about 20 minutes after heating started. However, spalling did not occur at the center in either PF-B2 or PF-B3, and only the PF-B3 case showed spalling near the anchor region. This could be because of the presence of reinforcing bars, which add extra tensile strength to the concrete. Also, as seen by the time-stress graphs, the support zone is subjected to greater tensile stress at the bottom than the central region. This can account for the regional spalling of PF-B3 near the anchor zone, as reinforcing bars provide additional tensile strength, but excessive tensile stress cannot be endured, resulting in spalling.

In PF-B3, top crack is predicted at both center and support regions. This is also shown in fire test (**Figure 5-12 (b)**) with center region suffering more severe crack propagation. **Figure 6-18** and **Figure 6-19** show the stress variation over time in the section view at the center and support regions, respectively, for PF-B3.
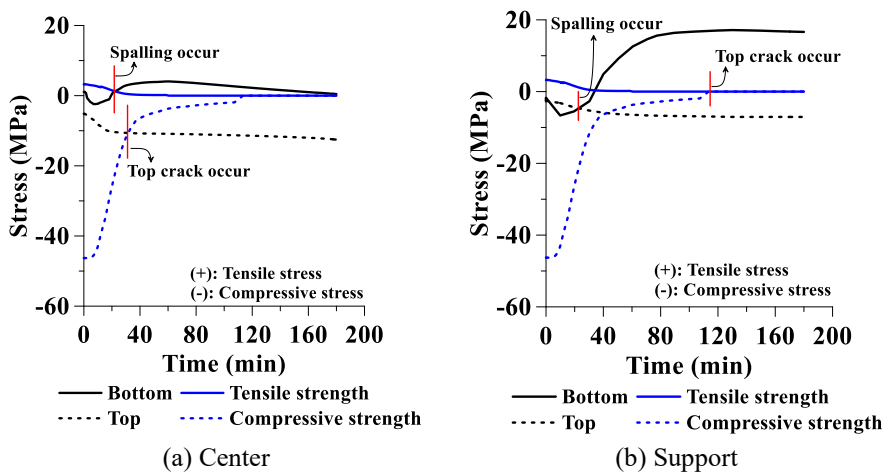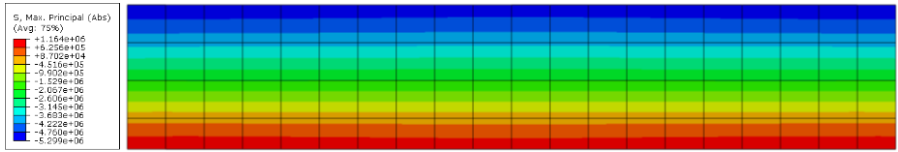

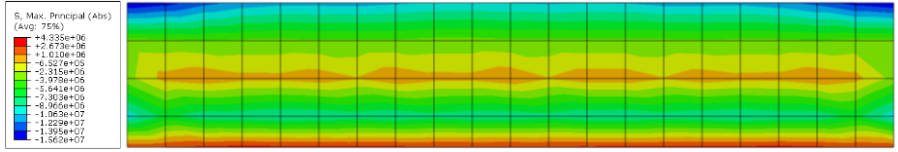(a) Center   (b) Support

Figure 6-17 Results of stress variation by FEA (PF-B3)

(a) Initial

(b) After 30 minutes
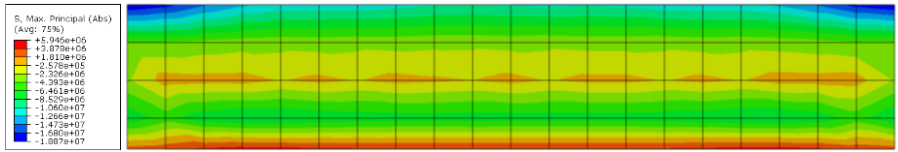
(c) After 60 minutes

(d) After 90 minutes

(e) After 120 minutes

(f) After 150 minutes

(g) After 180 minutes

Figure 6-18 Stress variation by time at the center (PF-B3)
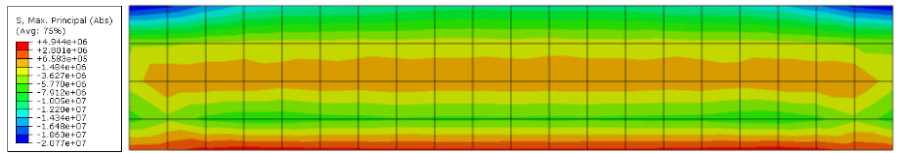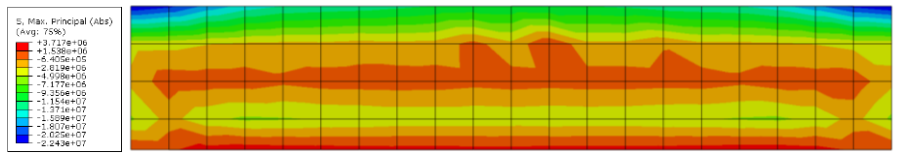
(a) Initial

(b) After 30 minutes
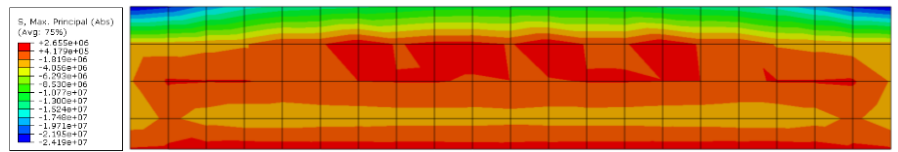

(c) After 60 minutes

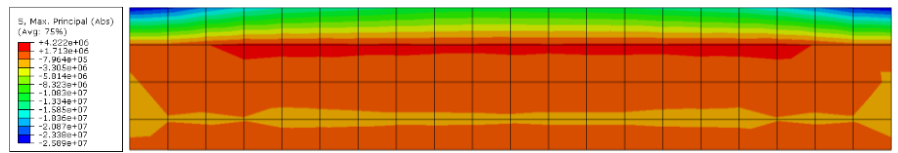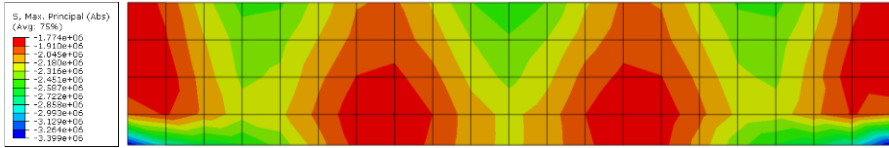(d) After 90 minutes

(e) After 120 minutes

(f) After 150 minutes
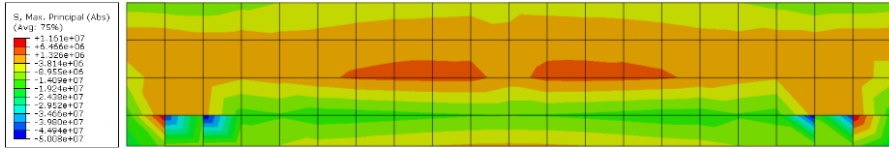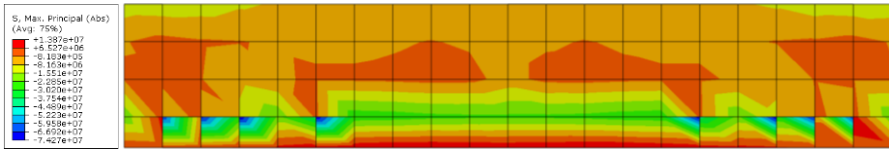

(g) After 180 minutes

Figure 6-19 Stress variation by time at the support (PF-B3)
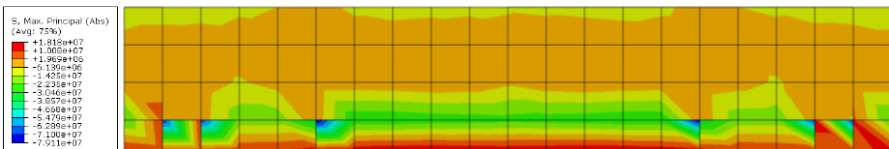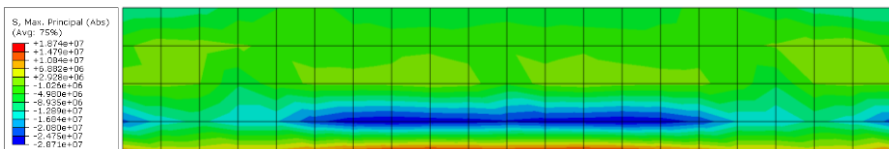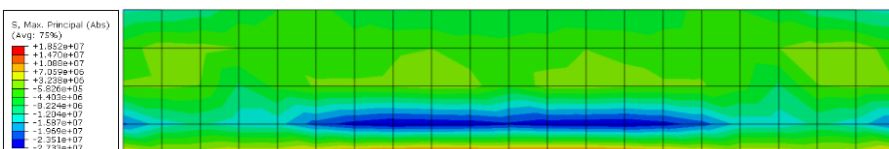
6.4 Parametric study

Table 6-2 shows the variables of parametric study in numerical modeling. Parametric study was performed using FEA under the same conditions as the fire tests, but by adjusting cover thicknesses with values of 45 mm (FEA-45), 60 mm (FEA-60), and 70 mm (FEA-70). The values of 45 and 60 mm are the specified cover thicknesses in IBC 2018 (ICC, 2017) for two-hour and three-hour fire resistance ratings, respectively, with unrestrained conditions (**Table 1-2**). Eurocode 2 (EN1992-1-2, 2004) specifies a cover thickness of 70 mm. The input fire scenario followed the ISO 834 standard fire curve (**Eq. (5-1)**; ISO, 1999) with a target fire resistance time of four hours. Fire performance of models was determined by comparing their deflections and deflection rates. The numerical model and material properties were defined in accordance with Section 6.1 to Section 6.3.

Table 6-2 Variables of parametric study in numerical modeling

Numerical model	FEA-45	FEA-60	FEA-70
Analysis time (min)	240		
Dimensions (mm)	6700 × 1500 × 250	6700 × 1500 × 280	6700 × 1500 × 300
Cover thickness (mm)	45	60	70
Tendon number	6	6	6
Initial tendon tensile stress (MPa)	1,116	1,116	1,116
Tendon type	Bonded bare-strand tendon		
Input fire scenario	ISO 834 standard fire curve		
Boundary condition	Unrestrained		

Table 6-3 Summary of results of parametric study

Numerical model	FEA-45	FEA-60	FEA-70
Analysis duration (min)	184	240	240
End temperature of tendon (°C)	440	428	379
Deflection (mm)	492.8* (at 180 min)	287.8	186.9

* When the deflection of numerical model exceeds the acceptance specified in ASTM E119.

Table 6-4 Tendon temperature variations of each numerical model

Model \ Time	60 min	120 min	180 min
FEA-45	176°C	339°C	434°C
FEA-60	130°C	264°C	359°C
FEA-70	111°C	225°C	311°C

Table 6-3 shows the summary of results of parametric study and **Figure 6-20** shows the FEA results of parametric study in graphs. The increase rate of temperature at the tendon differed, depending on the cover thickness. **Table 6-4** summarizes the tendon temperature variations of each numerical model in an hour interval. As shown in **Figures 6-20 (b)**, **(c)**, and **(d)**, although the deflection and deflection rate over time at the initial stage was quite small, the accumulated effect of heat gradient was shown after passing 60 minutes of heating and became more significant after 90 minutes of heating. By assuming the structure failure when deflection or deflection rate exceeds acceptance limit specified in ASTM E119 (ASTM, 2020), FEA-45 experienced sudden increase of deflection after 150 minutes of heating, resulting in structural collapse after 180 minutes of heating. Since FEA-45 case was designed in reference to two-hour fire resistance capacity, it could be estimated that the current code well specifies with 30 minutes of safe capacity. Contrary to FEA-45, FEA-60 and FEA-70 showed stable increase in deflection over four hours of heating. FEA-60 and FEA-70 cases show that the current code (IBC 2018 and Eurocode) specifies sufficient cover thickness to satisfy the target fire resistance ratings. The numerical analysis results indicate that the numerical model used in the current FEA is applicable to simple evaluation of fire performance of PT concrete slabs with a variety of dimensions and loading conditions.
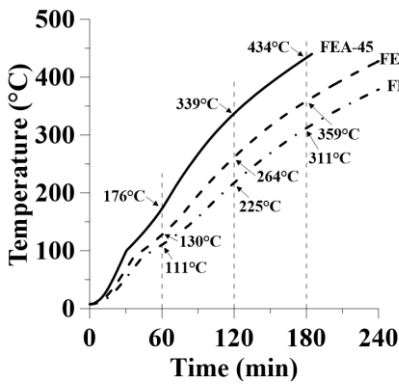
(a) Time-temperature curves
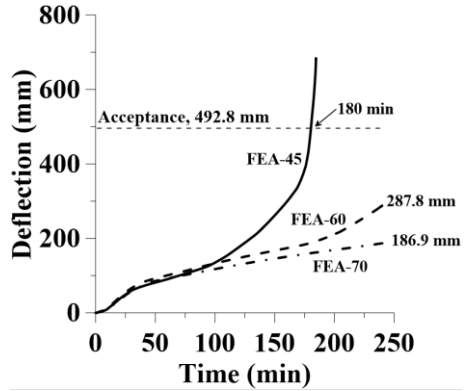
(b) Time-deflection curves
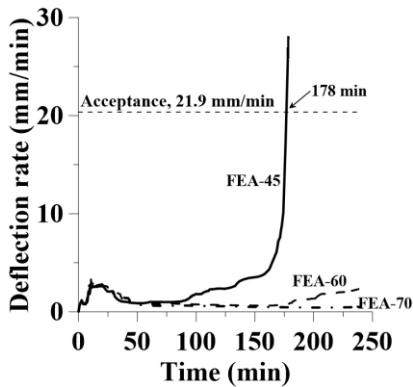
(c) Time-deflection rate curves

(d) Temperature-deflection curves

Figure 6-20 Results of FEA for parametric study
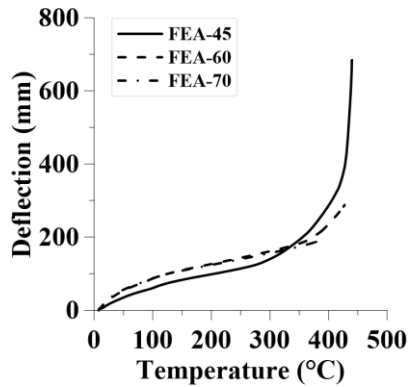
6.5 Discussion

In this chapter, numerical modeling and FEA were introduced. Summaries and discussions are as follows:

1) FEA was performed on the bonded PT cases using the ABAQUS program. Heat transfer and thermo-mechanical (heat stress) analyses were performed to verify the fire test results. Additionally, a parametric study was conducted by modifying the cover thickness.

2) Heat transfer analysis was performed using the concepts of conduction, convection, and radiation in accordance with Eurocode and previous research. The mesh size was varied and analysis results were compared to the results of fire tests. For heat transfer analysis, a mesh size of 50 mm intervals in the height direction was chosen. Although the bottom temperature of concrete was different in the initial phase compared to the fire test result, the temperature of concrete at the tendon level was comparable.

3) Thermo-mechanical (heat stress) analysis was performed using the same numerical model as was used in the heat transfer analysis. A model of damaged plasticity for concrete and a model of plasticity for steel were defined to conduct stress analysis. The processes of prestressing, loading, and heating were performed sequentially, which are the same as in those used for the experiment. The analysis results were consistent with the results of the fire tests.

4) Fire performance of the specimens were demonstrated by FEA using currently available methodologies. Further, the fire condition, structural dimension, loading condition, and material condition can be easily modified. The development of numerical models is expected to resolve issues such as various experimental site conditions and high cost.

Chapter 7. Conclusion

In this study, fire performance and behavior of two bonded and six unbonded PT one-way slabs were experimentally evaluated. Additionally, numerical analysis was performed only on bonded cases. Fire tests were conducted under sustained four-point static loading of 120 kN and monotonically increasing heating (ISO 834). The testing conditions were set by following the standards of ASTM E119 and KS F 2257. The specimen dimensions were designed to satisfy the ACI 318-19, IBC 2018, and ACI 423.10R-16. A general-purpose finite element analysis program (ABAQUS) was used to perform the numerical analysis. Heat transfer and thermo-mechanical analyses were performed sequentially, followed by parametric study. The following conclusions were drawn based on the results:

1) Temperature variations of slabs were measured at the locations of bottom, tendon, and reinforcing bar during fire tests. Except for the PF-B2 case, extreme temperature fluctuations were observed at the bottom of the slab between 14 and 24 minutes after the fire test began, which was attributed to the influence of early concrete spalling.

2) The presence of duct, the presence of grease, and the degree of evaporation of water all affected the temperature variation of the tendon. The duct delayed the penetration of heat into the tendon, as seen in the PF-S2 and PF-S3 cases. The delayed duration of heat penetration was 15 to 20 minutes. An earlier temperature increase, in the PF-S2 case, caused a shorter fire resistance time of 76% compared to PF-G2 or 55% compared to PF-U2. When grease was enclosed within the duct, the rate of temperature increase changed at 70ºC, the temperature at which grease is supposed to liquefy. The rate of temperature increase stabilized after reaching 100ºC due to evaporation of water in concrete.

3) Cover thickness affected the performance with different degrees for different tendon configuration in unbonded cases. The durations at failure with a cover thickness of 45 mm were 75, 55, and 42 min in PF-U2, PF-G2, and PF-S2, respectively. However, when the cover thickness was increased to 60 mm, the durations at failure were 52, 75, and 91 min in PF-U3, PF-G3, and PF-S3, respectively. The fire endurance duration of the PF-U3 decreased to 67% of PF-U2, whereas PF-G3 and PF-S3 increased to 36 and 116% of PF-G2 and PF-S2, respectively.

4) The time-deflection curve for each slab turned out to be equivalent regardless of the configuration of tendon prior to concrete delamination. After the fire test was completed, bonded cases retained load-resisting structural capacity, whereas unbonded cases failed prematurely. A sudden increase in deflection was noted, which was attributed to increased tendon temperature, concrete stiffness degradation, and section area loss.

5) The tensile force of the tendon was measured for unbonded cases. During heating, three stages of variation were discovered. The initial stage was tensile force-increasing stage caused by slab deflection and tendon elongation. Following the initial stage, the material's strength and stiffness degraded, resulting in a decrease in tensile force. Throughout the two stages, tendon tensile force variation was in the range of 10 to 20 kN, similar regardless of tendon configuration. The last stage was the rupture stage, during which the tensile force abruptly changed as a result of the structure failure.

6) Material stiffness degradation and loading conditions increased slab deflection, resulting in an increase in tendon tensile force. Also, because of the presence of tendons, large bursting force was applied downward near support (anchor) regions. Due to degraded material strength and stiffness, concrete near the anchor zone delaminated along the tendon. This behavior resulted in the early failure of unbonded cases. No stirrups were provided; if provided, delamination of concrete might have been prevented.

7) Heat transfer and thermo-mechanical analyses were performed by referring to previous studies. Mesh convergence was accomplished in the heat transfer analysis by varying the mesh size. Thermo-mechanical analysis was performed by employing a coupled temperature-displacement mechanism that performs stress analysis in conjunction with the application of temperature data. Numerical analysis was used to obtain temperature, deflection, deflection rate, and stress data. Crack propagation and spalling were predicted using a section view analysis of stress data.

8) To overcome the limitation of the testing facility and high cost of experiments, numerical analysis was used to define the specimen model, material properties, and analysis procedure. The method was validated by comparing with test results. After confirming a well-matched model, parametric study was conducted by modifying cover thickness. The analysis reproduced the performance and behavior of the structure and generated useful additional data.

9) The current fire testing conditions were more severe than specified by ASTM E119 and ISO 834. In an actual structure, such as a continuous slab or beam, the tendon's length will lengthen, alleviating the increase in tendon tensile force. Additionally, except for the end face of the structure, the tendon will be located in upper sections on supports that are less vulnerable to fire. Structure redundancy and stress redistribution would also strengthen the structure's safety, particularly for one- and two-way slabs.

In conclusion, bonded cases showed a sufficient fire resistance in accordance with the current specified codes and standards. Fire tests on unbonded cases were prematurely terminated due to unexpected concrete delamination, necessitating extra stirrups and/or long tendons. However, additional research is necessary to prove the need for reinforcement in a real-scale structure. Presence of HDPE sheathing, presence of duct and tendon configuration also had an effect on fire performance, especially during the early rapid temperature increase phase. Parametric studies are expected to aid further studies on the effect of a variety of dimensions and conditions fire performance of PT structures.

References

1.   AASHTO (2017), "AASHTO LRFD Bridge Design Specifications, 8rd Ed.," American Association of State Highway Transportation Officials, Washington D.C.

2.   ABAQUS (2014), "ABAQUS Standard User's Manual," SIMULIA, Johnston, RI.

3.   ACI Committee 318 (2019), "Building Code Requirements for Structural Concrete and Commentary," American Concrete Institute, Farminton Hills, MI.

4.   ACI 423.7-14 (2014), "Specification for Unbonded Single-Strand Tendon Materials," American Concrete Institute, Farmington Hills, MI.

5.   ACI 423.10R-16 (2016), "Guide to Estimating Prstress Loss," American Concrete Institute, Farmington Hills, MI.

6.   ASCE (1992), "Structural Fire Protection," ASCE committee on fire protection, Manual No. 78, Reston, VA.

7.   Aslani, F. and Bastami, M. (2011), "Constitutive Relationships for Normal-and High-Strength Concrete at Elevated Temperatures," *ACI Materials Journal*, pp. 355-364.

8.   ASTM E119 (2020), "Standard Test Methods for Fire Tests of Building Construction and Materials," ASTM Committee on Standards, West Conshohocken, PA.

9.   Bailey, C. G. and Ellobody, E. (2009), "Fire Tests on Bonded Post-Tensioned Concrete Slabs," *Engineering Structures,* V. 31, pp. 686-696.

10.   Buchanan, A. H. and Abu, A. K. (2017), "Structural Design for Fire Safety 2nd Edition," John Wiley & Sons, Ltd, Chichester, UK.

11.   Burns, N. H., Charney, F. A., and Vines, W. R. (1978), "Tests of One-Way Post-Tensioned Slabs with Unbonded Tendons," *PCI Journal,* V. 23, pp. 66-83.

12.   Chang, Y. F., Chen, Y. H., Sheu, M. S., and Yao, G. C. (2006), "Residual Stress-Strain Relationship for Concrete after Exposure to High Temperatures," *Cement and Concrete Research,* V. 36, pp. 1999-2005.

13.   Choi, J., Woods, C. R., Hrynyk, T. D., and Bayrak, O. (2020), "Delamination Cracking Behavior of Curved Post-Tensioned Concrete Structures," *ACI Structural Journal*, pp. 169-183.

14.   Du, Y., Peng, J.-Z., Liew, J. Y. R., and Li, G.-q. (2018), "Mechanical Properties of High Tensile Steel Cables at Elevated Temperatures," *Construction and Building Materials,* V. 182, pp. 52-65.

15.   Dwaikat, M. B. and Kodur, V. K. R. (2009), "Fire Induced Spalling in High Strength Concrete Beams," *Fire Technology,* V. 46, pp. 251-274.

16.   Ellobody, E. and Bailey, C. G. (2008), "Behaviour of Unbonded Post-Tensioned One-Way Concrete Slabs," *Advances in Structural Engineering,* V. 11, No. 1, pp. 107-120.

17.   EN1991-1-2 (2002), "Eurocode 1: Actions on Structures - Part 1-2: General Actions - Actions on Structures Exposed to Fire," The European Union, Brussels.

18.   EN1992-1-2 (2004), "Eurocode 2: Design of Concrete Structures - Part 1-2: General Rules - Structural Fire Design," The European Union, Brussels.

19.   EN1993-1-2 (2005), "Eurocode 3: Design of Steel Structures - Part 1-2: General Rules - Structural Fire Design," The European Union, Brussels.

20.   Gao, W. Y., Dai, J.-G., Teng, J. G., and Chen, G. M. (2013), "Finite Element Modeling of Reinforced Concrete Beams Exposed to Fire," *Engineering Structures,* V. 52, pp. 488-501.

21.   Garcia, J. M., Bonett, R. L., Schultz, A. E., and Ledezma, C. (2017), "Stress at Ultimate in Unbonded Tendons for Ungrouted Post-Tensioned Masonry Beams," *Engineering Structures,* V. 140, pp. 447-457.

22.   Hou, X., Zheng, W., and Kodur, V. K. R. (2013), "Response of Unbonded Prestressed Concrete Continuous Slabs under Fire Exposure," *Engineering Structures,* V. 56, pp. 2139-2148.

23. ICC (2017), "2018 International Building Code," Country Club Hills, IL.

24. International Standard ISO 834-1-1999 (1999), "Fire-Resistance Tests-Elements of Building Construction-Part 1: General Requirement," ISO, Geneva, Switzerland.

25. Kang, T. H.-K. and Huang, Y. (2012), "Nonlinear Finite Element Analyses of Unbonded Post-Tensioned Slab-Column Connections," *PTI Journal*.

26. Kodur, V., Dwaikat, M., and Fike, R. (2010), "High-Temperature Properties of Steel for Fire Resistance Modeling of Structures," *Journal of Materials in Civil Engineering,* V. 22, No. 5, pp. 423-434.

27. Kodur, V. K. R. and Dwaikat, M. B. (2010), "Effect of Fire Induced Restraint on Fire Resistance of Reinforced Concrete Beams," *Structural Fire Engineering,* V. 1, No. 2, pp. 73-88.

28. Kodur, V. K. R., Wang, T. C., and Cheng, F. P. (2004), "Predicting the Fire Resistance Behaviour of High Strength Concrete Columns," *Cement & Concrete Composites,* V. 26, pp. 141-153.

29. KS F 2257-5 (2014), "Methods of Fire Resistance Test for Elements of Building Construction - Specific Requirements for Load Bearing Horizontal Separating Elements," Korean Agency for Technology and Standards.

30. Lee, G., Han, D., Han, M.-C., Han, C.-G., and Son, H.-J. (2012), "Combining Polypropylene and Nylon Fibers to Optimize Fiber Addition for Spalling Protection of High-Strength Concrete," *Construction and Building Materials,* V. 34, pp. 313-320.

31. Lie, T. T. and Lin, T. D. (1985), "Fire Performance of Reinforced Concrete Columns," STP 882, *Fire Safety: Science and Engineering*, ASTM International, West Conshohocken, PA, pp. 176-205.

32. Lin, T. Y. (1963), "Load-Balancing Method for Design and Analysis of Prestressed Concrete Structures," *In Journal Proceedings,* V. 60, No. 6, pp. 719-742.

33. Martinez, J. and Jeffers, A. E. (2021), "Analysis of Restrained Composite Beams Exposed to Fire," *Engineering Structures,* V. 234, 111740.

34. PTI (2006), "Post-Tensioning Manul, 6th Edition," Post-Tensioning Institute, Farmington Hills, MI.

35. Purkiss, J. A. and Li, L.-Y. (2014), "Fire Safety Engineering Design of Structures Third Edition," CRC Press, Boca Raton, FL.

36. Shin, H., Kang, T. H.-K., and Park, J.-H. (2020), "Grouted Extruded-Strand Tendons: Friction Coefficients and Differential Individual Strand Forces," *ACI Structural Journal*, pp. 223-233.

37. VSL (2015), "Vsl Strand Post-Tensioning Systems," VSL International Ltd., Köniz, Switzerland.

38. Yang, K.-H. and Kang, T. H.-K. (2011), "Equivalent Strain Distribution Factor for Unbonded Tendon Stress at Ultimate," *ACI Structural Journal,* V. 108, No. 2, pp. 217-226.

39. Yoon, I.-S., Shin, H., and Kang, T. H.-K. (2019), "Comparative Study on Performance of Corrosion Protective Systems for Post-Tensioned Concrete Members," *ACI Structural Journal*, pp. 273-284.
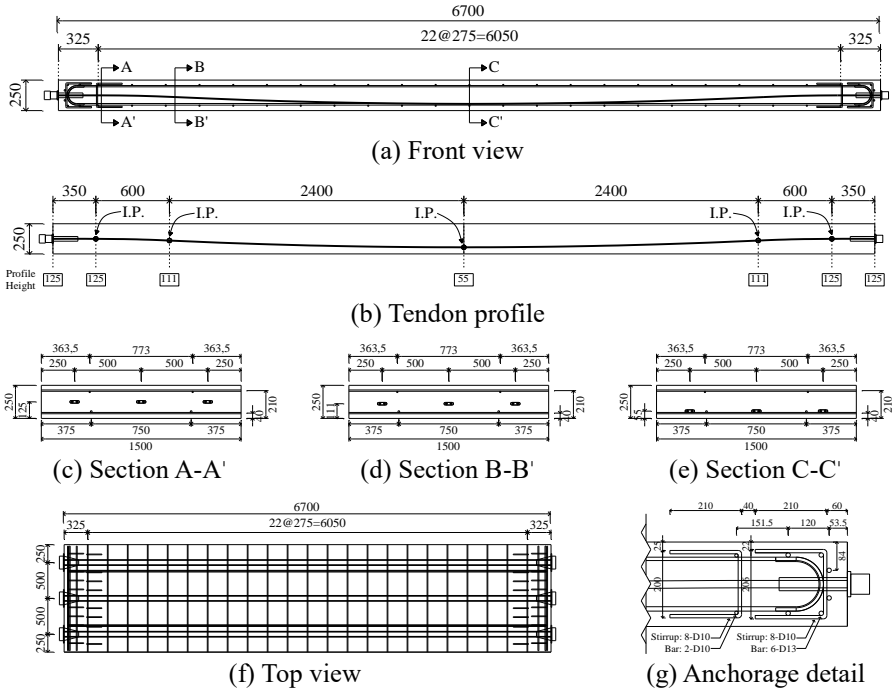
Appendix A : Final drawings

(a) Front view

(b) Tendon profile

(c) Section A-A' (d) Section B-B' (e) Section C-C'

(f) Top view (g) Anchorage detail

Figure A-1 Details of Specimen PF-B2 (unit: mm)

(a) Front view

(b) Tendon profile

(c) Section A-A' (d) Section B-B' (e) Section C-C'

(f) Top view (g) Anchorage detail
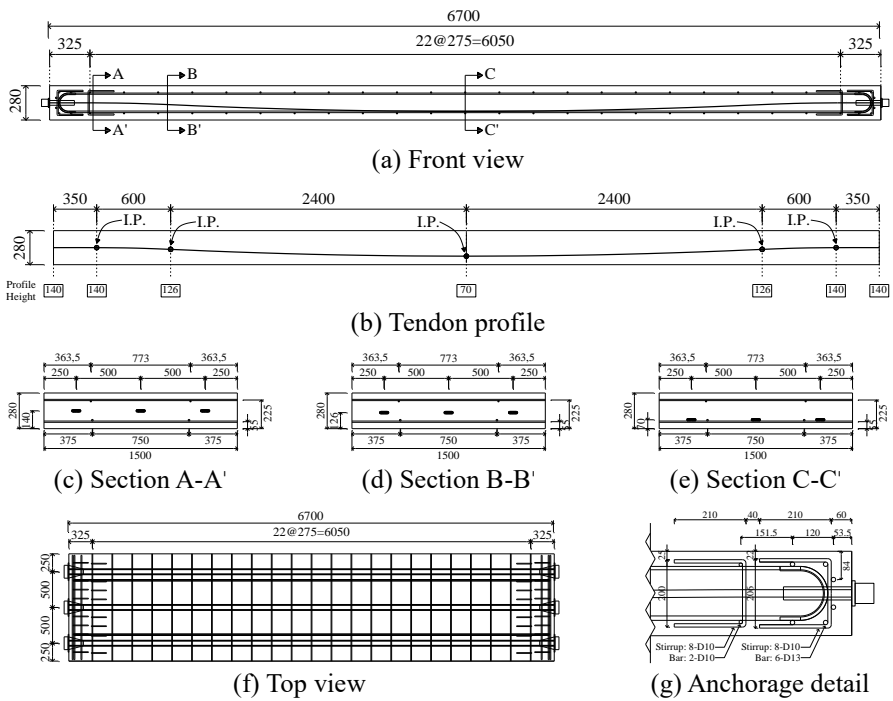
Figure A-2 Details of Specimen PF-B3 (unit: mm)

(a) Front view

(b) Tendon profile

(c) Section A-A'   **(d) Section B-B'**   **(e) Section C-C'**

(f) Top view   **(g) Anchorage detail**
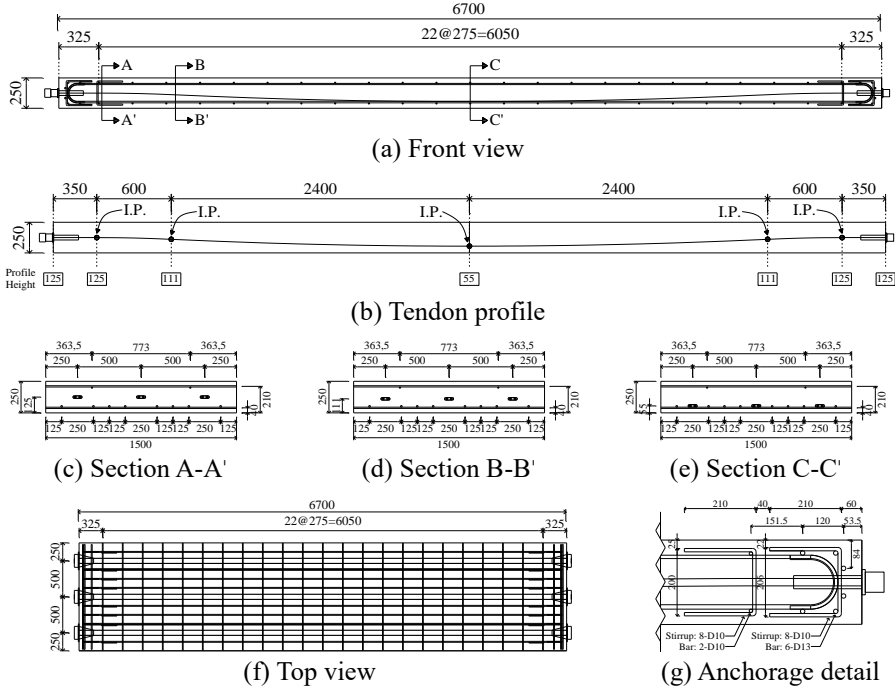
Figure A-3 Details of Specimen PF-U2 (unit: mm)

(a) Front view

(b) Tendon profile

(c) Section A-A'   **(d) Section B-B'**   **(e) Section C-C'**

(f) Top view   **(g) Anchorage detail**
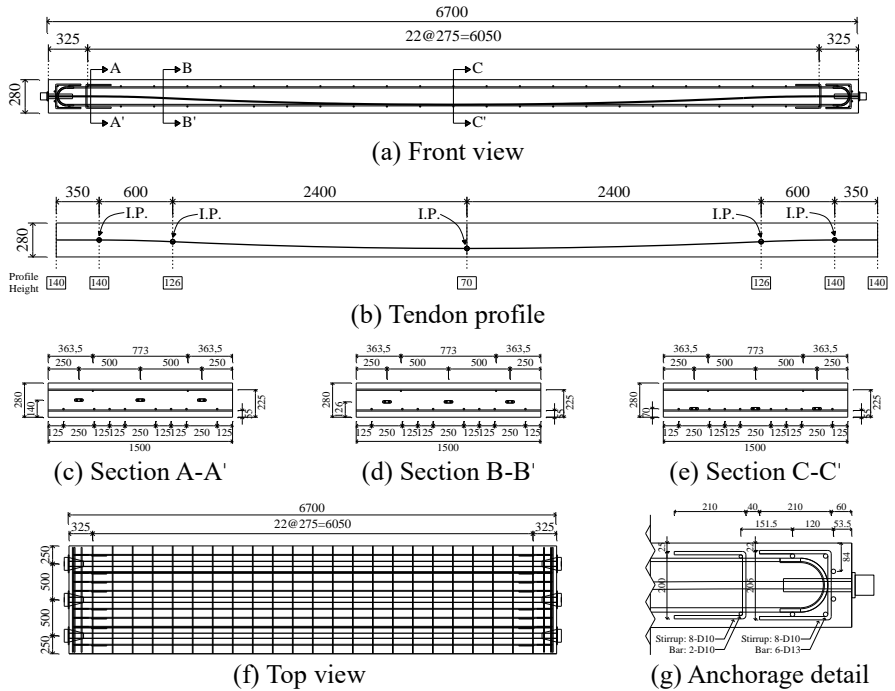
Figure A-4 Details of Specimen PF-U3 (unit: mm)

(a) Front view

(b) Tendon profile

(c) Section A-A' | **(d) Section B-B'** | **(e) Section C-C'**

(f) Top view | **(g) Anchorage detail**
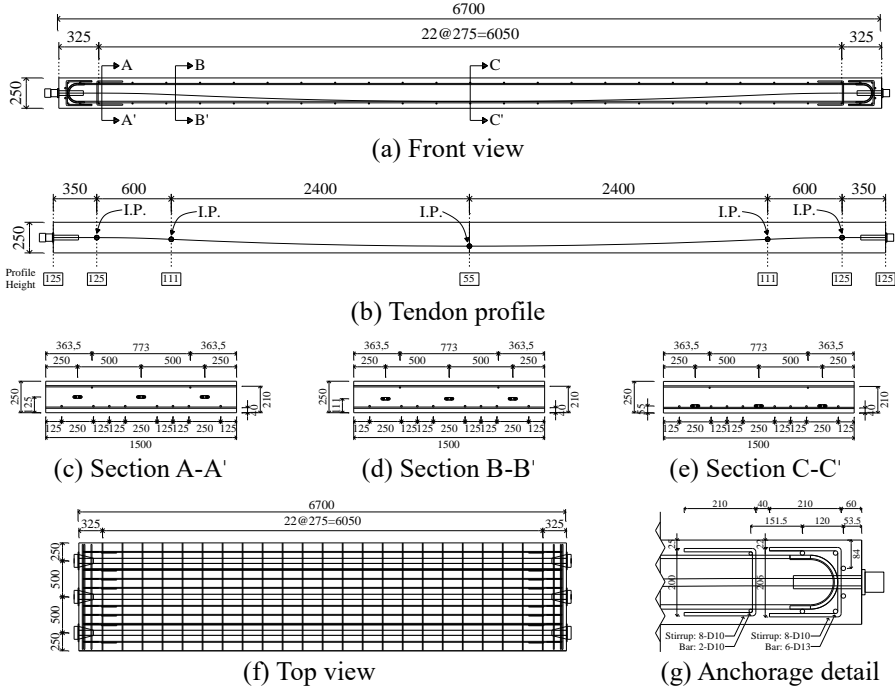
Figure A-5 Details of Specimen PF-G2 (unit: mm)

(a) Front view

(b) Tendon profile

(c) Section A-A' | **(d) Section B-B'** | **(e) Section C-C'**

(f) Top view | **(g) Anchorage detail**
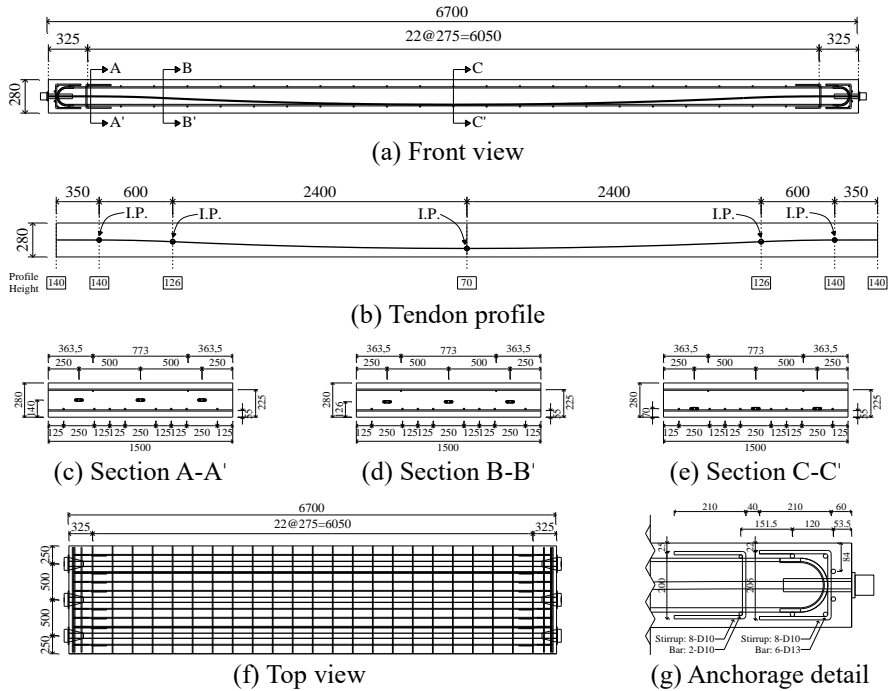
Figure A-6 Details of Specimen PF-G3 (unit: mm)

(a) Front view

(b) Tendon profile

(c) Section A-A' (d) Section B-B' (e) Section C-C'

(f) Top view (g) Anchorage detail
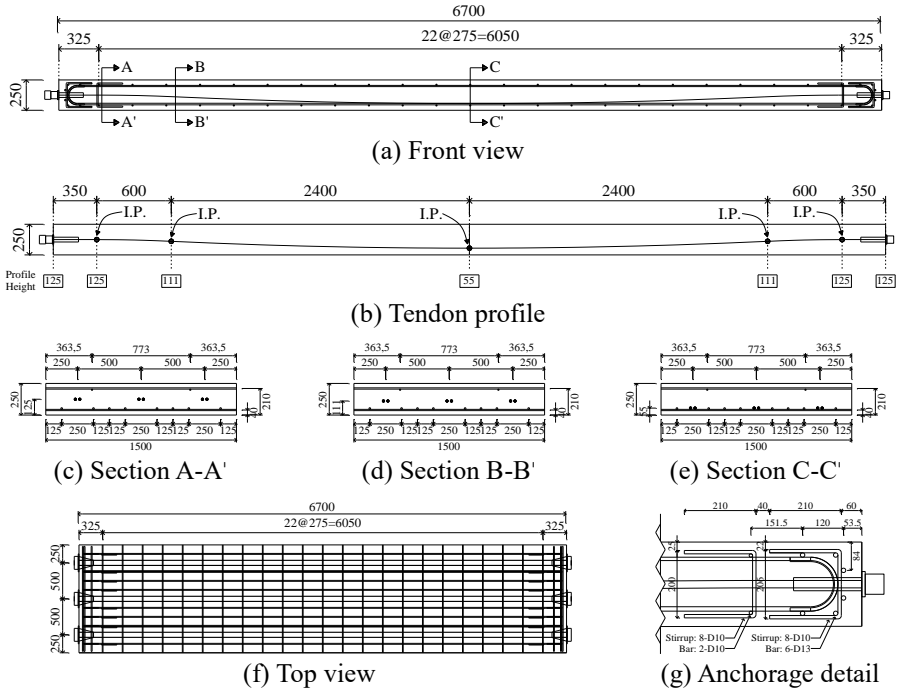
Figure A-7 Details of Specimen PF-S2 (unit: mm)

(a) Front view

(b) Tendon profile

(c) Section A-A' (d) Section B-B' (e) Section C-C'
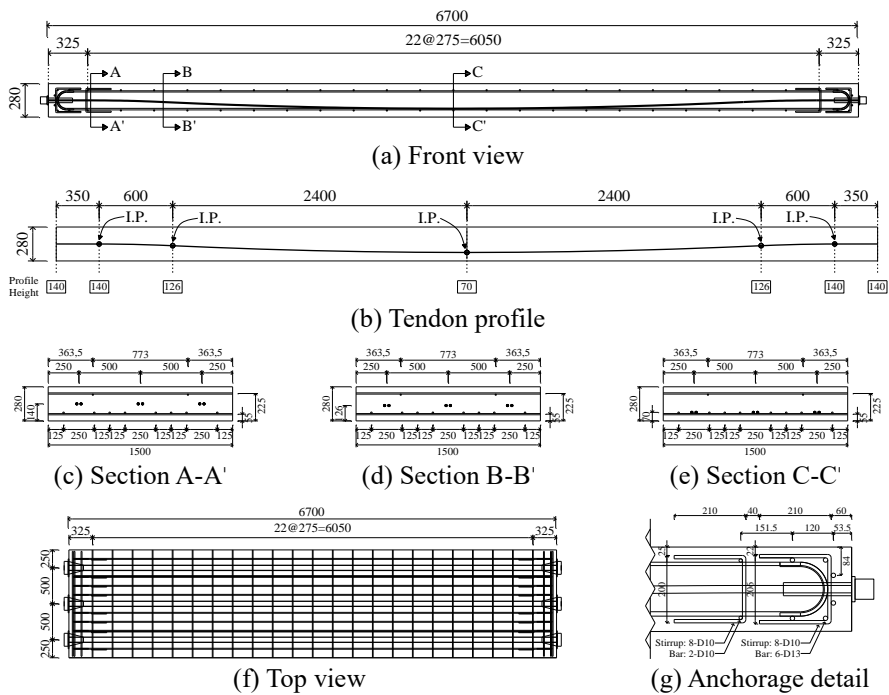
(f) Top view (g) Anchorage detail

Figure A-8 Details of Specimen PF-S3 (unit: mm)

Appendix B : Time-temperature curves at the bottom of slab
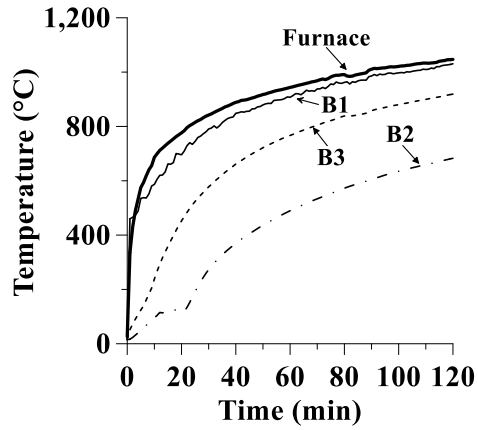
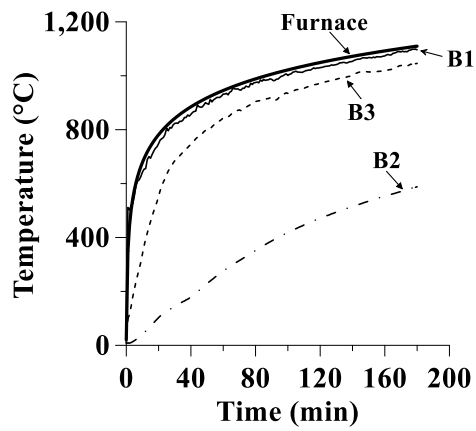**Figure B-1** Time-temperature curves at the bottom of slab (PF-B2)

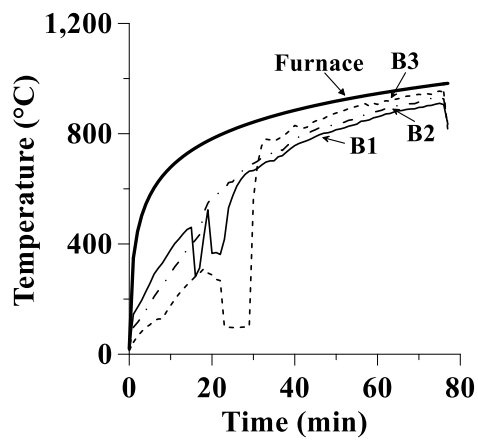**Figure B-2** Time-temperature curves at the bottom of slab (PF-B3)

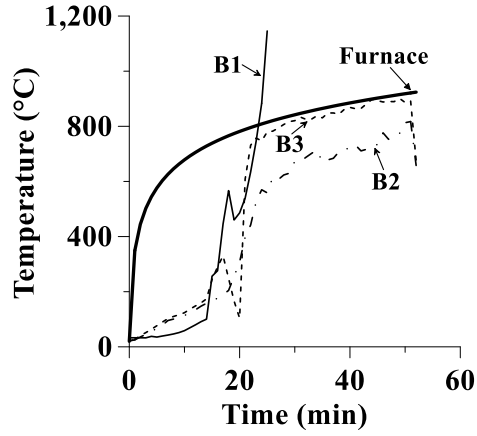**Figure B-3** Time-temperature curves at the bottom of slab (PF-U2)

106

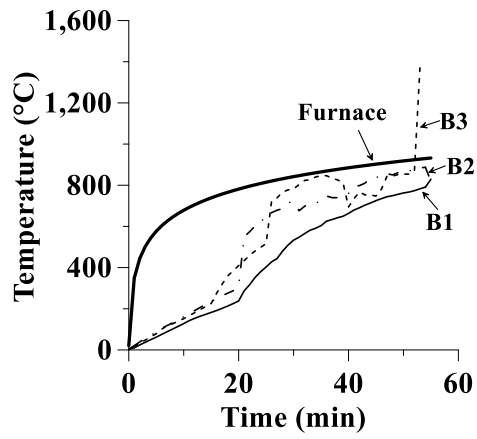**Figure B-4** Time-temperature curves at the bottom of slab (PF-U3)

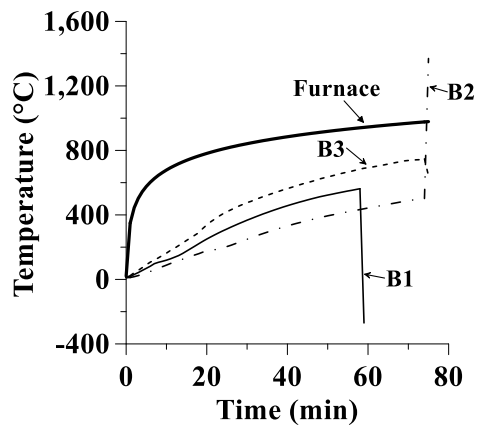**Figure B-5** Time-temperature curves at the bottom of slab (PF-G2)

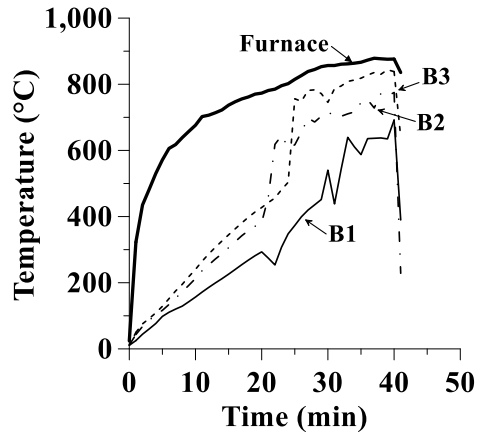**Figure B-6** Time-temperature curves at the bottom of slab (PF-G3)

Figure B-7 Time-temperature curves at the bottom of slab (PF-S2)
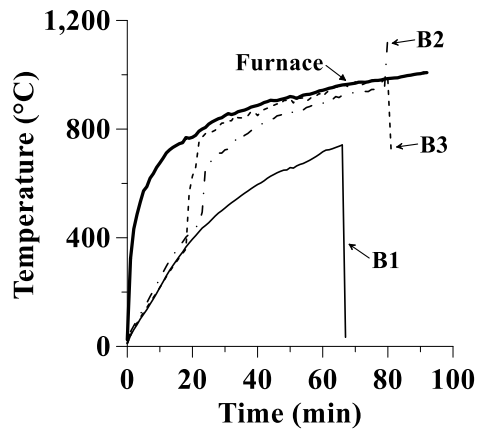

Figure B-8 Time-temperature curves at the bottom of slab (PF-S3)

국 문 초 록

텐던공법에 따른 일방향 포스트텐션 콘크리트 부재의 내화거동

최근 콘크리트 구조물에서 포스트텐션 공법의 적용은 지하 구조물, 장경간 구조물, 격납 구조물에서 증가하고 있다. 이에, 다양한 재난 상황에서의 구조 안전성을 확보하기 위해 여러 건축법규가 제정 및 개정되었다. 내화성 측면에서, 국내 내화시험 방법을 제안한 KS F 2257과 화재안전 설계기준을 제안한 국가표준이 있으며, 해외의 IBC 2018과 ASTM E119 등이 있다. 그러나, 제안된 표준들은 세부적인 내용이 부족하며 모호한 부분이 있다. 또한, 규정에서 제시하고 있는 기준의 적절성에 대한 추가 연구가 필요하다. 따라서, 본 연구에서는 구조물의 화재성능 평가를 위해 일방향 부착식 포스트텐션 콘크리트 슬래브 2개와 비부착식 포스트텐션 콘크리트 슬래브 6개의 화재거동에 대한 실험을 4점 정적하중 가력 및 가열을 통해 수행하였다.

본 실험에서 고려된 변수는 텐던공법 종류, 피복두께, 그리고 목표 내화성능이다. 4개의 실험체는 2시간의 화재를 견딜 수 있게 설계되었으며, 나머지는 3시간의 화재를 견딜 수 있게 설계되었다. 모든 실험체는 실험체의 바닥, 상부, 텐던 위치에 열전대를

설치하여 온도변화를 계측하였다. 또한, 자체제작한 로드셀을 설치하여 비부착 포스트텐션 콘크리트 슬래브의 긴장력 변화를 긴장 및 실험 시 계측하였다. 변위는 슬래브 중심에 LVDT를 설치하여 계측하였다.

실험 결과, 부착식 포스트텐션 콘크리트 슬래브의 경우, IBC 2018에서 규정하고 있는 최소 피복두께를 확보하였을 경우, 모두 2시간 및 3시간 이상 지속하중에 견딜 수 있음을 입증하였다. 하지만, 비부착식 포스트텐션 콘크리트 슬래브는 예상 시간보다 조기에 파열되었다. 콘크리트 파열력이 실험결과에 중요한 영향을 끼쳤으며, 조기 종료에 대한 여러 요인들이 조사되었다. 비록 실험이 조기에 종료되었지만, 텐던공법 종류에 따른 온도 변화, 긴장력 변화, 변위 변화 등의 화재 거동의 차이를 비교 분석할 수 있었다. 부착식 포스트텐션 콘크리트 슬래브의 경우, 유한요소해석을 통해 목표 내화성능 대비 최소 피복두께에 대한 화재성능을 평가하였다.

본 연구에서는 텐던공법에 따른 포스트텐션 콘크리트 일방향 부재의 화재거동을 분석하였다. 수치해석 기법을 사용하여 최소 피복두께에 따른 내화성능을 분석하였고, 화재 실험결과를 또한 검증하고자 하였다. 이 연구의 결과는 기준 조항의 세부 사항을 개정하기 위한 기초 연구자료로서 활용될 수 있을 것으로 기대된다.

핵심용어: 부착, 피복두께, 목표 내화성능, 일방향, 포스트텐션 콘크리트 슬래브, 텐던 공법 종류, 비부착.
학번: 2020-29310

감사의 글

2014년 서울대학교 건축학과에 학부과정으로 입학한 이후, 8년간의 학교생활은 저에게 큰 행운이자 경험이 되었습니다. 혼자서는 해내지 못할 많은 일들을 여러 좋은 사람들을 만나 이루었고 도움을 받았기에, 감사의 글을 통해 인사 올리고자 합니다.

먼저 서울대학교에서 건축구조라는 분야를 알게 해주시고, 대학생으로서 그리고 대학원생으로서 성장할 수 있도록 지도해주신 강현구 교수님께 진심으로 감사드립니다. 저에게 학문적 그리고 인격적으로 성장할 수 있게 아낌없이 지도해주신 교수님의 말씀들을 마음에 새겨 한층 더 성장하는 사람이 될 수 있도록 노력하겠습니다.

건축 구조의 근본적인 부분부터 짚어주시며 그 뼈대를 알게 해주신 홍성걸 교수님, 학부 지도교수님으로 열정으로 학문을 가르치시고 도와주시며 늘 한결음 다가와주신 이철호 교수님, 학문적 고찰과 아낌없는 격려와 조언으로 도움 주신 박홍근 교수님께 진심으로 감사를 드립니다. 존경하는 교수님들께 학위 심사를 받을 수 있어 영광으로 생각하며, 노력하는 제자가 되겠습니다.

본 논문의 핵심인 화재 실험 연구를 시작할 수 있게 도와주신 화성 건설기술연구원 화재안전연구소 여인환 소장님, 안재권 박사님, 류은미 박사님, 조규환 박사님, 전기수 수석 연구원님께 감사의 말을 드립니다.

고성능구조공학연구실 (HpSE) 인턴 연구원으로 시작하여 3년의 시간을 보내며 함께 생활하고 고생했던, 김상희 교수님, 정동혁 교수님, 조아서 교수님, 승용 형, 형엽 형, Fahimeh Yavartanoo, Hamidreza Alinejad Lashkariani, Andrew Nghiem, 성룡 형, 한석 형, 병욱 형, 동혁 형, 형석 형, 민규, 수현, Tse-An Chou, Gabriela Renee Martinez Lara, Pauline Lin Li Lam, Hafshah Salamah, 승헌 형, 상민, 한솔에게 감사합니다. 새로이 연구실에 들어오게 된 현식, 기완, 찬호에게도 응원의 말을 전합니다. 대학원 입학 동기로서 서로 돕고 의지했던 유상, 이현, 성부, 영식에게도 감사의 말을 전합니다.

앞으로 평생을 함께 할 동반자로서 끊임없이 격려해 주고 사랑해주고 기댐목이 되어준 채리에게 감사의 말을 전합니다. 인격적으로 나를 성장시켜주고 사랑받는다는 것이 무엇인지 알게 해주었으며, 기쁨과 슬픔을 모두 나눌 수 있는 언제나 변함없는 나의 친구이자 여자친구이자 곧 인생의 동반자가 될 채리에게 감사하며 같이 응원해주신 채리의 부모님과 언니에게도 감사합니다.

마지막으로 언제나 든든한 도움을 주시고 사랑을 주신 아버지, 어머니께 존경하고 사랑한다는 말을 전하고 싶습니다. 부모님이 계시기에 학업에 집중할 수 있었으며, 힘들 때마다 일어설 수 있었습니다. 단란하고 화목한 가정으로 유지될 수 있음에 감사하고 기도하며, 부모님의 기대에 보답할 수 있도록 늘 노력하는 아들이 되겠습니다.

모든 분들의 하시는 일이 잘 되시고 항상 건강하길 기도하며, 다시 한 번 진심으로 감사드립니다.

감사합니다.

<div align="right">2022년 2월</div>

<div align="right">박시영</div>